UNIVERSITY OF CALIFORNIA
RIVERSIDE

Accelerating the Quantum Optimal Control of Multi-Qubit Systems With Symmetry-Based Hamiltonian Transformations

A Dissertation submitted in partial satisfaction
of the requirements for the degree of

Doctor of Philosophy

in

Physics

by

Xian Wang

September 2023

Dissertation Committee:

Dr. Bryan M. Wong, Chairperson
Dr. Shan-Wen Tsai
Dr. Hai-Bo Yu

The Dissertation of Xian Wang is approved:

Committee Chairperson

University of California, Riverside

Acknowledgments

I am grateful to my academic advisor, Dr. Bryan M. Wong. You led me into academia. Your guidance, encouragement, and patience have been inspiring support for me to advance my research. I would not have been here without your help.

I am also grateful to my defense committee members, Dr. Shan-Wen Tsai and Dr. Hai-Bo Yu. Your insightful opinions and thoughtful feedback have been a significant help in my Ph.D. study.

Thank you to the collaborators in the Bryan M. Wong group, Dr. Anshuman Kumar, Mr. Akber Raza, Dr. Chengkuan Hong, Dr. Yuanqi Gao, Dr. Mahmut S. Okyay, and Dr. José M. Rodríguez-Borbón. I would not be able to complete my Ph.D. study without your help.

And my thanks to the collaborators at University of California, Riverside, Argonne National Laboratory, Lawrence Berkeley National Laboratory, and Johns Hopkins University, Dr. Christian R. Shelton, Dr. Nanpeng Yu, Dr. Paul Kairys, Dr. Sri Hari Krishna Narayanan, Dr. Jan Hückelheim, Dr. Paul Hovland, Dr. Adrián P. Diéguez, Dr. Khaled Z. Ibrahim, Dr. Dimitris Giovanis, and Dr. Michael Shields. Collaboration with you is an essential part of my Ph.D. study.

I appreciate the help and advice from the other members of the Bryan M. Wong group, Dr. Sharma S.R.K.C. Yamijala, Dr. Ravindra Shinde, Dr. Zulfikhar A. Ali, Dr. Hyuna Kwon, Mr. Simon Sandhofer, Mr. Cameron Chevalier, Dr. Steve D. Yang, Dr. Sohag Biswas, Dr. Kota Hanasaki, Dr. Min Choi, Mr. Yuan Chen, Dr. Qiang Xu, and Dr. Wafa Maftuhin.

My biggest thanks to my parents for their support, emotional and financial.

I acknowledge the funding support from the U.S. Department of Energy and the University of California, Riverside.

All chapters of this dissertation used materials from *Accelerating Quantum Optimal Control of Multi-Qubit Systems with Symmetry-Based Hamiltonian Transformations*, an article accepted for publication in *AVS Quantum Science*. Xian Wang is the major contributor to this article. Mahmut S. Okyay, Anshuman Kumar, and Bryan M. Wong also contributed to this article.

To my parents for all the support

ABSTRACT OF THE DISSERTATION

Accelerating the Quantum Optimal Control of Multi-Qubit Systems With Symmetry-Based Hamiltonian Transformations

by

Xian Wang

Doctor of Philosophy, Graduate Program in Physics
University of California, Riverside, September 2023
Dr. Bryan M. Wong, Chairperson

I developed a computationally efficient framework for accelerating the quantum optimal control of various multi-qubit systems. This framework decomposes the Hilbert space of the multi-qubit system and enables unitary transformations of the Hamiltonians based on the symmetry of finite groups. The Hamiltonians are block diagonalized after transformation, which features a natural structure for computing these blocks in parallel. Specifically, the size of the Hamiltonians of an n-qubit system is reduced from $2^n \times 2^n$ to $O(n \times n)$ or $O(\frac{2^n}{n} \times \frac{2^n}{n})$ under S_n symmetry or D_n symmetry, respectively. This approach reduces the execution time of quantum optimal control by orders of magnitude while the accuracy of the output is not affected. The Lie-Trotter-Suzuki decomposition generalizes this symmetry-based approach to a more general variety of multi-qubit systems. Based on the symmetry-induced decomposition of the Hilbert space, I propose the concept of symmetry-protected subspaces, which are potential platforms for preparing commonly used symmetric states, realizing simultaneous gate operations, quantum error suppression, and simulation of other quantum systems. A perspective on ladder operators and selection

rules is provided to facilitate the understanding of the transformation of the Hamiltonians. I provide the Python source code for the quantum optimal control framework and the symmetry-based methods.

Contents

List of Figures

List of Tables

Chapter 1

Introduction

As the development of classical computers deviates from Moore's law and approaches the limit to transistor size [1, 2, 3, 4], quantum computing becomes a promising candidate for enhancing future supercomputers. Several algorithms for quantum computing, including Shor's algorithm for factorizing integers [5] and Grover's algorithm for searching in unstructured databases [6], have been proposed and manifest the advantage of quantum computing over classical computing. Though several prototypes of quantum computers have been manufactured on multiple platforms, including superconducting transmons [7, 8, 9, 10, 11], superconducting fluxoniums [12, 13], trapped ions [14, 15], nitrogen-vacancy centers in diamonds [16, 17], and neutral atoms [18], quantum computing is still at its early stage and faces various challenges. One open problem that needs to be adequately addressed is the realization of fast and accurate quantum gates.

Quantum gates are the operations transforming quantum states. The most common method to realize quantum gates is manipulating quantum systems with external

controls, e.g., microwaves [19, 20, 21, 22, 23, 24, 25]. The dynamics of the interaction of quantum systems and microwaves follow the time-dependent Schrödinger equation. As such, we are naturally directed to the following question: How should we engineer time-dependent microwaves to realize desired quantum gates? Quantum optimal control (QOC) is developed to solve this problem. Despite the numerous computational techniques used to accelerate QOC calculations [26, 27], there have been much fewer works to simplify/accelerate QOC simulations of multi-qubit systems that take advantage of their intrinsic symmetry.

In this dissertation, I present a computationally efficient approach for the QOC of multi-qubit systems. Originating from the homogeneity and distinguishability of qubits, the Hamiltonians of a large family of multi-qubit systems feature the symmetry of finite groups. Based on this symmetry, I decompose the Hilbert space of the multi-qubit system and further introduce a unitary transformation of the Hamiltonians. Although there has been prior work on decomposing the Hilbert space of permutation-symmetric (S_n) multi-qubit systems [28, 29, 30, 31], these studies only considered analytical methods of small qubit systems. My work generalizes this decomposition approach to the dihedral group (D_n) symmetry (which brings more controllability to a multi-qubit system than S_n symmetry) and provides a mathematical justification for this approach. Multi-qubit systems with the symmetry of other finite groups can also be analyzed and simplified with my approach. The multi-qubit states lie in orthogonal subspaces after the decomposition, and the unitarily transformed Hamiltonians are block diagonalized. This benefits me by computing the evolution in each subspace in parallel, thus accelerating the QOC of multi-qubit systems. My tests on various problems indicate that this symmetry-based approach reduces the computational runtime

of QOC by orders of magnitude while maintaining the same accuracy of the outputs as the conventional method. This work enriches the toolbox for facilitating the realization of quantum gate operations with microwaves, which plays the role of firmware in quantum computers.

Inspired by the symmetry-induced decomposition of the Hilbert space, I propose the concept of symmetry-protected subspaces. The evolution of the quantum system is restricted inside each subspace as long as the Hamiltonian of the system preserves the symmetry of finite groups. Symmetry-protected subspaces provide a potential platform for quantum error suppression since the quantum state in any subspace cannot evolve to other subspaces. The energy levels of the eigenstates in each subspace can be manipulated by tuning the coupling coefficient between qubit pairs, enabling more controllability over the transitions of quantum states inside the subspaces. This allows me to simulate the Hamiltonians of other quantum systems with these subspaces. Symmetry-protected subspaces also provide platforms for preparing commonly-used symmetric states [32] and realizing simultaneous gate operations [5, 6]. Moreover, this work could potentially benefit quantum machine learning studies employing the symmetry of data and quantum circuits [33, 34].

In a realistic scenario, the symmetry of the entire multi-qubit system is typically broken. However, each term in the Hamiltonian preserves some reduced symmetry. The Lie-Trotter-Suzuki decomposition approximates the exponential propagator of the multi-qubit system with the product of multiple exponential terms, allowing me to transform each exponential with a different unitary adjoint matrix. [35, 36] The computation of each term then can be parallelized and accelerated with the symmetry-based transformation. As

such, the symmetry-based approach to accelerate QOC is generalized to a larger variety of multi-qubit systems.

In Sec. 1.1 and 1.2, I provide the background knowledge of quantum computing and quantum optimal control, respectively. I list my publications and my presentations at conferences during my Ph.D. study in Sec. 1.3. An outline of this dissertation is provided in Sec. 1.4.

Some content in this chapter is part of *Accelerating Quantum Optimal Control of Multi-Qubit Systems with Symmetry-Based Hamiltonian Transformations*, an article accepted for publication in *AVS Quantum Science*.

1.1 Quantum Computing

Quantum computing makes use of quantum bits for computational purposes. Quantum bits, or qubits, are the elementary units in quantum computers. Each qubit has two quantum states with distinct eigenenergies, and its evolution follows the fundamental principles of quantum mechanics. Developed in the 1920s, quantum mechanics is proven to be a complete theory for nearly all aspects of nature.

The proposal of employing quantum systems for computational purposes arose in the 1980s [37, 38] and was later enriched by advances in quantum algorithm design. Proposed in 1992, the Deutsch-Jozsa algorithm is the first algorithm that proves quantum computers are more efficient than classical computers in some computing tasks. [39, 40] Peter Shor's 1994 algorithm factorizes integers in polylogarithmic time, which is believed to be an NP problem on classical computers. [5] In 1996, Lov Grover proposed his algo-

rithm for searching in unstructured databases in $O(\sqrt{N})$ time, which runs in $O(N)$ time on classical computers. [6] Protocols for quantum cryptography are also potential revolutionary applications. [41, 42] These triumphs in quantum algorithms demonstrate quantum computers are more powerful than classical computers in some practical scenarios.

Another considerable breakthrough in quantum computing is the realization of various multi-qubit systems. Powered by the achievement in manipulating particles in quantum systems [19, 20, 21, 22, 23, 24, 25], several multi-qubit platforms, including superconducting transmons [7, 8, 9, 10, 11], superconducting fluxoniums [12, 13], trapped ions [14, 15], neutral atoms [18], nitrogen-cavity centers in diamonds [16, 17], etc., have been built up as prototypes of quantum computers. Though several computation tasks like boson sampling [43] and quantum random walk [44] have been tested on different platforms, general-purpose quantum computing remains a goal that can hardly be achieved in the short term. Increasing quantum volume, coherence time extension, quantum error mitigation, etc., are among the most significant open problems that need to be adequately addressed.

Quantum gate operations are quantum computers' most fundamental and underlying operations. Quantum gates are operations that transition quantum states in the Hilbert space. Thus far, the fidelity of quantum gates on all platforms is not perfect, which is a crucial problem for realizing real-world quantum computing. [45, 46, 47, 48] Inherent to the principles of quantum mechanics, quantum gates are unitary operations. This feature guarantees that the norm of quantum states is conserved and quantum evolutions are reversible. The most common approach to realizing quantum gates is manipulating the qubit system with external controls, e.g., microwaves. [19, 20, 21, 22, 23, 24, 25] Concerning a multi-qubit

system interacting with external controls, the time-varying Hamiltonian is a function of the controls. Following the Schrödinger equation, the evolution of the multi-qubit system can be calculated given the time-dependent controls.

When designing a quantum computer, instead of calculating the evolution of the computer system with the time-dependent controls, the inverse problem is more valuable, i.e., how should the external controls be engineered to steer a computer system towards some desired target state or to realize some desired quantum gates? Motivated by this problem, the study of QOC in multi-qubit systems is developed. [49, 50] The QOC for small-size problems like single-qubit and two-qubit quantum gates is well resolved. Concerning large-scale systems, it is proven that a small set of single-qubit and two-qubit quantum gates will be complete for realizing any quantum circuit. As such, QOC provides the firmware in a quantum computer since it instructs how to perform fundamental operations. Besides, QOC typically provides a more concise solution than reducing a complicated gate into universal gates when solving for large multi-qubit systems. I discuss the details of QOC in Sec. 1.2.

1.2 Quantum Optimal Control

Quantum optimal control, or QOC, is the study of designing the optimal controls that drive a quantum system to undergo some prescribed transitions. It is an essential tool for realizing gate operations in real-world quantum computing. [49, 50] Several general-purpose QOC frameworks, including GRAPE [51], Krotov [52], CRAB [53], etc., have been developed and applied to multi-qubit systems. In this dissertation, I implant the gradient ascent method from GRAPE. A loss function, typically the probability of the transition or

fidelity of the quantum gate, needs to be defined. The goal of QOC is to maximize the loss function by optimizing the controls. The gradient ascent method iteratively evaluates the gradient of the loss function with respect to the controls with backpropagation. Then the controls are updated based on the gradient in each iteration until the loss function is larger than some preset threshold.

In this dissertation, the QOC model is a semiquantum model, i.e., the Hamiltonians of the qubits are quantum and have eigenstates with distinct eigenenergies, and the time-dependent controls are classical and treated as continuous waves. The Hamiltonian of a multi-qubit system consists of two parts, the static Hamiltonian and the control Hamiltonian. The static Hamiltonian describes the dynamics feature of the multi-qubit system itself, and the control Hamiltonian describes the interaction of the qubits and the external control. In real-world quantum computers, qubits are typically realized by artificial particles, and their Hamiltonians can be complicated. However, we only employ two eigenstates with distinct energy levels. Thus, the Hamiltonians of single qubits can always be reduced to 2×2 Hermitian matrices. In a multi-qubit system, the state space is the tensor product of the state space of all single qubits. Therefore, the dimension of the Hilbert space increases exponentially as the number of qubits, i.e., the Hamiltonian size of a n-qubit system is $2^n \times 2^n$. The exponentially increasing Hamiltonian size is the most daunting challenge common to all QOC calculations in multi-qubit systems.

It is worth noting that the qubits in a quantum computer are typically homogeneous and distinguishable. That is, all the qubits are described by the same Hamiltonians, and each qubit can be distinguished from others and be assigned a unique index. Making

use of this feature, I customized a QOC framework for multi-qubit systems. The homogeneity and distinguishability can be accurately described by the symmetry of finite groups. I form the group algebra elements with the diagonal elements of the unitary irreducible representations (irreps) of the finite groups. After that, the group algebra elements are operated on the Fock states of spins to generate basis in orthogonal subspaces. The evolution of the multi-qubit system is confined to each subspace as long as the Hamiltonians of the multi-qubit system preserve the symmetry of finite groups. I further construct the unitary adjoint matrices transforming the Hamiltonians with the symmetry-induced basis. After transformation, the Hamiltonians are block diagonalized, enabling a natural approach for calculating each subspace in parallel. The accuracy of the QOC computation is not affected since the Hamiltonian transformation is unitary.

In general, the Hamiltonian of the entire multi-qubit system may not satisfy the symmetry of any finite group. However, looking into each term in the Hamiltonian, it typically has some reduced symmetry. This allows me to transform each term with a different adjoint matrix. When calculating the evolution of the multi-qubit system, I divide the time interval evenly into small steps. Then I approximate the propagator at each time step with the product of multiple exponential terms using the Lie-Trotter-Suzuki decomposition. [35, 36] These exponential terms can be block diagonalized by the adjoint matrices that transform the terms in the Hamiltonian as described above, enabling me to accelerate the QOC calculation with parallel computing. In this approach, the symmetry-based method for accelerating QOC calculation is generalized to nearly all multi-qubit systems with the Lie-Trotter-Suzuki decomposition.

1.3 Publications and Presentations at Conferences During the Ph.D. Study

I list my publications during my Ph.D. study as follows.

Xian Wang, Mahmut Sait Okyay, Anshuman Kumar, and Bryan M. Wong. Accelerating Quantum Optimal Control of Multi-Qubit Systems With Symmetry-Based Hamiltonian Transformations. Accepted for publication in *AVS Quantum Science*.

Xian Wang, Paul Kairys, Sri Hari Krishna Narayanan, Jan Hückelheim, and Paul Hovland. Memory-Efficient Differentiable Programming for Quantum Optimal Control of Discrete Lattices. In *2022 IEEE/ACM Third International Workshop on Quantum Computing Software (QCS)*, pages 94–99, Los Alamitos, CA, USA, Nov. 2022. IEEE Computer Society. [26]

Yuanqi Gao, Xian Wang, Nanpeng Yu, and Bryan M. Wong. Harnessing Deep Reinforcement Learning to Construct Time-Dependent Optimal Fields for Quantum Control Dynamics. *Physical Chemistry Chemical Physics*, 24(39):24012–24020, 2022. [54]

Akber Raza, Chengkuan Hong, Xian Wang, Anshuman Kumar, Christian R. Shelton, and Bryan M. Wong. NIC-CAGE: An Open-Source Software Package for Predicting Optimal Control Fields in Photo-Excited Chemical Systems. *Computer Physics Communications*, 258:107541, 2021. [55]

Xian Wang, Anshuman Kumar, Christian R. Shelton, and Bryan M. Wong. Harnessing Deep Neural Networks to Solve Inverse Problems in Quantum Dynamics: Machine-Learned Predictions of Time-Dependent Optimal Control Fields. *Physical Chemistry Chemical Physics*, 22(40):22889–22899, 2020. [56]

I list my presentations at conferences during my Ph.D. study as follows.

Harnessing Quantum Information Science for Enhancing Sensors in Harsh Fossil Energy Environment. FECM/NETL Spring R&D Project Review Meeting, Pittsburgh, PA, April 2023.

Accelerating the Quantum Optimal Control of Large Qubit Systems With Symmetry-Based Hamiltonian Transformations and Linear Unitary Propagators. APS March Meeting, Las Vegas, NV, March 2023.

Memory-Efficient Differentiable Programming for Quantum Optimal Control of Discrete Lattices. SC22, Quantum Computing Software Workshop, Dallas, TX, November 2022. [26]

1.4 Dissertation Outline

I provide the outline of this dissertation as follows.

In Ch. 2, I describe the dynamics of the multi-qubit system with the time-dependent Schrödinger equation. Several explicit examples of the Hamiltonians are given. I emphasize the symmetry of finite groups of these Hamiltonians. Besides, the framework of QOC, along with the pseudocode for the QOC algorithm, is provided.

The mathematical methods for the symmetry-based decomposition of the Hilbert space and the symmetry-induced unitary transformation of the Hamiltonians are provided in Ch. 3. I specifically discuss the details of the methods associated with the permutation group, S_n, and the dihedral group, D_n. The Clebsch-Gordan coefficients of the SU(2) group provide an equivalent approach to the Young method. Proof that validates the D_n-

based method is also provided. In addition, I provide details about how to combine the symmetry-based method and the Lie-Trotter-Suzuki decomposition.

The results of the symmetry-based method are provided in Ch. 4. I present the sparsity plots of the transformed Hamiltonians to show they are block diagonalized. A comparison of the results of the conventional and symmetry-based methods is provided to indicate the symmetry-based method generates the same outputs while the execution time is reduced by orders of magnitude. I also compare the outputs and execution time between the conventional method and the symmetry-based method combined with the Lie-Trotter-Suzuki decomposition for general multi-qubit systems.

In Ch. 5, I discuss the concept of symmetry-protected subspaces. Details are given about how to facilitate more controllability in the subspaces without breaking the symmetry of finite groups. I further discuss the proposals for quantum error suppression and simulating other quantum systems with symmetry-protected subspaces of multi-qubit systems. A perspective on ladder operators and selection rules is discussed to help understand the symmetry-based transformation of the Hamiltonians.

I conclude this dissertation in Ch. 6.

Chapter 2

Dynamics and Symmetry of Multi-Qubit Systems

In Sec. 2.1, I describe the dynamics of the multi-qubit system with the time-dependent Schrödinger equation. The exponential propagator is the analytical solution to the time-dependent Schrödinger equation. A summary of the QOC framework and the pseudocode are provided in Sec. 2.2. I especially highlight a modification to the golden-section search. I introduce the symmetry of the multi-qubit system with several example Hamiltonians in Sec. 2.3.

Some content in this chapter is part of *Accelerating Quantum Optimal Control of Multi-Qubit Systems with Symmetry-Based Hamiltonian Transformations*, an article accepted for publication in *AVS Quantum Science*, and *TRAVOLTA: GPU Acceleration and Algorithmic Improvements for Constructing Quantum Optimal Control Fields in Photo-Excited Systems*, an article submitted to *Computer Physics Communications*.

2.1 Dynamics of Multi-Qubit Systems

Like other quantum systems in the non-relativistic limit, multi-qubit systems follow the time-dependent Schrödinger equation

$$i\frac{\partial}{\partial t}|\psi(t)\rangle = H(t)|\psi(t)\rangle, \tag{2.1}$$

where $H(t)$ is the time-dependent Hamiltonian, and $|\psi(t)\rangle$ is the time-dependent quantum state. Here I take the reduced Planck constant, $\hbar$, as 1. Treating each qubit as a spin-$\frac{1}{2}$ particle, the quantum state $|\psi(t)\rangle$ of an n-qubit system lies in the Hilbert space, $\mathcal{H}(\mathbb{C}^{2^n})$, where 2^n is the dimension of the Hilbert space, and $\mathbb{C}$ means this is a complex space. Other than establishing a foundation for quantum advantage, this exponential increase in the dimension of the Hilbert space poses significant challenges for simulating multi-qubit systems with classical computers.

In my model, the Hamiltonian $H(t)$ has two parts, i.e.,

$$H(t) = H_0 + H_c(t), \tag{2.2}$$

where H_0 is the static Hamiltonian, and $H_c(t)$ is the time-dependent control Hamiltonian representing the interaction between the multi-qubit system and external electromagnetic pulse(s). Here I list several Hamiltonians as examples. The simplest static Hamiltonian for an n-qubit system in this dissertation is

$$H_0 = B_z \cdot \frac{1}{2}\sum_{i=1}^{n}\sigma_z^{(i)}, \tag{2.3}$$

which can be realized by applying a uniform static magnetic field, B_z, that interacts with all the qubits along the z-axis. I denote $\sigma_z^{(i)}$ to be shorthand for the tensor product $\mathbb{I}_2^{\otimes i-1} \otimes \sigma_z \otimes \mathbb{I}_2^{\otimes n-i}$, where σ_z and σ_x, σ_y in the following text are the Pauli matrices, and $\mathbb{I}_2$ is the rank-2 identity matrix. In many systems, such as the Ising model [57, 58, 59], each qubit is coupled to its neighbors. For a ring-shaped Ising model lattice, the static Hamiltonian becomes

$$H_0 = B_z \cdot \frac{1}{2} \sum_{i=1}^{n} \sigma_z^{(i)} + c_{\text{cpl}} \cdot \frac{1}{4} \sum_{i=1}^{n} \sigma_z^{(i)} \sigma_z^{(i+1)}, \tag{2.4}$$

where c_{cpl} is the coupling coefficient that represents the strength at which each qubit is coupled to its nearest neighbor. Similarly, $\sigma_z^{(i)}\sigma_z^{(i+1)}$ is shorthand for the tensor product $\mathbb{I}_2^{\otimes i-1} \otimes \sigma_z \otimes \sigma_z \otimes \mathbb{I}_2^{\otimes n-(i+1)}$, where the boundary condition $\sigma_z^{(n+i)} = \sigma_z^{(i)}, 1 \leq i \leq n$ holds. One example of the control Hamiltonian,

$$H_c = B_x(t) \cdot \frac{1}{2} \sum_{i=1}^{n} \sigma_x^{(i)} + B_y(t) \cdot \frac{1}{2} \sum_{i=1}^{n} \sigma_y^{(i)}, \tag{2.5}$$

represents the scenario of simultaneously manipulating all of the qubits with time-dependent microwaves along the x- and y-axes. Transitions between quantum states can be realized by optimizing $B_x(t)$ and $B_y(t)$, the controlling pulses. Some other Hamiltonians will be introduced later when necessary.

Given the Hamiltonians H_0 and $H_c(t)$ during the control duration $[0, T]$ and an initial state $|\psi(0)\rangle$, the final state $|\psi(T)\rangle$ can be formally calculated as follows:

$$|\psi(T)\rangle = \exp\left(-i \int_0^T (H_0 + H_c(t))\, \mathrm{d}t\right) |\psi(0)\rangle. \tag{2.6}$$

To obtain numerical solutions of Eq. 2.6, I employ the finite-difference time-domain (FDTD) method and discretize $[0, T]$ into N time steps, i.e., $\tau = \frac{T}{N}$ [51, 55]. With this approximation, the discrete propagation becomes

$$|\psi_{j+1}\rangle = \exp\left(-i\tau\left(H_0 + H_c[(j+\frac{1}{2})\tau]\right)\right)|\psi_j\rangle, \tag{2.7}$$

where $H_c[(j+\frac{1}{2})\tau]$ is the control Hamiltonian at time $t = (j+\frac{1}{2})\tau$, and $|\psi_j\rangle$ is the quantum state at time $t = j\tau$.

2.2 Quantum Optimal Control Algorithm

In contrast to conventional initial value problems in quantum dynamics, QOC focuses on the inverse problem to construct optimal control pulses for evolving a quantum system to undergo some desired transitions. In multi-qubit systems, this goal can be quantified as the probability that the final state $|\psi_N\rangle$ transitions to the target state $|\psi_t\rangle$ with the following inner product:

$$P(|\psi_N\rangle) = |\langle\psi_t|\psi_N\rangle|^2. \tag{2.8}$$

Here both $|\psi_N\rangle$ and $|\psi_t\rangle$ are normalized. Another common quantity is the fidelity that evaluates the similarity between the target gate operation K_t and the unitary propagator K_{N-1} of the real system:

$$F(K_{N-1}) = \left|\frac{\mathrm{Tr}(K_t^\dagger K_{N-1})}{D}\right|^2, \tag{2.9}$$

where Tr evaluates the trace of matrices, $K_{N-1} = \prod_{j=N-1}^{0} U_{j+\frac{1}{2}}$, $U_{j+\frac{1}{2}}$ is the exponential propagator in Eq. 2.7, and D is the dimension of the Hilbert space. Both $P(|\psi_N\rangle)$ and $F(K_{N-1})$ range between 0 and 1.

In this work, I implant the gradient ascent method from GRAPE into my QOC framework. [51] The loss function is typically defined as the probability in Eq. 2.8 or fidelity in Eq. 2.9. The QOC algorithm aims to maximize the loss function by optimizing the control pulses, e.g., $B_x(t)$ and $B_y(t)$ in Eq. 2.5. The control pulses are initialized as zeros at all time steps or white noise. Taking P as an example of the loss function, the control pulses are iteratively optimized with the gradient ascent method as follows:

$$B_{j+\frac{1}{2}}^{(l+1)} = B_{j+\frac{1}{2}}^{(l)} + \gamma \frac{\mathrm{d}P}{\mathrm{d}B_{j+\frac{1}{2}}^{(l)}}, \tag{2.10}$$

where $B_{j+\frac{1}{2}}^{(l)}$ represents either B_x or B_y at $t = (j+\frac{1}{2})\tau$ in the lth iteration, and γ is the update rate.

The gradient $\frac{\mathrm{d}P}{\mathrm{d}B_{j+\frac{1}{2}}}$ is evaluated using the chain rule [51, 55]. Without loss of generality, let me assume $B_{j+\frac{1}{2}}$ is B_x at $t = (j+\frac{1}{2})\tau$, and H_0 and $H_c(t)$ are as defined in Eqs. 2.4 and 2.5. Then the gradient can be written down explicitly as follows.

$$\begin{aligned}
\frac{\mathrm{d}P}{\mathrm{d}B_{j+\frac{1}{2}}} &= \frac{\partial P}{\partial(\langle\psi_t|\psi_N\rangle)} \cdot \frac{\mathrm{d}(\langle\psi_t|\psi_N\rangle)}{\mathrm{d}B_{j+\frac{1}{2}}} + \frac{\partial P}{\partial(\langle\psi_N|\psi_t\rangle)} \cdot \frac{\mathrm{d}(\langle\psi_N|\psi_t\rangle)}{\mathrm{d}B_{j+\frac{1}{2}}} \\
&= 2 \cdot \mathrm{Re}\left(\langle\psi_N|\psi_t\rangle \cdot \frac{\mathrm{d}(\langle\psi_t|\psi_N\rangle)}{\mathrm{d}B_{j+\frac{1}{2}}} \right) \\
&= 2 \cdot \mathrm{Re}\left(\langle\psi_N|\psi_t\rangle \cdot \langle\psi_t| \frac{\mathrm{d}(|\psi_N\rangle)}{\mathrm{d}B_{j+\frac{1}{2}}} \right),
\end{aligned} \tag{2.11}$$

where Re evaluates the real part of complex variables. Note that $|\psi_N\rangle = K_{N-1}|\psi_0\rangle = U_{N-\frac{1}{2}}U_{N-\frac{3}{2}}\dots U_{j+\frac{1}{2}}\dots U_{\frac{3}{2}}U_{\frac{1}{2}}|\psi_0\rangle$. Then

$$\begin{aligned}
\frac{\mathrm{d}(|\psi_N\rangle)}{\mathrm{d}B_{j+\frac{1}{2}}} &= U_{N-\frac{1}{2}}U_{N-\frac{3}{2}}\dots U_{j+\frac{3}{2}}\frac{\mathrm{d}U_{j+\frac{1}{2}}}{\mathrm{d}B_{j+\frac{1}{2}}}U_{j-\frac{1}{2}}\dots U_{\frac{3}{2}}U_{\frac{1}{2}}|\psi_0\rangle \\
&\approx -i\tau U_{N-\frac{1}{2}}U_{N-\frac{3}{2}}\dots U_{j+\frac{3}{2}}\sqrt{U_{j+\frac{1}{2}}}\tilde{H}_x\sqrt{U_{j+\frac{1}{2}}}U_{j-\frac{1}{2}}\dots U_{\frac{3}{2}}U_{\frac{1}{2}}|\psi_0\rangle \\
&= -i\tau U_{N-\frac{1}{2}}U_{N-\frac{3}{2}}\dots U_{j+\frac{3}{2}}\sqrt{U_{j+\frac{1}{2}}}\tilde{H}_x\sqrt{U_{j+\frac{1}{2}}}|\psi_j\rangle \\
&= -i\tau\left(\prod_{k=N-1}^{j+1}U_{k+\frac{1}{2}}\right)\sqrt{U_{j+\frac{1}{2}}}\tilde{H}_x\sqrt{U_{j+\frac{1}{2}}}|\psi_j\rangle,
\end{aligned} \tag{2.12}$$

where $\tilde{H}_x = \frac{1}{2}\sum_{i=1}^{n}\sigma_x^{(i)}$, and $\sqrt{U_{j+\frac{1}{2}}} = \exp\left(-i\frac{\tau}{2}\left(H_0 + H_c[(j+\frac{1}{2})\tau]\right)\right)$. The gradient with respect to $B_y(t)$ can be derived in a similar way. In case $H_c(t)$ is defined in a different way, I just need to make other approximations in Eq. 2.12.

It is worth noting that there is a recurrence relation in Eq. 2.12, i.e., $\prod_{k=N-1}^{j+1}U_{k+\frac{1}{2}} = \left(\prod_{k=N-1}^{j+2}U_{k+\frac{1}{2}}\right)U_{j+\frac{3}{2}}$. As such, I evaluate $\frac{\mathrm{d}P}{\mathrm{d}B_{j+\frac{1}{2}}}$ for $j = N-1$ first, then for $j = N-2$, $j = N-3$, and so on. Therefore, I claim that the gradient $\frac{\mathrm{d}P}{\mathrm{d}B_{j+\frac{1}{2}}}$ is evaluated with back-propagation. In contrast, the evaluation of $|\psi_N\rangle$ with Eq. 2.7 is called forward propagation since I evaluate $|\psi_1\rangle$ first, then $|\psi_2\rangle$, $|\psi_3\rangle$, and so on.

I employ the golden-section search to find the optimal update rate γ. The objective of the search method is to calculate the optimal γ that maximizes the loss function $P(\gamma)$ given the gradient $\frac{\mathrm{d}P}{\mathrm{d}B_{j+\frac{1}{2}}}$ in each iteration. The following analysis is based on the assumption that the maximum of $P(\gamma)$ is achieved at a γ larger than zero, and $P(\gamma)$ is concave near its maximum.

The search procedure is accomplished in two phases. First, the algorithm evaluates $P(\gamma^{(j)})$ at an increasing sequence of $\gamma^{(j)}, j = 0, 1, 2, \ldots$ which starts at $\gamma^{(0)} = 0$ and has the recurrence relation

$$\gamma^{(j+1)} = \left(\gamma^{(j)} + 0.3\right) \times 1.8, \tag{2.13}$$

where 0.3 and 1.8 are empirical coefficients and can be adjusted. The loop of the evaluation breaks when $P(\gamma^{(n)}) < P(\gamma^{(n-1)})$ is satisfied for some integer n so that the maximum of $P(\gamma)$ in the interval $[0, \gamma^{(n)}]$. To avoid an unrealistically large value of $\gamma^{(n)}$, it is common practice to set a threshold value, γ_{thres}, for the upper bound of the interval. If $P(\gamma^{(n)}) < P(\gamma^{(n-1)})$ is not achieved within $[0, \gamma_{\text{thres}}]$, the recurrence in Eq. 2.13 is forced to break. The second step is to search for the approximate value of optimal γ in the interval $[0, \gamma^{(n)}]$ with the golden-section algorithm. The function $P(\gamma)$ is evaluated at 0, $\frac{3-\sqrt{5}}{2}\gamma^{(n)}$, $\frac{\sqrt{5}-1}{2}\gamma^{(n)}$, and $\gamma^{(n)}$. Since $P(\gamma)$ is concave near the maximum, if $P(0)$ or $P(\frac{3-\sqrt{5}}{2}\gamma^{(n)})$ is the largest among the four values, the maximum is in the interval $[0, \frac{\sqrt{5}-1}{2}\gamma^{(n)}]$; otherwise, it is in the interval $[\frac{3-\sqrt{5}}{2}\gamma^{(n)}, \gamma^{(n)}]$. I retain the interval containing the maximum only and recursively evaluate $P(\gamma)$ at the golden ratio point of the new interval and shrink the interval again until the length of the interval is smaller than a threshold value. The midpoint of the final interval is then taken as the optimal γ, and the golden-section search procedure is terminated.

It is observed that the optimal update rate γ can be extremely large in the first iteration, which I further explain below. The transition probability, P (which ranges from 0 to 1 by definition), is typically a smooth functional of the control pulses $B_x(t)$ and $B_y(t)$. As such, the gradients $\frac{\partial P}{\partial B_x(t)}$ and $\frac{\partial P}{\partial B_y(t)}$ are zero when P is at its minimum of 0. These small gradient issues primarily occur in the first iteration since $B_{j+\frac{1}{2}}$ is initialized as a zero vector

or small amplitude white noise, making P nearly 0. As a result, γ needs to be very large to make any substantial update to $B_x(t)$ and $B_y(t)$. This forces the $\gamma^{(j)}$ defined in Eq. 2.13 to be a long sequence, and $P(\gamma^{(j)})$ has to be evaluated by the forward propagation many times, which is extremely time-consuming. To address this small gradient problem, I multiply the gradient $\frac{\mathrm{d}P}{\mathrm{d}B_{j+\frac{1}{2}}}$ by an empirical coefficient β to amplify its norm. The update rate γ' in this amplified gradient modification satisfies $\gamma'\beta \approx \gamma$, where γ is the update rate in the conventional method. Therefore, γ' can be small when the amplified gradient coefficient β is set to a sufficiently large value. In conclusion, the amplified gradient modification evaluates $P(\gamma)$ at much fewer points and outputs the correct optimal γ' in significantly less execution time.

As discussed above, extremely large values of γ occur when P is very small due to the small value of the gradient $\frac{\mathrm{d}P}{\mathrm{d}B_{j+\frac{1}{2}}}$ near the minimum P of zero. Besides, the optimal γ in the first iteration increases exponentially by the number of qubits. When $P > 0.001$, the optimal γ is typically less than 0.1, and the amplified gradient modification is no longer necessary. As such, I define the empirical coefficient β as follows for the QOC calculations when $n > 3$:

$$\begin{aligned} \beta &= \frac{0.1}{\sqrt{P}} \cdot 800^{n-3} \quad \text{if} \quad P < 0.001; \\ &= 1 \qquad\qquad\qquad\quad \text{if} \quad P \geq 0.001, \end{aligned} \tag{2.14}$$

where n is the number of qubits. In Eq. 2.14, the gradient $\frac{\mathrm{d}P}{\mathrm{d}B_{j+\frac{1}{2}}}$ is amplified only when $P < 0.001$ and $n > 3$, and β is negatively correlated to P. This definition functions well in my dissertation study.

The pseudocode of the QOC algorithm for constructing the optimized control pulses is given in Algorithm 1 below.

Algorithm 1 QOC Algorithm

Input: time interval $[0, T]$, time step τ, static Hamiltonian H_0, control Hamiltonian H_c, initial state $|\psi_0\rangle$, target state $|\psi_f\rangle$, initial guess for control pulses $B_x^{(0)}(t), B_y^{(0)}(t)$
Output: final state $|\psi_N\rangle$, optimized control pulses $B_x(t), B_y(t)$

$threshold \leftarrow 0.999$, $maxIter \leftarrow 100$
$l \leftarrow 0$
Initialize $B_{j+1/2}^{(l)}$ **for** $j \leftarrow 0, \ldots, N-1$
while $P < threshold$ **and** $l < maxIter$ **do**
    for $j \leftarrow 1, \ldots, N$ **do**
        Calculate $|\psi_j\rangle$ with Eq. 2.7
    end for
    Update P with Eq. 2.8
    for $j \leftarrow N-1, \ldots, 0$ **do**
        Calculate $\frac{\mathrm{d}P}{\mathrm{d}B_{j+\frac{1}{2}}^{(l)}}$ using the chain rule in Eqs. 2.11 and 2.12
    end for
    Calculate γ with the golden-section search method
    Update $B_{j+1/2}^{(l+1)}$ **for** $j \leftarrow 0, \ldots, N-1$ with Eq. 2.10
    $l \leftarrow l + 1$
end while
return $B_{j+1/2}$

2.3 Symmetry of Multi-Qubit Systems

In a real-world quantum computer, the physical qubits are typically realized by artificial or natural particles that have multiple eigenstates of distinct energy levels, e.g., superconducting transmons [7, 8, 9, 10, 11], superconducting fluxoniums [12, 13], and trapped ions [14, 15]. These particles are typically manufactured or manipulated to have the same engineering parameters. Therefore, the physical qubits in the same system are described by the same Hamiltonians. For computational purposes, each qubit, acting as a register,

must be distinguished from the others and assigned a unique address. Based on these facts, I claim the homogeneity and distinguishability of the qubits in the same system. The symmetry of finite groups of the multi-qubit system originates from the homogeneity and distinguishability of the qubits.

As shown in Eqs. 2.3, 2.4, 2.5, the Hamiltonian of an n-qubit system commonly consists of the following terms: $H_z = \sum_{i=1}^{n} \sigma_z^{(i)}$, $H_x = \sum_{i=1}^{n} \sigma_x^{(i)}$, and $H_y = \sum_{i=1}^{n} \sigma_y^{(i)}$ [57]. Writing down H_z explicitly as

$$H_z = \sum_{i=1}^{n} \sigma_z^{(i)} = \sigma_z \otimes \mathbb{I}_2^{\otimes n-1} + \mathbb{I}_2 \otimes \sigma_z \otimes \mathbb{I}_2^{\otimes n-2} + \cdots + \mathbb{I}_2^{\otimes n-1} \otimes \sigma_z, \tag{2.15}$$

it is obvious that any permutation of the qubit indices does not change H_z but only rearranges the terms in the summation. H_x and H_y have the same feature. Therefore, these Hamiltonian terms have the symmetry of the permutation group, S_n [60, 61, 62]. Note that the group actions are on the indices of the qubits, which does not require repositioning the qubits physically. When the interaction between neighboring qubits in a ring-shaped lattice is considered, one must include the coupling term $H_{z,\text{cpl}} = \sum_{i=1}^{n} \sigma_z^{(i)} \sigma_z^{(i+1)}$. This coupling term is invariant only under rotations and reflections of the indices of the qubits and, therefore, has the symmetry of the dihedral group, D_n [60, 61, 62]. Note that all terms having S_n symmetry also have D_n symmetry since D_n is a subgroup of S_n. Fig. 2.1b visually shows that the configuration of the non-interacting qubits is not affected by any S_n or D_n action on the indices. However, as shown in Fig. 2.1c, when the coupling is considered, the system is invariant only under D_n actions.

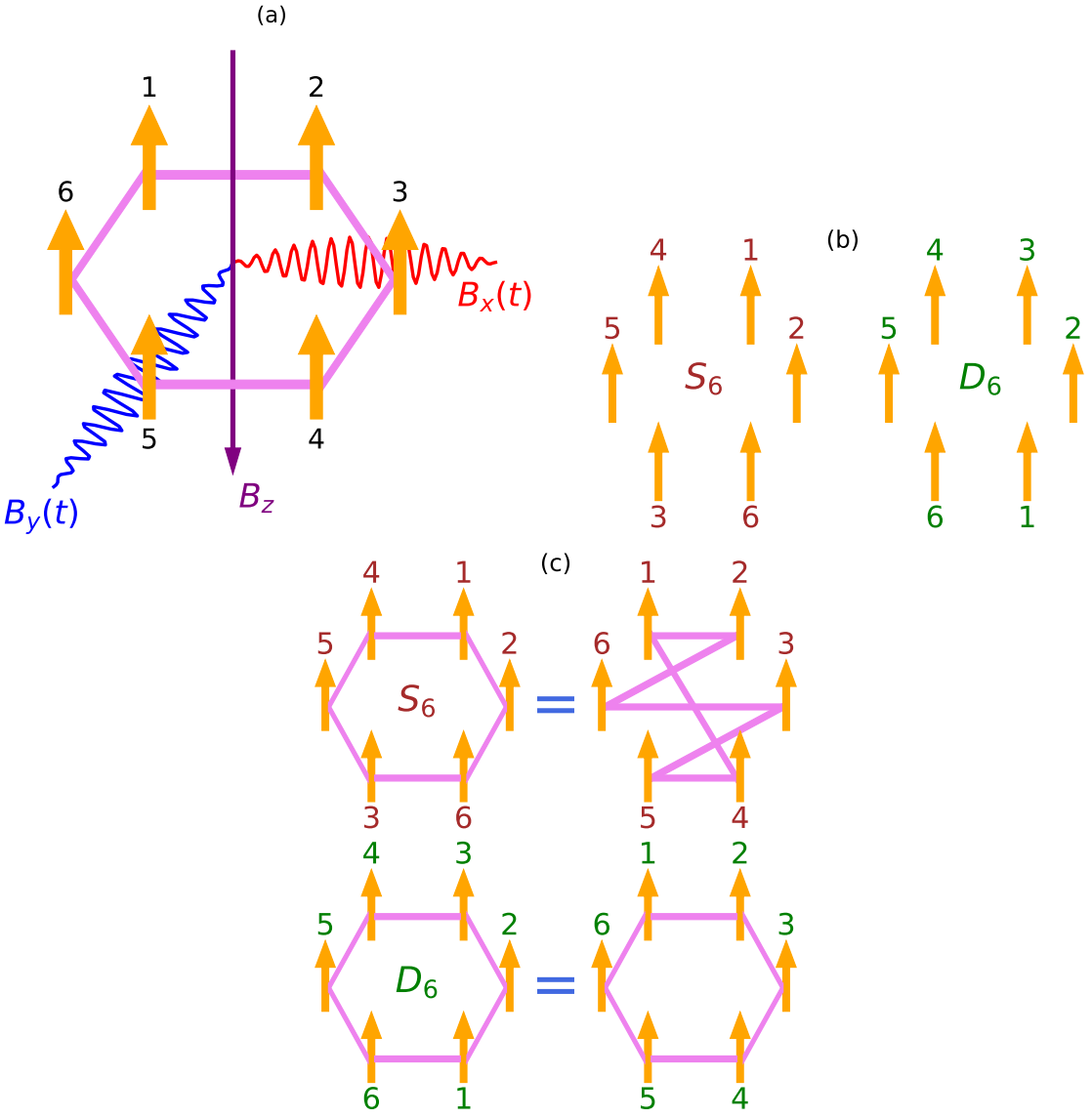

Figure 2.1: **Schematic of a multi-qubit system.** (a), A 6-qubit system in the presence of a static field B_z and time-dependent control pulses $B_x(t)$ and $B_y(t)$. Each qubit is represented by an orange arrow, and the numbers denote the indices of the qubits. The coupling between neighboring qubits is represented by violet bonds. (b), The 6-qubit system without coupling after applying an S_6 action (left) or a D_6 action (right) on the indices. (c), The 6-qubit system with coupling after applying an S_6 action (above) or a D_6 action (below) on the indices. The configurations connected with an equal sign are equivalent.

In many scenarios, the entire multi-qubit system may not satisfy the symmetry of any finite group. However, each term in the Hamiltonian may have a reduced symmetry of S_k, D_k ($k < n$), or some other finite group. Examples of broken symmetry in multi-qubit systems are presented in Sec. 3.5.

The symmetry of finite groups makes it possible to decompose the Hilbert space $\mathcal{H}(\mathbb{C}^{2^n})$ into orthogonal subspaces. Namely, $\mathcal{H}(\mathbb{C}^{2^n}) = \bigoplus_{\lambda,j} \mathcal{H}_j^\lambda$ under S_n symmetry or $\mathcal{H}(\mathbb{C}^{2^n}) = \bigoplus_{\theta,j} \mathcal{H}_j^\theta$ under D_n symmetry, where λ, j or θ, j indexes each specific subspace. Under these decompositions, I find an orthogonal and complete basis in each subspace. The orthogonality and completeness of the basis of the subspaces originate from the Schur orthogonality and completeness of the irreducible representations, or irreps, of finite groups. [60, 61, 62] Putting all the orthonormal bases together as columns, I construct the adjoint matrix A that transforms the Hamiltonians into block diagonal matrices. I denote the S_n- and D_n-induced adjoint matrices as A_{S_n} and A_{D_n}, respectively. In the following part of this dissertation, I also use the notation of A_S and A_D when they do not cause confusion. The procedure of decomposing the Hilbert space $\mathcal{H}(\mathbb{C}^{2^n})$ and generating the adjoint matrices A_S and A_D is given in detail in Ch. 3.

Chapter 3

Mathematical Methods

In Sec. 3.1 and 3.2, I present two equivalent methods, the Young method and the Clebsch-Gordan Coefficients of SU(2), for S_n-induced decomposition of the Hilbert space $\mathcal{H}(\mathbb{C}^{2^n})$. It is worth mentioning that the S_n symmetry was studied in several previous QOC works. [29, 30, 31] However, these studies focus on analytical methods of small qubit systems only, while I present a numerical approach for the S_n-induced method which applies to multi-qubit systems of any size. Based on the Young method, I developed the D_n-induced decomposition of $\mathcal{H}(\mathbb{C}^{2^n})$, which is shown in Sec. 3.3. A mathematical justification for the D_n-induced approach is provided in Sec. 3.4. It is worth noting that multi-qubit systems having the symmetry of other finite groups than S_n and D_n can also be analyzed and simplified in approaches similar to the D_n-induced method. In Sec. 3.5, I introduce how to combine the symmetry-based methods with the Lie-Trotter-Suzuki decomposition, which generalizes the symmetry-based methods to the scenario that the symmetry of the

entire multi-qubit system is broken. The source code in Python for the QOC of multi-qubit systems and the symmetry-based methods is provided in Sec. 3.6.

Some content in this chapter is part of *Accelerating Quantum Optimal Control of Multi-Qubit Systems with Symmetry-Based Hamiltonian Transformations*, an article accepted for publication in *AVS Quantum Science*.

3.1 Transformation of the Hamiltonians of S_n Symmetry With the Young Method

The static Hamiltonian without coupling in Eq. 2.3 obviously has S_n symmetry since it is proportional to $H_z = \sum_{i=1}^{n} \sigma_z^{(i)}$. Similarly, the control Hamiltonian in Eq. 2.5 also has S_n symmetry. If there are no other terms in the Hamiltonians, the whole multi-qubit system has S_n symmetry. Each qubit is described by the same static $(B_z \cdot \frac{1}{2}\sigma_z)$ and control $(B_x(t) \cdot \frac{1}{2}\sigma_x + B_y(t) \cdot \frac{1}{2}\sigma_y)$ Hamiltonian and assigned a unique index.

I temporarily specify the tensor products of the eigenstates of σ_z as the basis of the Hilbert space. Since both σ_z and $\mathbb{I}_2$ are diagonal matrices, H_z is diagonal; however, $H_x = \sum_{i=1}^{n} \sigma_x^{(i)}$ and $H_y = \sum_{i=1}^{n} \sigma_y^{(i)}$ are not. Considering the commutation relation $[\sigma_j, \sigma_k] = 2i\varepsilon_{jkl}\sigma_l$, where $j, k, l = x, y, z$, it is obvious that H_x, H_y, and H_z do not commute, and, thus, do not have eigenstates in common. Therefore, it is impossible to diagonalize H_x, H_y, and H_z simultaneously. Nevertheless, the S_n symmetry of the Hamiltonians leads to a second-best approach to construct another set of eigenstates of H_z. After being transformed with the unitary adjoint matrix made up of those eigenstates, H_x and H_y are block diagonalized while H_z is left diagonal.

The first approach to obtain these eigenstates is to use the irreps of S_n. I briefly introduce the Young method as follows. [60, 61, 62] Each irrep of S_n can be characterized by a standard Young diagram made up of n boxes. I denote the shape of the Young diagram as λ and the corresponding irrep as A^λ, where λ is an integer partition of n. For qubit systems, I only consider the irreps characterized by Young diagrams made up of no more than two rows, i.e., $\lambda = [n-m, m], n-m \geq m, m \geq 0$. I then generate standard Young tableaux by filling each Young diagram with the integers $1, 2, 3, \ldots, n$. The number of different standard Young tableaux d_λ that can be generated for each Young diagram λ is the dimension of the irrep A^λ. When $\lambda = [n-m, m]$, I have

$$d_\lambda = \frac{n!(n-2m+1)}{(n-m+1)!m!}. \tag{3.1}$$

I use the diagonal elements in each unitary irrep A^λ. For each group element $e_i \in S_n$, I denote its representation in A^λ as $A^\lambda(e_i)$. I further construct the following elements

$$O_j^\lambda = \sum_{i=1}^{n!} A_{jj}^\lambda(e_i) e_i, \ 1 \leq j \leq d_\lambda \tag{3.2}$$

in the group algebra $\mathcal{R}_{S_n}$ for each unitary irrep A^λ, where $A_{jj}^\lambda(e_i)$ is the jth diagonal element in the representation $A^\lambda(e_i)$. It should be noted that A^λ in Eq. 3.2 must be unitary. For each standard Young tableau T_j^λ with the shape λ, $1 \leq j \leq d_\lambda$, I define two permutation

subgroups $R(T_j^\lambda)$, $C(T_j^\lambda)$ of S_n as

$$\begin{aligned} R(T_j^\lambda) &= \{e \in S_n \mid e \text{ preserves the elements in each row of } T_j^\lambda\}, \\ C(T_j^\lambda) &= \{e \in S_n \mid e \text{ preserves the elements in each column of } T_j^\lambda\}. \end{aligned} \tag{3.3}$$

The Young symmetrizer of the tableau T_j^λ can subsequently be defined as

$$Y(T_j^\lambda) = \sum_{e \in R(T_j^\lambda),\ e' \in C(T_j^\lambda)} \operatorname{sgn}(e') e e', \tag{3.4}$$

where $\operatorname{sgn}(e') : S_n \to \{1, -1\}$ is the sign of the permutation e'. With the Young symmetrizers, an irrep A^λ can be derived, but it is not generally unitary and cannot be directly plugged into Eq. 3.2. The following recursive procedure yields the unitary irreps. Deleting the box filled with the largest remaining number repetitively for each Young tableau T_j^λ, I can define the standard Young tableau sequence $T_j^{\lambda,(0)} = T_j^\lambda, \ldots, T_j^{\lambda,(i)}, \ldots, T_j^{\lambda,(n-1)} = T^{[1]}$ where $\lambda, (i)$ is the shape of the Young diagram generated by deleting the boxes filled with the largest i numbers in T_j^λ. Each Young tableau $T_j^{\lambda,(i)}$ corresponds to the group S_{n-i} in the permutation group sequence $S_n \supset S_{n-1} \supset \cdots \supset S_1$. The recurrence relation is given as

follows:

$$
\begin{aligned}
O_j^{\lambda,(n-1)} &= O^{[1]} = e_0, \\
O_j^{\lambda,(n-2)} &= \frac{d_{\lambda,(n-2)}}{2!} O^{[1]} Y(T_j^{\lambda,(n-2)}) O^{[1]}, \\
&\vdots \\
O_j^{\lambda,(i)} &= \frac{d_{\lambda,(i)}}{(n-i)!} O_j^{\lambda,(i+1)} Y(T_j^{\lambda,(i)}) O_j^{\lambda,(i+1)}, \\
&\vdots \\
O_j^{\lambda,(1)} &= \frac{d_{\lambda,(1)}}{(n-1)!} O_j^{\lambda,(2)} Y(T_j^{\lambda,(1)}) O_j^{\lambda,(2)}, \\
O_j^{\lambda,(0)} &= O_j^{\lambda} = \frac{d_{\lambda}}{n!} O_j^{\lambda,(1)} Y(T_j^{\lambda}) O_j^{\lambda,(1)},
\end{aligned}
\tag{3.5}
$$

where e_0 is the identity element in the group, and $d_{\lambda,(i)}$ is the dimension of the irrep $A^{\lambda,(i)}$ of S_{n-i}.

Using $|\uparrow\rangle$ and $|\downarrow\rangle$ to represent the spin-up and spin-down states of a single qubit, respectively, the index-permutation group action on the Fock basis

$$
\alpha : S_n \times \{|\uparrow\rangle, |\downarrow\rangle\}^{\otimes n} \to \{|\uparrow\rangle, |\downarrow\rangle\}^{\otimes n} \tag{3.6}
$$

can be defined as follows. Any element $e \in S_n$ can be defined by its action on the index sequence $[1, 2, \ldots, i, \ldots, n]$, i.e., $e \cdot [1, 2, \ldots, i, \ldots, n] \mapsto [p_1, p_2, \ldots, p_i, \ldots, p_n], p_i \in \{1, 2, \ldots, n\}$. Denoting any Fock state in $\{|\uparrow\rangle, |\downarrow\rangle\}^{\otimes n}$ as $|s_1, s_2, \ldots, s_i, \ldots, s_n\rangle, s_i = \uparrow, \downarrow$, where i is the index for the ith qubit, the index-permutation action is $e \cdot |s_1, s_2, \ldots, s_i, \ldots, s_n\rangle \mapsto |s_{p_1}, s_{p_2}, \ldots, s_{p_i}, \ldots, s_{p_n}\rangle$, e.g., $(1,2,3,4,5) \cdot |\uparrow\downarrow\uparrow\uparrow\downarrow\rangle \mapsto |\uparrow_2 \downarrow_3 \uparrow_4 \uparrow_5 \downarrow_1\rangle = |\downarrow\uparrow\downarrow\uparrow\uparrow\rangle$. In terms of the group algebra elements $O_j^{\lambda} = \sum_{i=1}^{n!} A_{jj}^{\lambda}(e_i) e_i, \lambda = [n-m, m], 1 \le j \le d_{\lambda}$,

which is a linear combination of group elements, I define

$$O_j^\lambda \cdot |s_1, s_2, \ldots, s_i, \ldots, s_n\rangle = \sum_{i=1}^{n!} \left(A_{jj}^\lambda(e_i)(e_i \cdot |s_1, s_2, \ldots, s_i, \ldots, s_n\rangle) \right). \tag{3.7}$$

As such, O_j^λ become operators acting on the Fock states, and it is trivial to show that for any number m, $0 \leq m \leq n$, the following set

$$\{|s_1, s_2, \ldots, s_i, \ldots, s_n\rangle \mid s_i = \uparrow, \downarrow; m \text{ of } \uparrow, (n-m) \text{ of } \downarrow\} \tag{3.8}$$

is an orbit in $\{|\uparrow\rangle, |\downarrow\rangle\}^{\otimes n}$ since any index-permutation action $e \in S_n$ does not convert a spin-up to a spin-down or inversely but only rearranges the spins.

Each operator O_j^λ acts on no more than one element in each orbit. The elements to be acted on can be found with the Weyl tableaux that can be generated by filling the boxes in the Young diagram $\lambda = [n-m, m]$ with $\uparrow$ and $\downarrow$ entries. I fill all the boxes in the second row with $\downarrow$ and all the boxes right above the second row with $\uparrow$ entries. The rest of the boxes (i.e., the boxes in the first row with no box below them) can be filled with either $\uparrow$ or $\downarrow$ so that no $\uparrow$ is to the right of any $\downarrow$. In this way, there are $n - 2m + 1$ different Weyl tableaux for each operator O_j^λ. It should be noted that the Young tableau T_j^λ corresponding to O_j^λ has the same shape with the Weyl tableaux, (i.e., $\lambda = [n-m, m]$). With the number i in each box of the Young tableau T_j^λ being the index for the spin in the same box of each Weyl tableau, $n - 2m + 1$ elements in $\{|\uparrow\rangle, |\downarrow\rangle\}^{\otimes n}$ will be generated. Obviously, each of them is an eigenstate of H_z and belongs to a different orbit. Therefore, those $n - 2m + 1$ elements are orthogonal to each other. Acting O_j^λ on the $n - 2m + 1$

elements, I obtain the orthogonal basis for a subspace of the Hilbert space $\mathcal{H}(\mathbb{C}^{2^n})$. Each basis vector is still an eigenstate of H_z. It can be shown that the subspaces generated by different O_j^λ are orthogonal to each other, and I denote each subspace as $\mathcal{H}_j^\lambda$. The procedure above decomposes the Hilbert space $\mathcal{H}(\mathbb{C}^{2^n})$ with a dimension of 2^n into

$$\sum_{\lambda=[n-m,m]}^{n-m\geq m,m\geq 0} d_\lambda = \sum_{m=0}^{\lfloor n/2 \rfloor} \frac{n!(n-2m+1)}{(n-m+1)!m!} \tag{3.9}$$

orthogonal subspaces. Each subspace has a dimension of $n-2m+1$.

Thus far, with the Young method, I generated the orthogonal basis of the subspaces $\{\mathcal{H}_j^\lambda\}$. I next normalize the basis and let them be the columns of a unitary matrix A_S such that the basis of each particular subspace is positioned together. Since all the columns of A_S are eigenstates of H_z, after the unitary similarity transformation with the adjoint matrix A_S, $H_z' = A_S^\dagger H_z A_S$ remains diagonal. Moreover, after the same unitary similarity transformation, $H_x' = A_S^\dagger H_x A_S$ and $H_y' = A_S^\dagger H_y A_S$ are block diagonal. The nonzero elements in each block of H_x' and H_y' are distributed at the minor diagonals closest to the main diagonal (see Figs. 4.1, 4.2, 4.3, 4.4, and 4.5 in Sec. 4.1). The number of blocks equals the number of subspaces $\mathcal{H}_j^\lambda$ as described in Eq. 3.9, while the dimension of each block is consistent with the dimension of each subspace (i.e., $(n-2m+1)\times(n-2m+1)$).

Since the Hamiltonians in Eqs. 2.3 and 2.5 are block diagonal after the unitary similarity transformation with A_S, the evolution of a pure state $|\psi\rangle$ in any subspace $\mathcal{H}_j^\lambda$ is strictly confined within that subspace. In other words, if the initial state $|\psi(0)\rangle$ is in some subspace $\mathcal{H}_j^\lambda$, regardless of the temporal forms of the control pulses $B_x(t)$ and $B_y(t)$, the final state $|\psi(T)\rangle$ must also be in the same subspace. If the initial state is defined as a

linear combination of states in multiple subspaces, i.e.,

$$|\psi(0)\rangle = \sum_{\lambda,j} c_j^\lambda |\psi_j^\lambda(0)\rangle, c_j^\lambda \in \mathbb{C}, |\psi_j^\lambda(0)\rangle \in \mathcal{H}_j^\lambda, \tag{3.10}$$

the final state must also be in those subspaces with the same probabilities, i.e.,

$$|\psi(T)\rangle = \sum_{\lambda,j} {c'}_j^\lambda |\psi_j^\lambda(T)\rangle, {c'}_j^\lambda \in \mathbb{C}, |\psi_j^\lambda(T)\rangle \in \mathcal{H}_j^\lambda, \|{c'}_j^\lambda\| = \|c_j^\lambda\|, \tag{3.11}$$

as long as the Hamiltonians preserve the S_n symmetry. This implies that λ is a good quantum number in a multi-qubit system with S_n symmetry. Later I will show that λ is equivalent to the quantum number J, the total spin angular momentum of the multi-qubit system.

One disadvantage of the Young method is its computational complexity. Generating different O_j^λ can take different runtimes, while the most time-consuming one, $O_1^{[n]}$, takes

$$O\left(\prod_{i=1}^{n} (i!)^{2^{n-i}}\right) \tag{3.12}$$

group operations to be generated. The table below summarizes the timing of the Young method for $3 \leq n \leq 7$. Obviously, it is not practical to generate the complete adjoint matrix A_S with the Young method when n is large. It should be noted that the orthogonal decomposition of the Hilbert space with the Young method,

$$\mathcal{H}(\mathbb{C}^{2^n}) = \bigoplus_{\lambda,j} \mathcal{H}_j^\lambda, \tag{3.13}$$

is used to generate the representation space of unitary groups, namely SU(2), in this study. [60, 61, 62] Therefore, the Clebsch-Gordan coefficients of SU(2), another method for generating the unitary irreps of SU(2), should lead to the same direct sum decomposition in Eq. 3.13, as I show in the next section.

Table 3.1: Comparison of computational runtimes for generating the adjoint matrix A with different methods

	Computational Walltime (seconds)		
Number of qubits n	Young method	CG coefficients of SU(2)	D_n group algebra elements as operators
3	0.0077	0.0024	0.0012
4	0.0178	0.0100	0.0023
5	0.4748	0.0428	0.0046
6	63.8318	0.1848	0.0356
7	21286.3550	0.8066	0.0245
8	-	3.4327	0.0581
9	-	14.5743	0.1380
10	-	61.0588	0.3467
11	-	258.1316	0.7800
12	-	1080.7927	1.8423
13	-	4436.7408	4.4299
14	-	18832.3390	11.1521

Data collected with 8 Intel Broadwell CPUs. Computational timings for the Young method were not tested for 8 qubits and higher.

3.2 Transformation of the Hamiltonians of S_n Symmetry With the Clebsch-Gordan Coefficients of SU(2)

The Clebsch-Gordan (CG) coefficients are the coefficients for the direct sum decomposition of the direct product of two group irreps. When there is no coupling be-

tween neighboring qubits, the n-qubit system can be described with $\mathrm{SU}(2)^{\otimes n}$, so I can focus on the CG coefficients of SU(2) in this section. The CG coefficients of SU(2), denoted as $\langle J_1, M_1; J_2, M_2 \mid J, M\rangle$, has an analytical expression. The angular momentum $J \in \{0, \frac{1}{2}, 1, \frac{3}{2}, 2, \dots\}$ and the angular momentum projection onto the z-axis $M \in \{-J, -J+1, \dots, J-1, J\}$ are good quantum numbers characterizing the orthonormal basis $|J, M\rangle$, i.e., $\langle J', M' \mid J, M\rangle = \delta_{J'J}\delta_{M'M}$. $\langle J_1, M_1; J_2, M_2 \mid J, M\rangle$ is nonzero if and only if $|J_1 - J_2| \leq J \leq J_1 + J_2$ and $M = M_1 + M_2$. When one of the two irreps is the 2-dimensional irrep (i.e., $J_2 = \frac{1}{2}$), the CG coefficients $\langle J_1, M_1; \frac{1}{2}, M_2 \mid J, M\rangle$ reduce to

$$\begin{aligned}
\left\langle J_1, M_1; \frac{1}{2}, \frac{1}{2} \,\middle|\, \left(J_1 + \frac{1}{2}\right), M \right\rangle &= \sqrt{\frac{J_1 + M + \frac{1}{2}}{2J_1 + 1}}, \\
\left\langle J_1, M_1; \frac{1}{2}, -\frac{1}{2} \,\middle|\, \left(J_1 + \frac{1}{2}\right), M \right\rangle &= \sqrt{\frac{J_1 - M + \frac{1}{2}}{2J_1 + 1}}, \\
\left\langle J_1, M_1; \frac{1}{2}, \frac{1}{2} \,\middle|\, \left(J_1 - \frac{1}{2}\right), M \right\rangle &= -\sqrt{\frac{J_1 - M + \frac{1}{2}}{2J_1 + 1}}, \\
\left\langle J_1, M_1; \frac{1}{2}, -\frac{1}{2} \,\middle|\, \left(J_1 - \frac{1}{2}\right), M \right\rangle &= \sqrt{\frac{J_1 + M + \frac{1}{2}}{2J_1 + 1}}.
\end{aligned} \tag{3.14}$$

The eigenstates of a single qubit can be written as $|\frac{1}{2}, \frac{1}{2}\rangle = |\uparrow\rangle$ and $|\frac{1}{2}, -\frac{1}{2}\rangle = |\downarrow\rangle$. When an additional qubit is added into the system, applying the CG coefficients in Eq. 3.14 gives the eigenstates of the two-qubit system, i.e., the symmetric triplet states $|1, 1\rangle = |\uparrow\uparrow\rangle$, $|1, 0\rangle = \frac{1}{\sqrt{2}}(|\uparrow\downarrow\rangle + |\downarrow\uparrow\rangle)$, $|1, -1\rangle = |\downarrow\downarrow\rangle$, and the anti-symmetric singlet state $|0, 0\rangle = \frac{1}{\sqrt{2}}(|\uparrow\downarrow\rangle - |\downarrow\uparrow\rangle)$. In other words, the procedure of the orthogonal decomposition of the Hilbert space $\mathcal{H}(\mathbb{C}^{2^n})$ of the combined two spin-$\frac{1}{2}$ systems is to decompose the direct product of two 2-dimensional irreps of SU(2) into the direct sum of two irreps. Similarly, when a new qubit is added to the multi-qubit system, the CG coefficients in Eq. 3.14 allow

me to decompose the direct product of the irrep carried by each existing subspace and a 2-dimensional irrep into the direct sum of two if $J_1 > 0$, or one if $J_1 = 0$, irrep(s). In this way, the orthonormal basis of new orthogonal subspaces (i.e., the eigenstates of the multi-qubit system) can be generated.

Following the procedure above and iteratively applying Eq. 3.14, the eigenstates, $|J, M\rangle$, of a multi-qubit system with any number of qubits n can be generated. These eigenstates are in different subspaces characterized by the angular momentum J, and I denote these subspaces as $\mathcal{H}^J$. Each $\mathcal{H}^J$ has a total of $2J + 1$ basis kets $|J, M\rangle$. It is worth noting that different subspaces can have the same value of J. To distinguish among the subspaces $\{\mathcal{H}^J\}$ characterized by the same J, I require the evolution history of J. According to the CG coefficient $\langle J_1, M_1; \frac{1}{2}, M_2 \mid J, M\rangle$, the angular momentum J of each subspace $\mathcal{H}^J$ of a n-qubit system and its counterpart J_1 of the $(n-1)$-qubit system satisfies the relation $J = J_1 + \frac{1}{2}$ or $J = J_1 - \frac{1}{2}$. I denote J as $J^{(0)}$, J_1 as $J^{(1)}$, and the angular momentum in the $(n-2)$-qubit system as $J^{(2)}$. This sequence of angular momenta $J^{(0)} = J, J^{(1)}, J^{(2)}, \ldots, J^{(n-1)} = \frac{1}{2}$ indicates how the subspace $\mathcal{H}^J$ is evolved to and is unique for each subspace. I can then use the evolution history of J, denoted as the sequence $J^{(n-1)}, \ldots, J^{(i)}, \ldots, J^{(0)}$, or $[J^{(i)}]$ for short, to distinguish each of the $\mathcal{H}^J$ with the same J. I denote each $\mathcal{H}^J$ with the evolution history $[J^{(i)}]$ as $\mathcal{H}^J_{[J^{(i)}]}$. Similar to the Young method in the previous subsection, I let the basis $|J, M\rangle$ in each $\mathcal{H}^J_{[J^{(i)}]}$ be the columns of the adjoint matrix A_S. After a unitary similarity transformation with A_S, $H'_z = A_S^\dagger H_z A_S$ remains diagonal, and $H'_x = A_S^\dagger H_x A_S$ and $H'_y = A_S^\dagger H_y A_S$ are block diagonal. Only the elements in the minor diagonals closest to the main diagonal in each block of H'_x and H'_y are nonzero.

Therefore, H_x and H_y are the control Hamiltonians that change M by ± 1 but keep J and $[J^{(i)}]$ unchanged. Further details are provided in Sec. 5.2.

Thus far, I have introduced two methods for transforming the Hamiltonians: utilizing the group algebra elements of S_n with the Young method and decomposing the direct product of the irreps of SU(2) into a direct sum iteratively. Both methods decompose the Hilbert space $\mathcal{H}(\mathbb{C}^{2^n})$ into orthogonal subspaces $\{\mathcal{H}_j^\lambda\}$ or $\{\mathcal{H}_{[J^{(i)}]}^J\}$ and generate the orthonormal basis in each subspace. Since the two sets of subspaces both carry the irreps of SU(2), the basis of either set of subspaces can be linearly transformed to the other. In fact, denoting the adjoint matrix generated with the Young method as A_S^{Y} and that generated with the CG coefficients of SU(2) as A_S^{CG}, tests for up to 7 qubits show that $A_S^{\mathrm{Y}\dagger} A_S^{\mathrm{CG}}$ is a permutation matrix (i.e., there is only one element of 1 in each row and in each column of $A_S^{\mathrm{Y}\dagger} A_S^{\mathrm{CG}}$, while the other elements are all 0, as shown in Fig. 3.1). Therefore, the adjoint matrices generated with the two methods are mathematically equivalent and only differ in the sorting of the subspaces.

Since the orthonormal basis of the two sets of subspaces, $\{\mathcal{H}_j^\lambda\}$ and $\{\mathcal{H}_{[J^{(i)}]}^J\}$, are the same, the quantum numbers $\lambda = [n-m, m]$ and J characterizing these subspaces must coincide with each other. It should be noted that the dimension of the subspace $\mathcal{H}_j^\lambda$ is $n - 2m + 1$ and that of $\mathcal{H}_{[J^{(i)}]}^J$ is $2J + 1$. The constraint $n - 2m + 1 = 2J + 1$ must be satisfied so that the subspaces $\mathcal{H}_j^\lambda$ and $\mathcal{H}_{[J^{(i)}]}^J$ can be the same. The index sets, $\{j\}$ and $\{[J^{(i)}]\}$, should also have the same number of elements so that there is a one-to-one mapping between them. Table 3.2 shows an example of the correspondence between $\{\mathcal{H}_j^\lambda\}$ and $\{\mathcal{H}_{[J^{(i)}]}^J\}$ of the 6-qubit system.

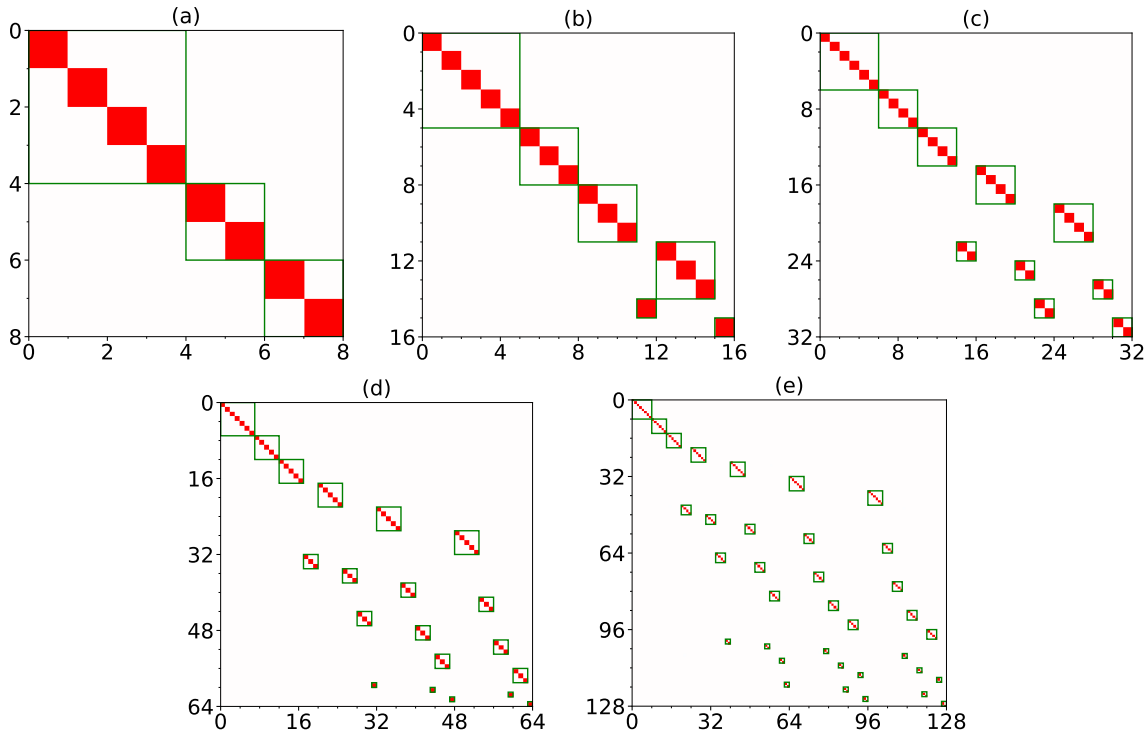

Figure 3.1: **Sparsity plots for $A_S^{\mathbf{Y}\dagger} A_S^{\mathbf{CG}}$ matrices of multi-qubit systems.** (a) 3-qubit system; (b) 4-qubit system; (c) 5-qubit system; (d) 6-qubit system; (e) 7-qubit system. The x- and y-axes denote the column and row indices of the matrix elements, respectively. Each green-colored square box contains an identity matrix. All the elements outside the boxes are zeros.

Table 3.2: Correspondence of good quantum numbers and indices between $\{\mathcal{H}_j^\lambda\}$ and $\{\mathcal{H}_{[J^{(i)}]}^J\}$ in a 6-qubit system

Decomposition method	Young method	CG coefficients of SU(2)
Notation of subspace	$\mathcal{H}_j^\lambda$	$\mathcal{H}_{[J^{(i)}]}^J$
Good quantum number of subspaces	$\lambda = [n-m, m]$	J
Index of subspaces with the same good quantum number	j	$[J^{(i)}] = [J^{(5)}, J^{(4)}, J^{(3)}, J^{(2)}, J^{(1)}, J^{(0)}]$
Dimension of subspace	$n-2m+1$	$2J+1$
Good quantum number	$[6,0]$	3
Index of subspaces	1, $[[1,2,3,4,5,6]]$	$[\frac{1}{2}, 1, \frac{3}{2}, 2, \frac{5}{2}, 3]$
Good quantum number	$[5,1]$	2
Index of subspaces	1, $[[1,2,3,4,5],[6]]$	$[\frac{1}{2}, 1, \frac{3}{2}, 2, \frac{5}{2}, 2]$
	2, $[[1,2,3,4,6],[5]]$	$[\frac{1}{2}, 1, \frac{3}{2}, 2, \frac{3}{2}, 2]$
	3, $[[1,2,3,5,6],[4]]$	$[\frac{1}{2}, 1, \frac{3}{2}, 1, \frac{3}{2}, 2]$
	4, $[[1,2,4,5,6],[3]]$	$[\frac{1}{2}, 1, \frac{1}{2}, 1, \frac{3}{2}, 2]$
	5, $[[1,3,4,5,6],[2]]$	$[\frac{1}{2}, 0, \frac{1}{2}, 1, \frac{3}{2}, 2]$
Good quantum number	$[4,2]$	1
Index of subspaces	1, $[[1,2,3,4],[5,6]]$	$[\frac{1}{2}, 1, \frac{3}{2}, 2, \frac{3}{2}, 1]$
	2, $[[1,2,3,5],[4,6]]$	$[\frac{1}{2}, 1, \frac{3}{2}, 1, \frac{3}{2}, 1]$
	3, $[[1,2,3,6],[4,5]]$	$[\frac{1}{2}, 1, \frac{1}{2}, 1, \frac{1}{2}, 1]$
	4, $[[1,2,4,5],[3,6]]$	$[\frac{1}{2}, 1, \frac{3}{2}, 1, \frac{1}{2}, 1]$
	5, $[[1,2,4,6],[3,5]]$	$[\frac{1}{2}, 1, \frac{1}{2}, 0, \frac{1}{2}, 1]$
	6, $[[1,2,5,6],[3,4]]$	$[\frac{1}{2}, 0, \frac{1}{2}, 1, \frac{1}{2}, 1]$
	7, $[[1,3,4,5],[2,6]]$	$[\frac{1}{2}, 1, \frac{1}{2}, 1, \frac{3}{2}, 1]$
	8, $[[1,3,4,6],[2,5]]$	$[\frac{1}{2}, 0, \frac{1}{2}, 1, \frac{3}{2}, 1]$
	9, $[[1,3,5,6],[2,4]]$	$[\frac{1}{2}, 0, \frac{1}{2}, 0, \frac{1}{2}, 1]$
Good quantum number	$[3,3]$	0
Index of subspaces	1, $[[1,2,3],[4,5,6]]$	$[\frac{1}{2}, 1, \frac{3}{2}, 1, \frac{1}{2}, 0]$
	2, $[[1,2,4],[3,5,6]]$	$[\frac{1}{2}, 1, \frac{1}{2}, 1, \frac{1}{2}, 0]$
	3, $[[1,2,5],[3,4,6]]$	$[\frac{1}{2}, 0, \frac{1}{2}, 1, \frac{1}{2}, 0]$
	4, $[[1,3,4],[2,5,6]]$	$[\frac{1}{2}, 1, \frac{1}{2}, 0, \frac{1}{2}, 0]$
	5, $[[1,3,5],[2,4,6]]$	$[\frac{1}{2}, 0, \frac{1}{2}, 0, \frac{1}{2}, 0]$

The index of subspaces j is not well-defined. I can rearrange the order of the diagonal elements in any representation of S_n with a similarity transformation. Therefore, I pursue an index that is invariant under the similarity transformation of group representations. Note that the subspace $\mathcal{H}_j^\lambda$ is generated with the group algebra element O_j^λ corresponding to a standard Young tableau T_j^λ with the shape λ. Here I record the Young tableau T_j^λ as a two-row list in addition to the index j, which is defined by sorting T_j^λ.

As shown in Table 3.2, I conclude that the Young method and the CG coefficients of SU(2) lead to the same decomposition of $\mathcal{H}(\mathbb{C}^{2^n})$, and the same transformation of the Hamiltonians H_x, H_y, H_z, whereas the CG coefficients method takes much less time, as shown in Table 3.1. In this work, I preferably use the CG coefficients of SU(2) to generate the adjoint matrix A_S that transforms the Hamiltonians in Eqs. 2.3 and 2.5.

Although the Young method is cumbersome for transforming Hamiltonians with S_n symmetry, it does imply that Hamiltonians with other types of finite group symmetries may be transformed in a similar way (i.e., to act the group algebra elements on some proper Fock states). In the following section, I introduce how Hamiltonians with D_n symmetry in Eq. 2.4 can be transformed with the group algebra elements of $\mathcal{R}_{D_n}$.

3.3 Transformation of the Hamiltonians of D_n Symmetry

The dihedral group D_n is the finite group describing the symmetry of a regular polygon with n vertices. D_n has $2n$ group elements, with n rotational and n reflective elements. The last term in Eq. 2.4 has D_n symmetry since it is invariant under the rotations of the indices $\{i \in \mathbb{N} | 1 \leq i \leq n\}$, which are defined as

$$\begin{aligned} & i \mapsto (i+k) \bmod n && \text{if } (i+k) \bmod n \neq 0; \\ & i \mapsto n && \text{if } (i+k) \bmod n = 0, \\ & 1 \leq i \leq n, 0 \leq k \leq n-1, \end{aligned} \tag{3.15}$$

and the reflections of the indices, which are defined as

$$\begin{aligned} &i \mapsto (n+k-i) \bmod n \qquad \text{if } (n+k-i) \bmod n \neq 0; \\ &i \mapsto n \qquad\qquad\qquad\qquad\quad \text{if } (n+k-i) \bmod n = 0, \\ &1 \leq i \leq n, 0 \leq k \leq n-1. \end{aligned} \tag{3.16}$$

One intuitive way to understand D_n symmetry is to position each qubit at the vertices of a n-gon and take the edges as the coupling between nearest neighbors. It should be noted that Eqs. 2.3 and 2.5 also have D_n symmetry since D_n is a subgroup of S_n. Therefore, the adjoint matrices block diagonalizing the coupling Hamiltonian, $H_{\text{cpl}} = \sum_{i=1}^{n} \sigma_z^{(i)} \sigma_z^{(i+1)}$, should block diagonalize H_x, H_y, and H_z as well. I provide the details about how to generate the adjoint matrices with the irreps of D_n as follows.

The $2n$ elements of the D_n group are in $\frac{n+3}{2}$ conjugate classes if n is odd or $\frac{n}{2}+3$ conjugate classes if n is even. Accordingly, the D_n group has the same number of inequivalent irreps. The character tables of D_n are given in Tables 3.3 and 3.4.

Table 3.3: Character table of the D_n group for odd n

	Conjugate class		
Irrep	$\{e_0\}$ $(1,1)$	$\{C_n^k, C_n^{n-k}\}$ $(2, \frac{n-1}{2})$	$\{C_2^{(k)}\}$ $(n,1)$
Identity (1)	1	1	1
C_n (1)	1	1	-1
$\theta_1 = \frac{2\pi}{n}$ (2)	2	$2\cos(k\theta_1)$	0
$\vdots$	$\vdots$	$\vdots$	$\vdots$
$\theta_j = \frac{2\pi j}{n}$ (2)	2	$2\cos(k\theta_j)$	0
$\vdots$	$\vdots$	$\vdots$	$\vdots$
$\theta_{\frac{n-1}{2}} = \frac{\pi(n-1)}{n}$ (2)	2	$2\cos(k\theta_{\frac{n-1}{2}})$	0

Three types of conjugate classes exist: (1) the identity element $\{e_0\}$, (2) rotations $\{C_n^k, C_n^{n-k}\}, 1 \leq k \leq \frac{n-1}{2}$, and (3) reflections $\{C_2^{(k)} | 0 \leq k \leq n-1\}$. The numbers in the bracket next to the conjugate classes are the number of elements in the class and the number of classes of that type. The irreps are 1- or 2-dimensional. Besides the identity irrep, the other 1-dimensional irrep is formed by the fact that the cyclic group C_n is an invariant subgroup of D_n. The $\frac{n-1}{2}$ of 2-dimensional irreps are characterized by $\theta_j, 1 \leq j \leq \frac{n-1}{2}$. The number in the bracket next to the irreps is the dimension of the irrep.

The 2-dimensional irreps of D_n can be constructed in the following way. In the $\theta_j = \frac{2\pi j}{n}$ representation,

$$
\begin{aligned}
A(C_n^k) &= \begin{pmatrix} \cos(k\theta_j) & -\sin(k\theta_j) \\ \sin(k\theta_j) & \cos(k\theta_j) \end{pmatrix}, \\
A(C_2^{(k)}) &= \begin{pmatrix} \cos(k\theta_j) & \sin(k\theta_j) \\ \sin(k\theta_j) & -\cos(k\theta_j) \end{pmatrix}, \\
C_n^0 &= e_0, 0 \leq k \leq n-1.
\end{aligned}
\tag{3.17}
$$

Table 3.4: Character table of the D_n group for even n

Irrep	Conjugate class				
	$\{e_0\}$ $(1,1)$	$\{C_n^k, C_n^{n-k}\}$ $(2, \frac{n-2}{2})$	$\{C_n^{\frac{n}{2}}\}$ $(1,1)$	$\{C_2^{(k)}\}$ $(\frac{n}{2},1)$	$\{C_2^{(k')}\}$ $(\frac{n}{2},1)$
Identity (1)	1	1	1	1	1
C_n (1)	1	1	1	-1	-1
$D_{\frac{n}{2}}$ (1)	1	1 if k is even -1 if k is odd	1 if $\frac{n}{2}$ is even -1 if $\frac{n}{2}$ is odd	-1	1
$D'_{\frac{n}{2}}$ (1)	1	1 if k is even -1 if k is odd	1 if $\frac{n}{2}$ is even -1 if $\frac{n}{2}$ is odd	1	-1
$\theta_1 = \frac{2\pi}{n}$ (2)	2	$2\cos(k\theta_1)$	-2	0	0
$\vdots$	$\vdots$	$\vdots$	$\vdots$	$\vdots$	$\vdots$
$\theta_j = \frac{2\pi j}{n}$ (2)	2	$2\cos(k\theta_j)$	$2\cos(j\pi)$	0	0
$\vdots$	$\vdots$	$\vdots$	$\vdots$	$\vdots$	$\vdots$
$\theta_{\frac{n-2}{2}} = \frac{\pi(n-2)}{n}$ (2)	2	$2\cos(k\theta_{\frac{n-2}{2}})$	$2\cos(\frac{n-2}{2}\pi)$	0	0

Five types of conjugate classes exist: (1) the identity element $\{e_0\}$, (2) rotations $\{C_n^k, C_n^{n-k}\}, 1 \leq k \leq \frac{n-2}{2}$, (3) rotation $\{C_n^{\frac{n}{2}}\}$, (4) reflections changing all the indices of the qubits $\{C_2^{(k)} | k = 2l, 0 \leq l \leq \frac{n}{2} - 1\}$, and (5) reflections keeping two indices of the qubits unchanged $\{C_2^{(k')} | k' = 2l + 1, 0 \leq l \leq \frac{n}{2} - 1\}$. The numbers in the bracket next to the conjugate classes are the number of elements in the class and the number of classes of that type. The irreps are 1- or 2-dimensional. Besides the identity irrep, the other 1-dimensional irreps are formed by the fact that the cyclic group C_n and $D_{\frac{n}{2}}$ are invariant subgroups of D_n. The $\frac{n-2}{2}$ of 2-dimensional irreps are characterized by $\theta_j, 1 \leq j \leq \frac{n-2}{2}$. The number in the bracket next to the irreps is the dimension of the irrep.

Here I clarify the definition of C_n^k and $C_2^{(k)}$ with their action on the sequence of the indices of qubits $[1, 2, 3, \ldots, j, \ldots, n]$:

$$\begin{aligned} C_n^k \cdot [1, 2, 3, \ldots, n-1, n] &\mapsto [1+k, 2+k, \ldots, n-1, n, 1, 2, \ldots, k-1, k], \\ C_2^{(k)} \cdot [1, 2, 3, \ldots, n-1, n] &\mapsto [k, k-1, \ldots, 2, 1, n, n-1, \ldots, 2+k, 1+k], \\ C_2^{(k)} &= R \circ C_n^k, 0 \leq k \leq n-1, \end{aligned} \tag{3.18}$$

where R is the action reversing the sequence and $\circ$ is the group operation. It is easy to verify that the matrices defined in Eq. 3.17 form the $\theta_j = \frac{2\pi j}{n}$ 2-dimensional representation and are compatible with the character tables in Tables 3.3 and 3.4.

Similar to the procedure in Sec. 3.1, I construct the elements

$$O_j^\theta = \sum_{i=1}^{2n} A_{jj}^\theta(e_i) e_i, \ 1 \leq j \leq d_\theta \tag{3.19}$$

in the group algebra $\mathcal{R}_{D_n}$ for each unitary irrep A^θ. Here $\theta \in \{\mathrm{Id}, C_n, \theta_1, \ldots, \theta_{\frac{n-1}{2}}\}$ (for odd n) or $\theta \in \{\mathrm{Id}, C_n, D_{\frac{n}{2}}, D'_{\frac{n}{2}}, \theta_1, \ldots, \theta_{\frac{n-2}{2}}\}$ (for even n) is the index identifying the irrep, and $A_{jj}^\theta(e_i)$ is the jth diagonal element in the representation $A^\theta(e_i)$ of the element $e_i \in D_n$, and $d_\theta = 1$ or 2 is the dimension of the representation A^θ. It is trivial to show there are $n+1$ elements if n is odd, or $n+2$ elements if n is even, in the group algebra $\mathcal{R}_{D_n}$. These elements can be regarded as operators acting on the Fock basis. With the group actions defined in the mapping in Eq. 3.18, the action of any $e \in D_n$ on any Fock state

$|s_1, s_2, s_3, \ldots, s_i, \ldots, s_n\rangle \in \{|\uparrow\rangle, |\downarrow\rangle\}^{\otimes n}$ can be defined as

$$\begin{aligned} C_n^k \cdot |s_1, s_2, s_3, \ldots, s_{n-1}, s_n\rangle &\mapsto |s_{1+k}, s_{2+k}, \ldots, s_{n-1}, s_n, s_1, s_2, \ldots, s_{k-1}, s_k\rangle, \\ C_2^{(k)} \cdot |s_1, s_2, s_3, \ldots, s_{n-1}, s_n\rangle &\mapsto |s_k, s_{k-1}, \ldots, s_2, s_1, s_n, s_{n-1}, \ldots, s_{2+k}, s_{1+k}\rangle, \\ 0 \leq k \leq n-1, s_i &\in \{|\uparrow\rangle, |\downarrow\rangle\}, 1 \leq i \leq n. \end{aligned} \tag{3.20}$$

The action of the operator $O_j^\theta = \sum_{i=1}^{2n} A_{jj}^\theta(e_i)e_i$ is the linear combination of the action of each $e_i \in D_n$, i.e.,

$$O_j^\theta \cdot |s_1, s_2, s_3, \ldots, s_i, \ldots, s_n\rangle = \sum_{i=1}^{2n} A_{jj}^\theta(e_i)(e_i \cdot |s_1, s_2, s_3, \ldots, s_i, \ldots, s_n\rangle). \tag{3.21}$$

With respect to the group action of D_n, $\{|\uparrow\rangle, |\downarrow\rangle\}^{\otimes n}$ is decomposed into orbits. Since D_n has rotation and reflection elements only, it is not guaranteed that any two elements in the set $\{|s_1, s_2, s_3, \ldots, s_i, \ldots, s_n\rangle \mid s_i = \uparrow, \downarrow; m \text{ of } \uparrow, (n-m) \text{ of } \downarrow\}$ are equivalent to each other. Therefore, the set above is typically not an orbit of $\{|\uparrow\rangle, |\downarrow\rangle\}^{\otimes n}$ under the group action of D_n. However, it is trivial to show that the orbit $D_n \cdot |s_1, \ldots, s_n\rangle$ is a subset of the orbit $S_n \cdot |s_1, \ldots, s_n\rangle$ since any D_n action also does not convert a spin-up to a spin-down or vice versa but only rearranges the spins. In other words, the fact that D_n is a subgroup of S_n results in the D_n orbits being subsets of the S_n orbits.

With the orbit-stabilizer theorem [63], I claim that for any $|s_1, \ldots, s_n\rangle \in \{|\uparrow\rangle, |\downarrow\rangle\}^{\otimes n}$, the number of elements in the orbit $D_n \cdot |s_1, \ldots, s_n\rangle$ is either a factor of n if $C_n \cdot |s_1, \ldots, s_n\rangle = (D_n \backslash C_n) \cdot |s_1, \ldots, s_n\rangle$ or a factor of $2n$ if $C_n \cdot |s_1, \ldots, s_n\rangle \cap (D_n \backslash C_n) \cdot |s_1, \ldots, s_n\rangle = \varnothing$. Here, $D_n \backslash C_n = R \circ C_n$ is the difference of D_n and C_n. The Hilbert space

$\mathcal{H}(\mathbb{C}^{2^n})$ is decomposed into subspaces by acting each operator O_j^θ on some proper element(s) in the orbits. If $C_n \cdot |s_1, \ldots, s_n\rangle = (D_n \backslash C_n) \cdot |s_1, \ldots, s_n\rangle$, each operator O_j^θ acts on no more than one element in each orbit. In contrast, if $C_n \cdot |s_1, \ldots, s_n\rangle \cap (D_n \backslash C_n) \cdot |s_1, \ldots, s_n\rangle = \varnothing$, each operator O_j^θ acts on zero or two elements in each orbit. Following the procedure above, the orthogonal basis of all the subspaces is generated. Each subspace is defined by the group action of the operator O_j^θ, and I denote that subspace as $\mathcal{H}_j^\theta$. I then normalize the orthogonal basis in each subspace $\mathcal{H}_j^\theta$ and let them be the columns of such a unitary matrix A_D such that the basis of each particular subspace is positioned together. All the orthonormal basis vectors are the eigenstates of H_{cpl} and H_z. Therefore, after the unitary similarity transformation with the adjoint matrix A_D, $H'_{\text{cpl}} = A_D^\dagger H_{\text{cpl}} A_D$ and $H'_z = A_D^\dagger H_z A_D$ remain diagonal, while $H'_x = A_D^\dagger H_x A_D$ and $H'_y = A_D^\dagger H_y A_D$ are block diagonal. It should be noted that the dimensions of the subspaces in the decomposition

$$\mathcal{H}(\mathbb{C}^{2^n}) = \bigoplus_{\theta,j} \mathcal{H}_j^\theta \tag{3.22}$$

are generally larger than those in the decomposition in Eq. 3.13. In fact, the dimension of $\mathcal{H}_1^{[n]}$ in the S_n decomposition is $\sim O(n)$, whereas the dimension of $\mathcal{H}_1^{\text{Id}}$ in the D_n decomposition is $\sim O(\frac{2^n}{n})$. Therefore, the sizes of the blocks in H'_x and H'_y after the D_n transformation (which are equal to the dimensions of the subspaces) are generally larger than those corresponding to the S_n-induced transformation. Table 4.1 in Sec. 4.1 shows a comparison of the dimensions of $\mathcal{H}(\mathbb{C}^{2^n})$, $\mathcal{H}_1^{[n]}$, $\mathcal{H}_1^{\text{Id}}$ for $3 \leq n \leq 14$.

Similar to what I concluded in Sec. 3.1, with the Hamiltonians in Eqs. 2.4 and 2.5 block diagonalized with the D_n-induced unitary similarity transformation, it is clear that

the evolution of a pure state $|\psi\rangle$ in any subspace $\mathcal{H}_j^\theta$ is strictly confined within that subspace regardless of the temporal forms of the control pulses $B_x(t)$ and $B_y(t)$. Furthermore, if the initial state is defined as a linear combination of states in multiple subspaces, i.e.,

$$|\psi(0)\rangle = \sum_{\theta,j} c_j^\theta |\psi_j^\theta(0)\rangle, c_j^\theta \in \mathbb{C}, |\psi_j^\theta(0)\rangle \in \mathcal{H}_j^\theta, \tag{3.23}$$

the final state must also be in those subspaces with the same probabilities, i.e.,

$$|\psi(T)\rangle = \sum_{\theta,j} c'^\theta_j |\psi_j^\theta(T)\rangle, c'^\theta_j \in \mathbb{C}, |\psi_j^\theta(T)\rangle \in \mathcal{H}_j^\theta, \|c'^\theta_j\| = \|c_j^\theta\|. \tag{3.24}$$

Since the subspaces $\{\mathcal{H}_j^\theta\}$ are characterized by θ, I conclude that θ is a good quantum number in a multi-qubit system with D_n symmetry. It is worth noting that θ is no longer equivalent to the total spin angular momentum J; however, it can be shown that the angular momentum projection onto the z-axis M is still a good quantum number for the eigenstates of H_0 in Eq. 2.4. For S_n symmetry, where each $M \in \{-J, -J+1, \ldots, J-1, J\}$, there is only one eigenstate characterized with M in each subspace $\mathcal{H}^J_{[J^{(i)}]}$. In contrast, for D_n symmetry, there may be more than one eigenstate characterized by the same M in each subspace $\mathcal{H}_j^\theta$. It should be noted that H_x and H_y have S_n symmetry and change M by ± 1. One consequence is that there may be nonzero elements not only in the minor diagonals closest to the main diagonal but also in further minor diagonals in the blocks of $H'_x = A_D^\dagger H_x A_D$ and $H'_y = A_D^\dagger H_y A_D$ (see Figs. 4.1, 4.2, 4.3, 4.4, and 4.5 in Sec. 4.1). I discuss the profile of H'_x and H'_y with the theory of creation/annihilation operators in Sec. 5.2.

3.4 Mathematical Proof of the Orthogonality and Completeness of the Basis Vectors Generated by the D_n-Induced Decomposition of the Hilbert Space

In this subsection, I show that the basis vectors generated in the procedure in Sec. 3.3 are orthogonal and complete in the Hilbert space $\mathcal{H}(\mathbb{C}^{2^n})$. For the proof, I construct the following complex 2-dimensional irreps of D_n. In the $\theta_j = \frac{2\pi j}{n}$ representation,

$$\begin{aligned} A(C_n^k) &= \begin{pmatrix} \exp(ik\theta_j) & 0 \\ 0 & \exp(-ik\theta_j) \end{pmatrix}, \\ A(C_2^{(k)}) &= \begin{pmatrix} 0 & \exp(ik\theta_j) \\ \exp(-ik\theta_j) & 0 \end{pmatrix}, \\ C_n^0 &= e_0, 0 \leq k \leq n-1, \end{aligned} \tag{3.25}$$

where i is the imaginary unit. The same as in Eq. 3.18, I clarify the definition of C_n^k and $C_2^{(k)}$ with their action on the sequence of the indices of qubits $[1, 2, 3, \ldots, j, \ldots, n]$:

$$\begin{aligned} C_n^k \cdot [1, 2, 3, \ldots, n-1, n] &\mapsto [1+k, 2+k, \ldots, n-1, n, 1, 2, \ldots, k-1, k]; \\ C_2^{(k)} \cdot [1, 2, 3, \ldots, n-1, n] &\mapsto [k, k-1, \ldots, 2, 1, n, n-1, \ldots, 2+k, 1+k], \\ C_2^{(k)} &= R \circ C_n^k, 0 \leq k \leq n-1, \end{aligned} \tag{3.26}$$

where R is the action reversing the sequence and $\circ$ is the group operation. It is straightforward to verify that the matrices defined in Eq. 3.25 form the $\theta_j = \frac{2\pi j}{n}$, 2-dimensional

representation and are compatible with the character tables in Tables 3.3 and 3.4. This complex irrep makes the proof simpler.

Lemma 1. For any $|s_1, \ldots, s_n\rangle \in \{|\uparrow\rangle, |\downarrow\rangle\}^{\otimes n}$, $C_n \cdot |s_1, \ldots, s_n\rangle$ and $(D_n \backslash C_n) \cdot |s_1, \ldots, s_n\rangle$ either are the same set or have no element in common.

Proof. Note that the reflection elements are defined by $C_2^{(k)} = R \circ C_n^k$. Then $R = R \circ e_0$ is also a reflection element. Considering that C_n is an invariant subgroup of D_n, all the reflection elements form the coset $R \circ C_n = C_n \circ R = D_n \backslash C_n$.

If $R \cdot |s_1, \ldots, s_n\rangle \in C_n \cdot |s_1, \ldots, s_n\rangle$, I obviously have $(D_n \backslash C_n) \cdot |s_1, \ldots, s_n\rangle = (C_n \circ R) \cdot |s_1, \ldots, s_n\rangle = C_n \cdot (R \cdot |s_1, \ldots, s_n\rangle) = C_n \cdot |s_1, \ldots, s_n\rangle$.

Otherwise, if $R \cdot |s_1, \ldots, s_n\rangle \notin C_n \cdot |s_1, \ldots, s_n\rangle$, I have $(D_n \backslash C_n) \cdot |s_1, \ldots, s_n\rangle = (C_n \circ R) \cdot |s_1, \ldots, s_n\rangle = C_n \cdot (R \cdot |s_1, \ldots, s_n\rangle)$. Assume that some element $C_n^k \cdot (R \cdot |s_1, \ldots, s_n\rangle) \in C_n \cdot |s_1, \ldots, s_n\rangle$; then $(C_n^k)^{-1} \cdot (C_n^k \cdot (R \cdot |s_1, \ldots, s_n\rangle)) = ((C_n^k)^{-1} \circ C_n^k) \cdot (R \cdot |s_1, \ldots, s_n\rangle) = R \cdot |s_1, \ldots, s_n\rangle$ is in $(C_n^k)^{-1} \cdot (C_n \cdot |s_1, \ldots, s_n\rangle) = ((C_n^k)^{-1} \circ C_n) \cdot |s_1, \ldots, s_n\rangle = C_n \cdot |s_1, \ldots, s_n\rangle$, which is contradictory with $R \cdot |s_1, \ldots, s_n\rangle \notin C_n \cdot |s_1, \ldots, s_n\rangle$. I can then conclude that $(D_n \backslash C_n) \cdot |s_1, \ldots, s_n\rangle$ and $C_n \cdot |s_1, \ldots, s_n\rangle$ have no element in common if $R \cdot |s_1, \ldots, s_n\rangle \notin C_n \cdot |s_1, \ldots, s_n\rangle$.

Lemma 2. For any element $O_j^\theta = \sum_{i=1}^{2n} A_{jj}^\theta(e_i) e_i$ in the group algebra $\mathcal{R}_{D_n}$ as an operator on $|s_1, \ldots, s_n\rangle \in \{|\uparrow\rangle, |\downarrow\rangle\}^{\otimes n}$ as defined in Eq. 3.21, considering two different elements $|s_1', \ldots, s_n'\rangle$ and $|s_1'', \ldots, s_n''\rangle$ in $C_n \cdot |s_1, \ldots, s_n\rangle$, I have $O_j^\theta \cdot |s_1', \ldots, s_n'\rangle = c \times O_j^\theta \cdot |s_1'', \ldots, s_n''\rangle$, where $c \in \mathbb{C}$ is a complex coefficient that can be zero.

Proof. I discuss the operators O_j^θ by their corresponding irreps.

In the situation of the identity irrep, $O^{\mathrm{Id}} = \sum_{i=1}^{2n} e_i$. Obviously, for any element $|s'_1, \ldots, s'_n\rangle \in D_n \cdot |s_1, \ldots, s_n\rangle$, $O^{\mathrm{Id}} \cdot |s'_1, \ldots, s'_n\rangle$ is the same.

In the situation of the C_n irrep, $O^{C_n} = \sum_{i=1}^{n} e_i - \sum_{i=n+1}^{2n} e_i$, where the elements in the first sum are rotations, and the elements in the second sum are reflections. Obviously, for any $|s'_1, \ldots, s'_n\rangle \in C_n \cdot |s_1, \ldots, s_n\rangle$, $O^{C_n} \cdot |s'_1, \ldots, s'_n\rangle$ is a zero vector if $C_n \cdot |s_1, \ldots, s_n\rangle = (D_n \backslash C_n) \cdot |s_1, \ldots, s_n\rangle$. Otherwise, for any $|s'_1, \ldots, s'_n\rangle \in C_n \cdot |s_1, \ldots, s_n\rangle$, $O^{C_n} \cdot |s'_1, \ldots, s'_n\rangle$ is the same if $C_n \cdot |s_1, \ldots, s_n\rangle \cap (D_n \backslash C_n) \cdot |s_1, \ldots, s_n\rangle = \varnothing$.

When n is even, I need to discuss the two irreps formed by the fact that $D_{\frac{n}{2}}$ is an invariant subgroup of D_n. Following the notations in Table 3.4, I take these two operators as $O^{D_{\frac{n}{2}}} = \sum_{i=1}^{2n} A^{D_{\frac{n}{2}}}(e_i) e_i$ and $O^{D'_{\frac{n}{2}}} = \sum_{i=1}^{2n} A^{D'_{\frac{n}{2}}}(e_i) e_i$. Note that 1 and -1 appear alternately as the coefficients of the C_n elements and the $D_n \backslash C_n$ elements. Also, $C_n \cdot |s_1, \ldots, s_n\rangle$ and $(D_n \backslash C_n) \cdot |s_1, \ldots, s_n\rangle$ always have the same number of elements. Then for any $|s'_1, \ldots, s'_n\rangle \in C_n \cdot |s_1, \ldots, s_n\rangle$, $O^{D_{\frac{n}{2}}} \cdot |s'_1, \ldots, s'_n\rangle$ and $O^{D'_{\frac{n}{2}}} \cdot |s'_1, \ldots, s'_n\rangle$ must be zero vectors if $C_n \cdot |s_1, \ldots, s_n\rangle$ has an odd number of elements.

For $O^{D_{\frac{n}{2}}} \cdot |s'_1, \ldots, s'_n\rangle$ or $O^{D'_{\frac{n}{2}}} \cdot |s'_1, \ldots, s'_n\rangle$ to be a nonzero vector, I also need to ensure that the coefficients of the C_n elements and those of the $D_n \backslash C_n$ elements, appearing as 1 and -1, do not cancel each other. If $C_n \cdot |s_1, \ldots, s_n\rangle \cap (D_n \backslash C_n) \cdot |s_1, \ldots, s_n\rangle = \varnothing$, it is obvious that those coefficients will not cancel each other since they are the coefficients of the elements in the two different sets $C_n \cdot |s_1, \ldots, s_n\rangle$ and $(D_n \backslash C_n) \cdot |s_1, \ldots, s_n\rangle$. Acting $O^{D_{\frac{n}{2}}}$ or $O^{D'_{\frac{n}{2}}}$ on other elements $|s''_1, \ldots, s''_n\rangle \in C_n \cdot |s_1, \ldots, s_n\rangle$ will result in a collinear basis vector with a global phase factor of 1 or -1.

I then discuss the situation of $C_n \cdot |s_1, \ldots, s_n\rangle = (D_n \backslash C_n) \cdot |s_1, \ldots, s_n\rangle$ where each has an even number of elements. In this case, there must be an element $C_n^k \in C_n$ such that $C_n^k \cdot |s'_1, \ldots, s'_n\rangle = R \cdot |s'_1, \ldots, s'_n\rangle$, where $R \in D_n \backslash C_n$ is the element reversing the sequence $|s'_1, \ldots, s'_n\rangle$. I notice that, following the notations in Table 3.4, the element R is in the conjugate class $C_2^{(k)}$. For the case that the coefficient of C_n^k is 1, $O^{D_{\frac{n}{2}}} \cdot |s'_1, \ldots, s'_n\rangle$ is a zero vector, and $O^{D'_{\frac{n}{2}}} \cdot |s'_1, \ldots, s'_n\rangle$ is a nonzero vector. Otherwise, if the coefficient of C_n^k is -1, $O^{D_{\frac{n}{2}}} \cdot |s'_1, \ldots, s'_n\rangle$ is a nonzero vector, and $O^{D'_{\frac{n}{2}}} \cdot |s'_1, \ldots, s'_n\rangle$ is a zero vector. Acting $O^{D_{\frac{n}{2}}}$ or $O^{D'_{\frac{n}{2}}}$ on other elements $|s''_1, \ldots, s''_n\rangle \in C_n \cdot |s_1, \ldots, s_n\rangle$ will result in a collinear basis vector with a global phase factor of 1 or -1.

I now discuss the last situation where O_j^θ is generated by the diagonal elements in the 2-dimensional irrep. With the irreps as constructed in Eq. 3.25, the operators become $O_j^\theta = \sum_{i=1}^n A_{jj}^\theta(e_i)e_i$.

I first discuss the operators $O_1^{\theta_j} = \sum_{k=0}^{n-1} \exp(ik\theta_j)C_n^k$. It is trivial to see that the number of elements in the set $\{\exp(ik\theta_j)|0 \leq k \leq n-1, \theta_j = \frac{2\pi j}{n}\}$ must be a factor of n if it is noticed that $C_n^k \mapsto \exp(ik\theta_j)$ is an irrep of C_n. Per the orbit-stabilizer theorem [63], the number of elements in $C_n \cdot |s_1, \ldots, s_n\rangle$ is also a factor of n. Denoting the number of elements in $C_n \cdot |s_1, \ldots, s_n\rangle$ as d, the group actions of $C_n^0, C_n^d, \ldots, C_n^{n-d}$ will keep $|s'_1, \ldots, s'_n\rangle$ unchanged. In $O_1^{\theta_j} \cdot |s'_1, \ldots, s'_n\rangle$, the coefficient of $|s'_1, \ldots, s'_n\rangle$ will be $1 + \exp(id\theta_j) + \cdots + \exp(i(n-d)\theta_j)$. This coefficient is nonzero if and only if $d\theta_j$ is a multiple of 2π, or equivalently, if and only if the number of elements in $\{\exp(ik\theta_j)|0 \leq k \leq n-1, \theta_j = \frac{2\pi j}{n}\}$ is a factor of the number of elements in $C_n \cdot |s_1, \ldots, s_n\rangle$. In fact,

$1, \exp(id\theta_j), \ldots, \exp(i(n-d)\theta_j)$ are equally spaced complex numbers on the unit circle in the complex plane, and they sum up to zero if $d\theta_j$ is not a multiple of 2π.

The coefficient of another $|s_1'', \ldots, s_n''\rangle \in C_n \cdot |s_1, \ldots, s_n\rangle$ in $O_1^{\theta_j} \cdot |s_1', \ldots, s_n'\rangle$ is $\exp(ik'\theta_j) + \exp(i(d+k')\theta_j) + \cdots + \exp(i(n-d+k')\theta_j)$, which is $\exp(ik'\theta_j)$ multiplied by the sum in the previous paragraph, where $C_n^{k'} \cdot |s_1', \ldots, s_n'\rangle = |s_1'', \ldots, s_n''\rangle$. The condition for this coefficient to be zero is the same as that given in the last paragraph. In conclusion, I claim that for any $|s_1', \ldots, s_n'\rangle \in C_n \cdot |s_1, \ldots, s_n\rangle$, $O_1^{\theta_j} \cdot |s_1', \ldots, s_n'\rangle$ is a nonzero vector if and only if the number of elements in $\{\exp(ik\theta_j) | 0 \leq k \leq n-1, \theta_j = \frac{2\pi j}{n}\}$ is a factor of the number of elements in $C_n \cdot |s_1, \ldots, s_n\rangle$.

The discussion of the operators $O_2^{\theta_j} = \sum_{k=0}^{n-1} \exp(-ik\theta_j) C_n^k$ is similar if it is noticed that $\exp(-ik\theta_j)$ is the complex conjugate of $\exp(ik\theta_j)$. For any $|s_1', \ldots, s_n'\rangle \in C_n \cdot |s_1, \ldots, s_n\rangle$, $O_2^{\theta_j} \cdot |s_1', \ldots, s_n'\rangle$ is a nonzero vector if and only if the number of elements in $\{\exp(-ik\theta_j) | 0 \leq k \leq n-1, \theta_j = \frac{2\pi j}{n}\}$ is a factor of the number of elements in $C_n \cdot |s_1, \ldots, s_n\rangle$. When $O_1^{\theta_j} \cdot |s_1', \ldots, s_n'\rangle$ and $O_2^{\theta_j} \cdot |s_1', \ldots, s_n'\rangle$ are nonzero, acting $O_1^{\theta_j}$ or $O_2^{\theta_j}$ on another $|s_1'', \ldots, s_n''\rangle \in C_n \cdot |s_1, \ldots, s_n\rangle$ will result in collinear basis vectors with a global phase factor of $\exp(ik'\theta_j)$ or $\exp(-ik'\theta_j)$, respectively, where $C_n^{k'} \cdot |s_1', \ldots, s_n'\rangle = |s_1'', \ldots, s_n''\rangle$. When $C_n \cdot |s_1, \ldots, s_n\rangle \cap (D_n \backslash C_n) \cdot |s_1, \ldots, s_n\rangle = \varnothing$, the operators $O_1^{\theta_j}$ or $O_2^{\theta_j}$ need to act on two elements in $D_n \cdot |s_1, \ldots, s_n\rangle$ to generate two basis vectors: one element in $C_n \cdot |s_1, \ldots, s_n\rangle$ and the other in $(D_n \backslash C_n) \cdot |s_1, \ldots, s_n\rangle$.

Corollary. Each group algebra element O_j^θ necessarily acts on zero or one element in the orbit $D_n \cdot |s_1, \ldots, s_n\rangle$ if $C_n \cdot |s_1, \ldots, s_n\rangle = (D_n \backslash C_n) \cdot |s_1, \ldots, s_n\rangle$; or it necessarily acts on zero or two elements in the orbit if $C_n \cdot |s_1, \ldots, s_n\rangle \cap (D_n \backslash C_n) \cdot |s_1, \ldots, s_n\rangle = \varnothing$ to

generate the basis vectors. Acting the operator on other elements in the orbit generates a zero vector or a collinear basis vector with no other difference than a global phase factor.

I am now ready to show that these generated basis vectors are orthogonal and complete in the Hilbert space $\mathcal{H}(\mathbb{C}^{2^n})$.

Orthogonality. When two different group algebra elements O_j^θ and $O_{j'}^{\theta'}$ in Eq. 3.19 act on two elements $|s_1, \ldots, s_n\rangle$ and $|s'_1, \ldots, s'_n\rangle$ in two different orbits, respectively, it is obvious that

$$(\langle s'_1, \ldots, s'_n | O_{j'}^{\theta'})(O_j^\theta | s_1, \ldots, s_n\rangle) = 0 \tag{3.27}$$

because $O_j^\theta |s_1, \ldots, s_n\rangle$ and $O_{j'}^{\theta'} |s'_1, \ldots, s'_n\rangle$ are in two orthogonal subspaces spanned by the two different orbits.

I discuss the case that the elements $|s_1, \ldots, s_n\rangle$ and $|s'_1, \ldots, s'_n\rangle$ are in the same orbit $D_n \cdot |s''_1, \ldots, s''_n\rangle$. If O_j^θ and $O_{j'}^{\theta'}$ are both formed by 2-dimensional irreps, obviously, Eq. 3.27 holds when $|s_1, \ldots, s_n\rangle \in C_n \cdot |s''_1, \ldots, s''_n\rangle$ and $|s'_1, \ldots, s'_n\rangle \in (D_n \backslash C_n) \cdot |s''_1, \ldots, s''_n\rangle$. Otherwise, if $|s_1, \ldots, s_n\rangle$ and $|s'_1, \ldots, s'_n\rangle$ are both in $C_n \cdot |s''_1, \ldots, s''_n\rangle$ or $(D_n \backslash C_n) \cdot |s''_1, \ldots, s''_n\rangle$, without loss of generality, I can assume that $|s_1, \ldots, s_n\rangle = |s'_1, \ldots, s'_n\rangle$ since it results in no other difference than a global phase factor. Letting $O_j^\theta = \sum_{i=1}^n A_{jj}^\theta(e_i) e_i$ and $O_{j'}^{\theta'} = \sum_{i=1}^n A_{j'j'}^{\theta'}(e_i) e_i$, the left-hand side of Eq. 3.27 becomes $\sum_{i=1}^n (A_{jj}^\theta(e_i) A_{j'j'}^{\theta'}(e_i))$. I can easily see that this is zero with the Schur orthogonality of the irreps of finite groups [60, 61, 62].

When at least one of the operators is formed by 1-dimensional irreps, without loss of generality, I can still assume that $|s_1, \ldots, s_n\rangle = |s'_1, \ldots, s'_n\rangle$ in the orbit $D_n \cdot |s''_1, \ldots, s''_n\rangle$ since it results in no other difference than a global phase factor. Letting $O_j^\theta = \sum_{i=1}^{2n} A_{jj}^\theta(e_i) e_i$

and $O^{\theta'}_{j'} = \sum_{i=1}^{2n} A^{\theta'}_{j'j'}(e_i)e_i$, the left-hand side of Eq. 3.27 becomes $\sum_{i=1}^{2n}(A^{\theta}_{jj}(e_i)A^{\theta'}_{j'j'}(e_i))$. Again, I directly determine that this is zero with the Schur orthogonality.

Completeness. All the elements in all the orbits $D_n \cdot \{|\uparrow\rangle, |\downarrow\rangle\}^{\otimes n}$ together form a complete basis in the Hilbert space $\mathcal{H}(\mathbb{C}^{2^n})$. As such, it is sufficient to show that the operators act on the elements in each orbit the same number of times as the number of elements in that orbit.

The character tables in Tables 3.3 and 3.4 list the number of irreps. I first discuss the situation that the orbit $D_n \cdot |s_1, \ldots, s_n\rangle$ has n elements and $C_n \cdot |s_1, \ldots, s_n\rangle = (D_n \backslash C_n) \cdot |s_1, \ldots, s_n\rangle$. If n is odd, the $n-1$ operators generated by the $\frac{n-1}{2}$ 2-dimensional irreps each act on one element in the orbit once. O^{Id} also acts on the orbit element once. In total, n operators act on the orbit elements.

Otherwise, if n is even, the $n-2$ operators generated by the $\frac{n-2}{2}$ 2-dimensional irreps each act on one element in the orbit once. O^{Id} also acts on the orbit element once. In addition, one of $O^{D_{\frac{n}{2}}}$ and $O^{D'_{\frac{n}{2}}}$ acts on the orbit element once. In total, n operators act on the orbit elements.

I then discuss the situation that the orbit $D_n \cdot |s_1, \ldots, s_n\rangle$ has $2n$ elements and $C_n \cdot |s_1, \ldots, s_n\rangle \cap (D_n \backslash C_n) \cdot |s_1, \ldots, s_n\rangle = \varnothing$. If n is odd, the $n-1$ operators generated by the $\frac{n-1}{2}$ of 2-dimensional irreps each act on two elements in the orbit once. O^{Id} and O^{C_n} each acts on one orbit element once. In total, there are $2n$ actions on the orbit elements.

Otherwise, if n is even, the $n-2$ operators generated by the $\frac{n-2}{2}$ of 2-dimensional irreps each act on two elements in the orbit once. O^{Id} and O^{C_n} each acts on one orbit

element once. In addition, both $O^{D_{\frac{n}{2}}}$ and $O^{D'_{\frac{n}{2}}}$ act on one orbit element once. In total, there are $2n$ actions on the orbit elements.

Now I discuss the situation where $D_n \cdot |s_1, \ldots, s_n\rangle$ has fewer than n elements and $C_n \cdot |s_1, \ldots, s_n\rangle = (D_n \backslash C_n) \cdot |s_1, \ldots, s_n\rangle$. Let the number of elements in $D_n \cdot |s_1, \ldots, s_n\rangle$ be d, which must be a factor of n. In order for an operator $O_1^{\theta_j}$ or $O_2^{\theta_j}$ from a 2-dimensional irrep to act on one element in the orbit and generate a nonzero basis vector, d must be a multiple of the number of elements in $\{\exp(ik\theta_j) | 0 \leq k \leq n-1, \theta_j = \frac{2\pi j}{n}\}$. This requires θ_j to be a multiple of $\frac{2\pi}{d}$, or equivalently, j must be a multiple of $\frac{n}{d}$. If n is odd, there are $\frac{d-1}{2}$ of such j satisfying $1 \leq j \leq \frac{n-1}{2}$; i.e., $\theta_j = \frac{2\pi}{d}, \frac{4\pi}{d}, \ldots, \frac{\pi(d-1)}{d}$; then $d-1$ operators generated by the corresponding $\frac{d-1}{2}$ of 2-dimensional irreps each act on one element in the orbit once. O^{Id} also acts on the orbit element once. In total, d operators act on the orbit elements.

Otherwise, if n is even, I need to discuss the two situations where d is odd and d is even. When d is odd, there are $\frac{d-1}{2}$ multiples of $\frac{n}{d}$ satisfying $1 \leq j \leq \frac{n-2}{2}$ (i.e., $\theta_j = \frac{2\pi}{d}, \frac{4\pi}{d}, \ldots, \frac{\pi(d-1)}{d}$). Then $d-1$ operators generated by the corresponding $\frac{d-1}{2}$ of 2-dimensional irreps each act on one element in the orbit once. O^{Id} also acts on the orbit element once. In total, d operators act on the orbit elements. When d is even, there are $\frac{d-2}{2}$ multiples of $\frac{n}{d}$ satisfying $1 \leq j \leq \frac{n-2}{2}$ (i.e., $\theta_j = \frac{2\pi}{d}, \frac{4\pi}{d}, \ldots, \frac{\pi(d-2)}{d}$). Then $d-2$ operators generated by the corresponding $\frac{d-2}{2}$ 2-dimensional irreps each act on one element in the orbit once. O^{Id} and one of $O^{D_{\frac{n}{2}}}$ and $O^{D'_{\frac{n}{2}}}$ also each act on the orbit element once. In total, d operators act on the orbit elements.

Lastly, I discuss the situation where $D_n \cdot |s_1, \ldots, s_n\rangle$ has fewer than $2n$ elements, and $C_n \cdot |s_1, \ldots, s_n\rangle \cap (D_n \backslash C_n) \cdot |s_1, \ldots, s_n\rangle = \varnothing$. This situation is very similar to the situation

where $D_n \cdot |s_1, \ldots, s_n\rangle$ has $2n$ elements. In this case, O^{C_n} makes one additional action to O^{Id}, and both $O^{D_{\frac{n}{2}}}$ and $O^{D'_{\frac{n}{2}}}$ make actions if it applies, and each operator generated by the 2-dimensional irreps acts twice if it applies. As a result, the number of actions on the orbit elements is doubled compared with the previous situation.

I have shown that the number of actions on the elements in each orbit is the same as the number of elements in that orbit. These actions generate orthogonal basis vectors, which I have proved. Since all the orbits $D_n \cdot \{|\uparrow\rangle, |\downarrow\rangle\}^{\otimes n}$ together form a complete basis in the Hilbert space $\mathcal{H}(\mathbb{C}^{2^n})$, the basis vectors generated by acting the operators on the orbit elements must also form a complete basis in the Hilbert space $\mathcal{H}(\mathbb{C}^{2^n})$.

Q.E.D.

The irreps constructed in Eq. 3.17 differ from those constructed in Eq. 3.25; however, they can be transformed into each other with linear unitary transformations. My conclusion then holds that the basis vectors generated in the procedure of Sec. 3.3 are orthogonal and complete in the Hilbert space $\mathcal{H}(\mathbb{C}^{2^n})$.

It is worth noting that the Schur orthogonality plays an essential role in the proof. Therefore, I claim that the Schur orthogonality and completeness of the irreps of finite groups is the origin of the orthogonality and completeness of the basis vectors generated in the procedure in Sec. 3.3. I further conjecture that for any subgroup G of S_n, a similar procedure of acting the operators defined with the group algebra $\mathcal{R}_G$ on the elements in the orbits $\{G \cdot |s_1, \ldots, s_n\rangle \mid |s_1, \ldots, s_n\rangle \in \{|\uparrow\rangle, |\downarrow\rangle\}^{\otimes n}\}$ will generate an orthogonal and complete basis in the Hilbert space $\mathcal{H}(\mathbb{C}^{2^n})$, and the Schur orthogonality and completeness of the irreps of finite groups will play an essential role in the proof.

3.5 Generalizing the Symmetry-Based Method With the Lie-Trotter-Suzuki Decomposition

In Secs. 3.1, 3.2, 3.3, 3.4, I discussed how to decompose the Hilbert space $\mathcal{H}(\mathbb{C}^{2^n})$ of an n-qubit system and transform the Hamiltonians when the system has S_n or D_n symmetry. In general, the symmetry of the entire system may be low. For example, consider the following control Hamiltonian,

$$H_c'(t) = \frac{1}{2}\sum_{i=1}^{n}\left(B_x^{(i)}(t)\cdot\sigma_x^{(i)} + B_y^{(i)}(t)\cdot\sigma_y^{(i)}\right). \tag{3.28}$$

The S_n symmetry of the n-qubit system is broken since each qubit is tuned by a different control pulse. Therefore, this Hamiltonian cannot be block diagonalized with the A_S-transformation. However, each term in the sum, i.e., $H_c'^{(i)}(t) = B_x^{(i)}(t)\cdot\sigma_x^{(i)} + B_y^{(i)}(t)\cdot\sigma_y^{(i)}$ satisfies S_1 symmetry. When the static Hamiltonian has no coupling terms as in Eq. 2.3, I can calculate the evolution of each qubit separately in the Hilbert space $\mathcal{H}(\mathbb{C}^2)$. As such, the Hilbert space is decomposed from $\mathcal{H}(\mathbb{C}^{2^n})$ to $\mathcal{H}(\mathbb{C}^2)^{\otimes n}$, simplifying the QOC computation.

The following example is more complicated. When the n-qubit system has coupling terms as in Eq. 2.4, the complete Hamiltonian becomes

$$H_0 + H_c'(t) = \frac{1}{2}\sum_{i=1}^{n}\left(B_z\cdot\sigma_z^{(i)} + B_x^{(i)}(t)\cdot\sigma_x^{(i)} + B_y^{(i)}(t)\cdot\sigma_y^{(i)}\right) + c_{\text{cpl}}\cdot\frac{1}{4}\sum_{i=1}^{n}\sigma_z^{(i)}\sigma_z^{(i+1)}. \tag{3.29}$$

This system is inseparable, and therefore, the QOC computation cannot be simplified with the tensor product decomposition of the Hilbert space. However, each term in the Hamilto-

nian preserves some reduced symmetry. Specifically, the ith qubit terms have S_1 symmetry, and all the coupling terms together have D_n symmetry. Then I am allowed to generalize my symmetry-based method with the Lie-Trotter-Suzuki decomposition, or Trotterization, of the propagators.

Trotterization is a decomposition that approximates the exponential of a summed-up operator with the product of the exponential of each element in the sum. [35, 36] For the system described by Eq. 3.29, defining $H_0^{(i)} = B_z \cdot \frac{1}{2}\sigma_z^{(i)}$ and $H_{\text{cpl}} = c_{\text{cpl}} \cdot \frac{1}{4}\sum_{i=1}^{n} \sigma_z^{(i)}\sigma_z^{(i+1)}$, the discretized propagator at the jth time step as defined in Eq. 2.7 can be written as

$$U_j = \exp\left(-i\tau \sum_{i=1}^{n}\left(H_0^{(i)} + H_c'^{(i)}[(j+\frac{1}{2})\tau] + \frac{1}{n}H_{\text{cpl}}\right)\right). \tag{3.30}$$

Then I Trotterize Eq. 3.30 by the symmetry of the terms as

$$U_j = \prod_{i=1}^{n}\left[\exp\left(-i\tau\left(H_0^{(i)} + H_c'^{(i)}[(j+\frac{1}{2})\tau]\right)\right)\exp\left(-i\frac{\tau}{n}H_{\text{cpl}}\right)\right] + O(n^2\tau^2), \tag{3.31}$$

where the first and second exponentials in the bracket have S_1 and D_n symmetries, respectively. I transform each exponential term so that the number of blocks is maximized and the size of each time-dependent block is minimized. The transformation is given by

$$U_j \approx \prod_{i=1}^{n}\left[A_i \exp\left(-i\tau A_i^\dagger\left(H_0^{(i)} + H_c'^{(i)}[(j+\frac{1}{2})\tau]\right)A_i\right)A_i^\dagger A_D \exp\left(-i\frac{\tau}{n}A_D^\dagger H_{\text{cpl}} A_D\right)A_D^\dagger\right], \tag{3.32}$$

where $A_i = A_{(i,n)}$ is the permutation matrix that swaps the ith and the nth qubit. Either $H_0^{(i)}$ or $H_c'^{(i)}[(j+\frac{1}{2})\tau]$ is proportional to $\sigma_\alpha^{(i)}, \alpha = x, y, z$, so I discuss the transformation of

$\sigma_\alpha^{(i)}$ here. After transformation, $A_{(i,n)}^\dagger \sigma_\alpha^{(i)} A_{(i,n)}$ is equal to $\sigma_\alpha^{(n)}$ which has 2^{n-1} size-2-by-2 blocks that are exactly the same. The matrices A_i and $A_D \exp(-i\frac{\tau}{n} A_D^\dagger H_{\text{cpl}} A_D) A_D^\dagger$ are constant and only need to be calculated one time. As such, I reduce the time-dependent term from one size-2^n-by-2^n matrix to n size-2-by-2 matrices.

I present several examples to further illustrate the method above. The coupling terms in the form of $\sigma_\alpha^{(i)}\sigma_\alpha^{(j)}, i \neq j$ can be transformed with $A_{(i,n-1)}A_{(j,n)}$. The transformed term $A_{(j,n)}^\dagger A_{(i,n-1)}^\dagger \sigma_\alpha^{(i)}\sigma_\alpha^{(j)} A_{(i,n-1)}A_{(j,n)}$ is equal to $\sigma_\alpha^{(n-1)}\sigma_\alpha^{(n)}$ and has 2^{n-2} blocks, with each block having a size of 4×4. This term can be further block diagonalized with its S_2 symmetry. More specifically, letting $A = A_{(i,n-1)}A_{(j,n)}(\mathbb{I}_{2^{n-2}} \otimes A_{S_2})$, each 4×4 block in $A_{(j,n)}^\dagger A_{(i,n-1)}^\dagger \sigma_\alpha^{(i)}\sigma_\alpha^{(j)} A_{(i,n-1)}A_{(j,n)}$ can be transformed into one 1×1 and one 3×3 block. Similarly, the terms in the form of $\sigma_\alpha^{\otimes i-1} \otimes \sigma_\beta \otimes \sigma_\alpha^{\otimes j-i-1} \otimes \sigma_\beta \otimes \sigma_\alpha^{\otimes n-j}$ can be transformed with index permutation and $S_2 \otimes S_{n-2}$ symmetry. In general, $\mathbb{I}_2, \sigma_x, \sigma_y, \sigma_z$ and their tensor products form the orthogonal basis of any $2^n \times 2^n$ Hermitian matrix under the Hilbert-Schmidt inner product [64]. Accordingly, the Hamiltonian of an n-qubit system can always be decomposed so that each component can be transformed into $\mathbb{I}_2^{\otimes l} \otimes \sigma_x^{\otimes m} \otimes \sigma_y^{\otimes p} \otimes \sigma_z^{\otimes q}, l + m + p + q = n$ by an adjoint matrix A_I permuting the indices. I can then transform this term with the adjoint matrix $A_G = \mathbb{I}_{2^l} \otimes A_{S_m} \otimes A_{S_p} \otimes A_{S_q}$ where $G = S_m \otimes S_p \otimes S_q$ is the finite group indicating the symmetry of this term.

Based on the examples above, I provide a general framework for parallel computing with the Lie-Trotter-Suzuki decomposition and the symmetry-based transformation of the Hamiltonian of any multi-qubit system. The propagator of the quantum system is Trotterized so that terms sharing the same symmetry of finite groups are put together

and block diagonalized by the same adjoint matrix. The principle of block diagonalizing each exponential term is to maximize the number of blocks and minimize the size of each time-dependent block. Specifically, a general Hamiltonian H can be decomposed into a sum $H = \sum_{G,I}[H_0^{(G,I)} + H_c^{(G,I)}]$ by the symmetry characterized by the finite group G and the indices of the qubits I (I denotes the indices of the qubits coupled to either static fields or controlling pulses simultaneously). The propagator of $H_0^{(G,I)} + H_c^{(G,I)}$ can be transformed by the adjoint matrix $A_{G,I} = A_I A_G$. As such, a general symmetry-based transformed and Trotterized propagator at $t = (j + \frac{1}{2})\tau$ can be written as

$$\begin{aligned} U_j &= \prod_{G,I} \left[\exp\left(-i\tau \left(H_0^{(G,I)} + H_c^{(G,I)}[(j+\frac{1}{2})\tau] \right) \right) + O(\tau^2) \right] \\ &\approx \prod_{G,I} \left[A_{G,I} \exp\left(-i\tau A_{G,I}^\dagger \left(H_0^{(G,I)} + H_c^{(G,I)}[(j+\frac{1}{2})\tau] \right) A_{G,I} \right) A_{G,I}^\dagger \right]. \end{aligned} \tag{3.33}$$

When $A_G = \mathbb{I}_{2^l} \otimes A_{G_{n-l}}$ satisfies $l \geq 1$, the blocks repeat themselves 2^l times in the transformed Hamiltonian, allowing me to calculate the exponential of a $2^{n-l} \times 2^{n-l}$ matrix rather than that of a full $2^n \times 2^n$ matrix when computing the propagator. It is worth noting that each exponential in the Trotterized propagator in Eq. 3.33 is independent of the others, which allows them to be trivially computed in parallel. Also, the exponential of each block (not counting the repetitive blocks) is independent, allowing me to parallelize the computation further.

All of the $A_{G,I}$ adjoint matrices and the blocks in all of the exponentials are unitary, allowing me to easily calculate the inverse of the transformed propagators in parallel. Also, the derivative of each exponential $\exp(-i\tau A_{G,I}^\dagger (H_0^{(G,I)} + H_c^{(G,I)}[(j+\frac{1}{2})\tau]) A_{G,I})$ with respect

to the time-dependent control $B_\alpha[(j+\frac{1}{2})\tau]$ can be approximated as

$$\begin{aligned}
&\frac{\mathrm{d}\left(\exp\left(-i\tau A_{G,I}^{\dagger}\left(H_0^{(G,I)}+H_c^{(G,I)}[(j+\frac{1}{2})\tau]\right)A_{G,I}\right)\right)}{\mathrm{d}(B_\alpha[(j+\frac{1}{2})\tau])} \\
\approx &-i\tau A_{G,I}^{\dagger}\tilde{H}_c^{(G,I)}A_{G,I}\cdot\exp\left(-i\tau A_{G,I}^{\dagger}\left(H_0^{(G,I)}+H_c^{(G,I)}[(j+\frac{1}{2})\tau]\right)A_{G,I}\right)
\end{aligned} \tag{3.34}$$

when τ is small and the control Hamiltonian has the simple expression of $H_c^{(G,I)}[(j+\frac{1}{2})\tau] = B_\alpha[(j+\frac{1}{2})\tau]\cdot\tilde{H}_c^{(G,I)}$, which is a common situation. As such, I can easily apply the transformed propagator U_j in Eq. 3.33 to gradient-based methods with backpropagation. [51, 55]

3.6 Source Code Availability

The Python code used for the QOC of multi-qubit systems and the symmetry-based methods is available at https://github.com/xwang056/qoc_multi-qubits.

Chapter 4

Results and Analysis

In Sec. 4.1, I present the sparsity plots of several example Hamiltonians. A comparison of the dimensions of $\mathcal{H}(\mathbb{C}^{2^n})$, $\mathcal{H}_1^{[n]}$, and $\mathcal{H}_1^{\mathrm{Id}}$ for $3 \leq n \leq 14$ is provided. Comparisons of the optimal controlling pulses and the power spectra generated by the conventional method and the symmetry-based method are presented in Sec. 4.2. In addition, I present a comparison of the execution time of these two approaches. These comparisons lead to the conclusion that the symmetry-based method reduces the execution time by orders of magnitude and generates the same optimal controlling pulses. Comparisons between the conventional method and the symmetry-based method combined with the Lie-Trotter-Suzuki decomposition are provided in Sec. 4.3.

Some content in this chapter is part of *Accelerating Quantum Optimal Control of Multi-Qubit Systems with Symmetry-Based Hamiltonian Transformations*, an article accepted for publication in *AVS Quantum Science*.

4.1 Decomposition of the Hilbert Space and Transformation of the Hamiltonians

In Figs. 4.1, 4.2, 4.3, 4.4, and 4.5, I present the sparsity plots of the original and the transformed Hamiltonians of 3-, 4-, 5-, 6-, and 7-qubit systems, respectively. The transformed Hamiltonians $A_S^\dagger H_x A_S$ and $A_D^\dagger H_x A_D$ are block diagonal, while the original Hamiltonian H_x is not. $A_S^\dagger H_z A_S$ and $A_D^\dagger H_z A_D$ remain diagonal after transformation, and they follow the same subspace decomposition with $A_S^\dagger H_x A_S$ and $A_D^\dagger H_x A_D$, respectively. The distribution of the nonzero elements in the complex-valued H_y matrix is the same as those in H_x. In systems of 4 qubits and above, $H_{z,\text{cpl}}$ can be transformed into a block diagonal matrix by only A_D since it does not have S_n symmetry. However, $A_S^\dagger H_{z,\text{cpl}} A_S$ in the 3-qubit system is block diagonalized because $S_3 = D_3$ and consequently, $A_{S_3} = A_{D_3}$. Note that the dimension of a subspace in the Hilbert space decomposition (the subspaces $\mathcal{H}_j^\lambda$ or $\mathcal{H}_j^\theta$) equals the size of the corresponding square block in the transformed Hamiltonian (the green box from top-left to bottom-right in Figs. 4.1, 4.2, 4.3, 4.4, and 4.5). The first subspace ($\mathcal{H}_1^{[n]}$ or $\mathcal{H}_1^{\text{Id}}$) contains the significant $|\uparrow\rangle^{\otimes n}$ and $|\downarrow\rangle^{\otimes n}$ states of the multi-qubit system. Table 4.1 shows a comparison between the dimension of the complete Hilbert space and the dimension of the first subspace for systems with various numbers of qubits. While the dimension of $\mathcal{H}(\mathbb{C}^{2^n})$ is 2^n, the dimensions of $\mathcal{H}_1^S$ and $\mathcal{H}_1^D$ are reduced to $n+1$ and $\sim O(\frac{2^n}{n})$, respectively.

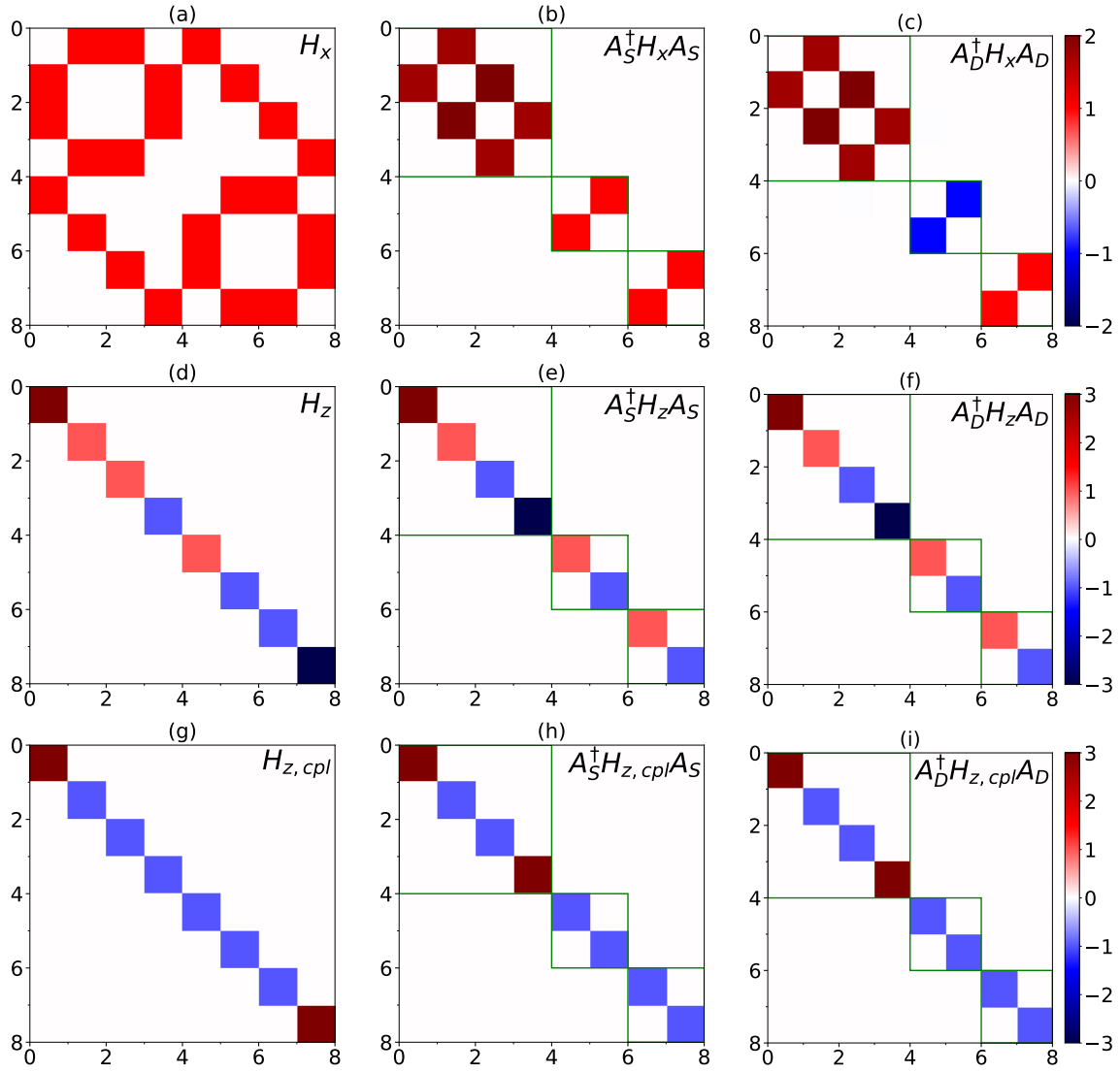

Figure 4.1: **Sparsity plots for Hamiltonians of a 3-qubit system.** (a), H_x; (b), $A_S^\dagger H_x A_S$; (c), $A_D^\dagger H_x A_D$; (d), H_z; (e), $A_S^\dagger H_z A_S$; (f), $A_D^\dagger H_z A_D$; (g), $H_{z,\mathrm{cpl}}$; (h), $A_S^\dagger H_{z,\mathrm{cpl}} A_S$; and (i), $A_D^\dagger H_{z,\mathrm{cpl}} A_D$. The x- and y-axes denote the column and row indices of the matrix elements, respectively. The color bars indicate the value of the matrix elements. Each block for the matrices in panels (b), (c), (e), (f), (h), and (i) is enclosed by a green-colored square box.

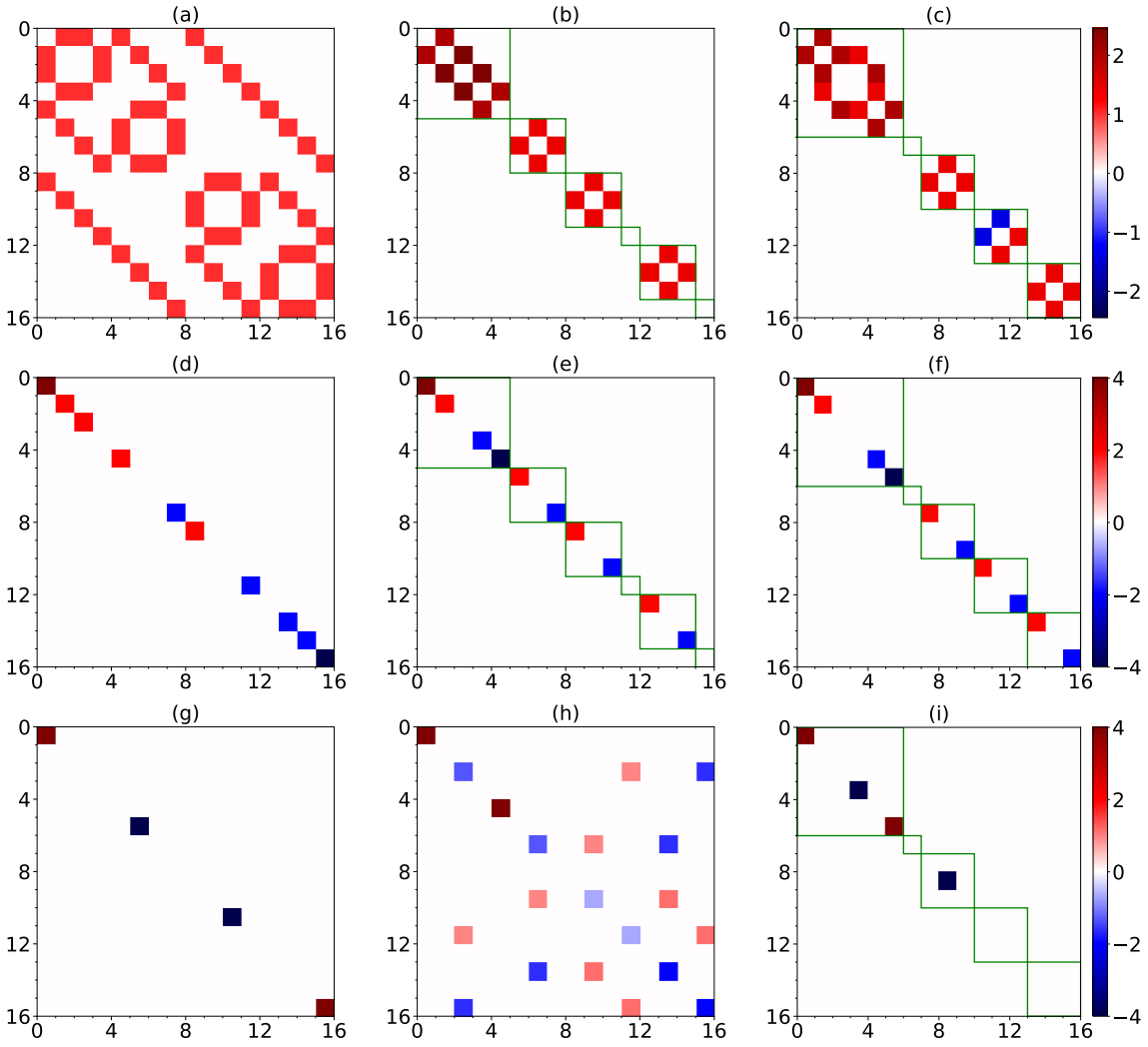

Figure 4.2: **Sparsity plots for Hamiltonians of a 4-qubit system.** (a), H_x; (b), $A_S^\dagger H_x A_S$; (c), $A_D^\dagger H_x A_D$; (d), H_z; (e), $A_S^\dagger H_z A_S$; (f), $A_D^\dagger H_z A_D$; (g), $H_{z,\mathrm{cpl}}$; (h), $A_S^\dagger H_{z,\mathrm{cpl}} A_S$; and (i), $A_D^\dagger H_{z,\mathrm{cpl}} A_D$. The x- and y-axes denote the column and row indices of the matrix elements, respectively. The color bars indicate the value of the matrix elements. Each block for the matrices in panels (b), (c), (e), (f), and (i) is enclosed by a green-colored square box.

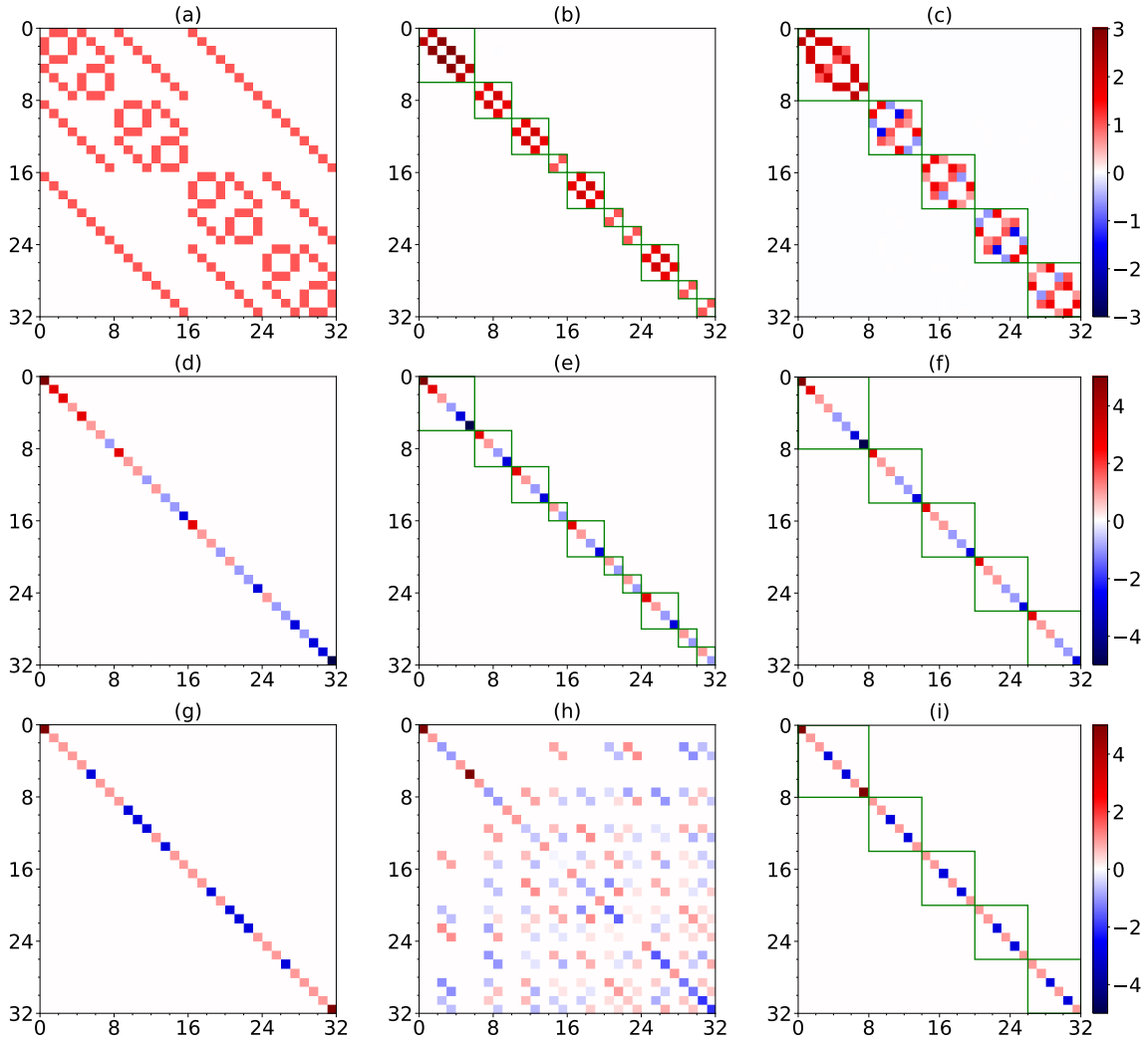

Figure 4.3: **Sparsity plots for Hamiltonians of a 5-qubit system.** (a), H_x; (b), $A_S^\dagger H_x A_S$; (c), $A_D^\dagger H_x A_D$; (d), H_z; (e), $A_S^\dagger H_z A_S$; (f), $A_D^\dagger H_z A_D$; (g), $H_{z,\mathrm{cpl}}$; (h), $A_S^\dagger H_{z,\mathrm{cpl}} A_S$; and (i), $A_D^\dagger H_{z,\mathrm{cpl}} A_D$. The x- and y-axes denote the column and row indices of the matrix elements, respectively. The color bars indicate the value of the matrix elements. Each block for the matrices in panels (b), (c), (e), (f), and (i) is enclosed by a green-colored square box.

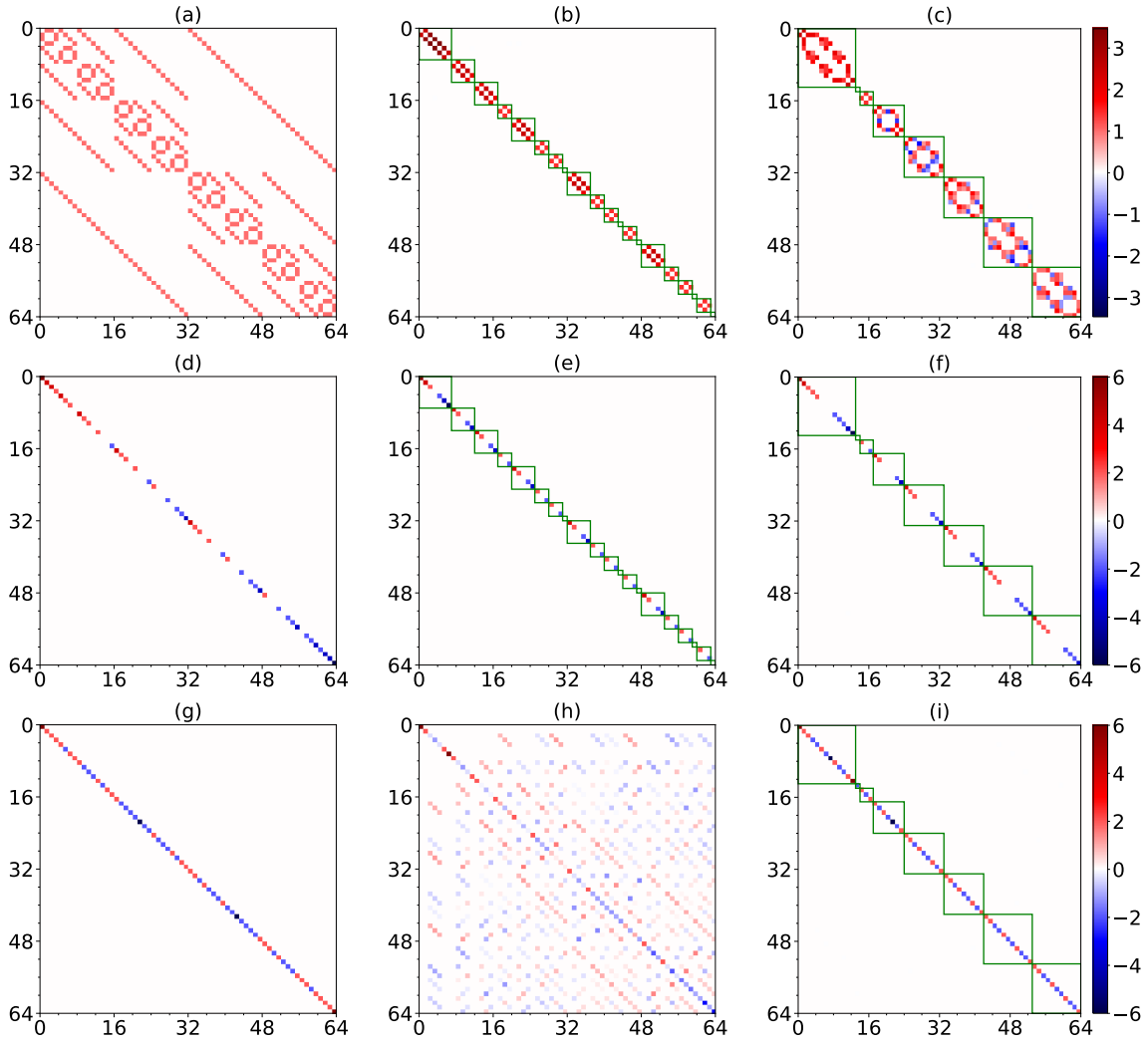

Figure 4.4: **Sparsity plots for Hamiltonians of the 6-qubit system.** (a), H_x; (b), $A_S^\dagger H_x A_S$; (c), $A_D^\dagger H_x A_D$; (d), H_z; (e), $A_S^\dagger H_z A_S$; (f), $A_D^\dagger H_z A_D$; (g), $H_{z,\mathrm{cpl}}$; (h), $A_S^\dagger H_{z,\mathrm{cpl}} A_S$; and (i), $A_D^\dagger H_{z,\mathrm{cpl}} A_D$. The x- and y-axes denote the column and row indices of the matrix elements, respectively. The color bars indicate the value of the matrix elements. Each sub-block for the matrices in panels (b), (c), (e), (f), and (i) is enclosed by a green-colored square.

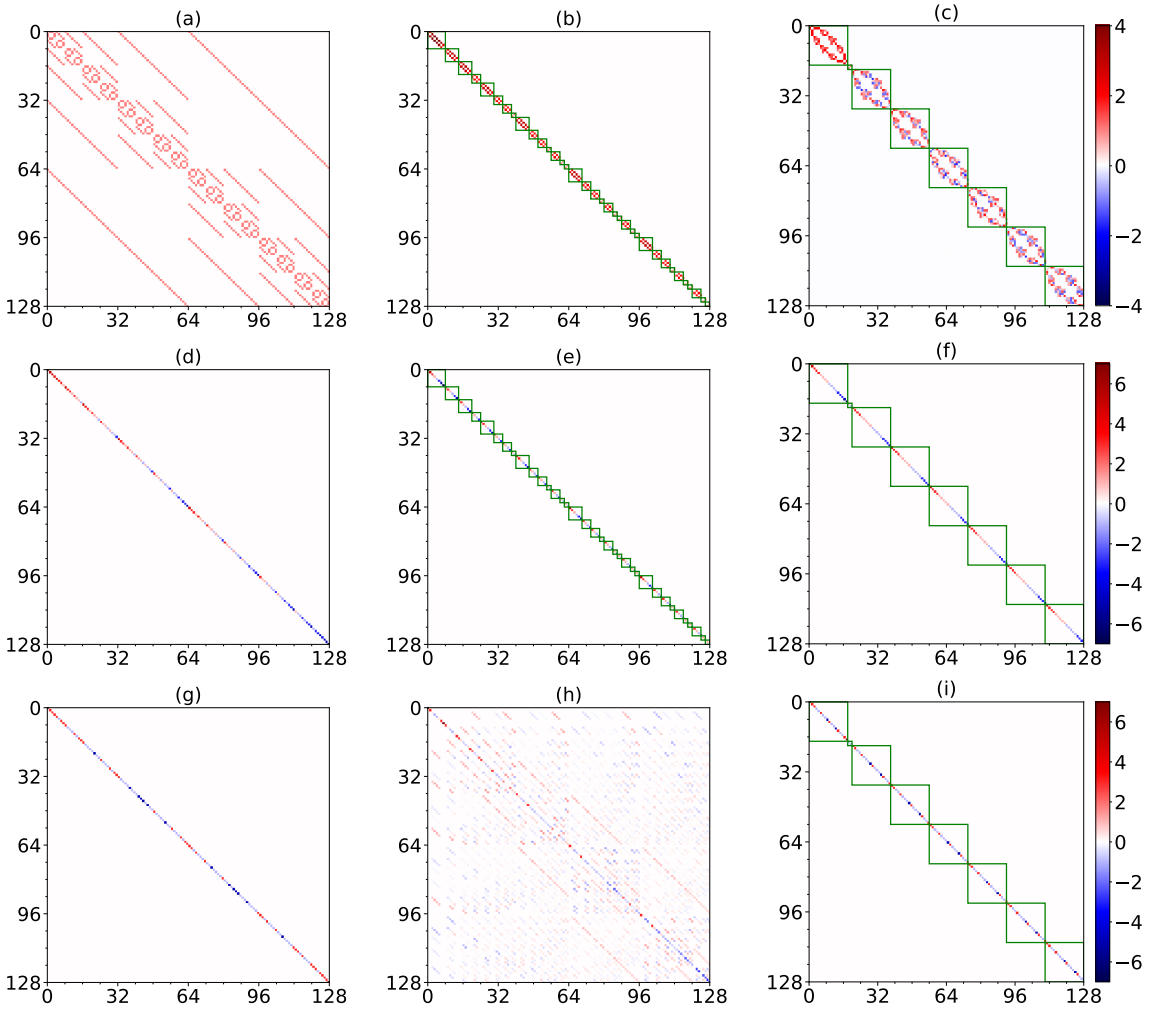

Figure 4.5: **Sparsity plots for Hamiltonians of a 7-qubit system.** (a), H_x; (b), $A_S^\dagger H_x A_S$; (c), $A_D^\dagger H_x A_D$; (d), H_z; (e), $A_S^\dagger H_z A_S$; (f), $A_D^\dagger H_z A_D$; (g), $H_{z,\mathrm{cpl}}$; (h), $A_S^\dagger H_{z,\mathrm{cpl}} A_S$; and (i), $A_D^\dagger H_{z,\mathrm{cpl}} A_D$. The x- and y-axes denote the column and row indices of the matrix elements, respectively. The color bars indicate the value of the matrix elements. Each block for the matrices in panels (b), (c), (e), (f), and (i) is enclosed by a green-colored square box.

Table 4.1: Comparison of the dimensions of $\mathcal{H}(\mathbb{C}^{2^n})$, $\mathcal{H}_1^{[n]}$, and $\mathcal{H}_1^{\mathrm{Id}}$

	Dimension of space		
Number of qubits n	$\mathcal{H}(\mathbb{C}^{2^n})$	$\mathcal{H}_1^{[n]}$	$\mathcal{H}_1^{\mathrm{Id}}$
3	8	4	4
4	16	5	6
5	32	6	8
6	64	7	13
7	128	8	18
8	256	9	30
9	512	10	46
10	1024	11	78
11	2048	12	126
12	4096	13	224
13	8192	14	380
14	16384	15	687

The subspace $\mathcal{H}_1^{[n]}$ is generated with the operator $O_1^{[n]}$ of the identity representation of S_n, whereas the subspace $\mathcal{H}_1^{\mathrm{Id}}$ is generated with the operator O_1^{Id} of the identity representation of D_n. As such, they are listed together and compared to the complete Hilbert space $\mathcal{H}(\mathbb{C}^{2^n})$.

When the Hamiltonians have no coupling terms as in Eqs. 2.3 and 2.5, they are block diagonal after the unitary similarity transformation with A_S. The evolution of the multi-qubit system is strictly confined within each subspace, $\mathcal{H}_j^{\lambda}$. It is common that the initial state is orthogonal to some subspaces. I can then restrict the calculation of the Schrödinger equation (Eq. 2.1) within only necessary subspaces; i.e., instead of using the complete adjoint matrix A_S, I can define such an adjoint matrix A'_S such that its columns consist of only the orthonormal basis of the subspaces in which the initial state $|\psi(0)\rangle$ lies. Then the transformed Hamiltonians $A_S'^{\dagger} H_x A'_S$, $A_S'^{\dagger} H_y A'_S$, and $A_S'^{\dagger} H_z A'_S$ will have fewer blocks and a smaller size, while the calculation is not affected because the orthogonality of the subspaces guarantees that all omitted subspaces will not be transitioned into. Similarly, when the Hamiltonians have coupling terms as in Eq. 2.4, they are block diagonalized with the D_n-induced unitary similarity transformation. The evolution of the multi-qubit system in any subspace $\mathcal{H}_j^{\theta}$ is strictly confined within that subspace regardless of the temporal forms of the control pulses $B_x(t)$ and $B_y(t)$. As such, instead of using the complete adjoint matrix A_D, I can define such an adjoint matrix A'_D such that its columns consist of only the orthonormal basis of the subspaces in which the initial state $|\psi(0)\rangle$ lies. After the similarity transformation, the Hamiltonians in Eqs. 2.4 and 2.5 (i.e., $A_D'^{\dagger} H_0 A'_D$ and $A_D'^{\dagger} H_c A'_D$) will have a smaller size without affecting the calculation results.

4.2 Comparision of Conventional and Symmetry-Based Methods

In this section, I present comparisons of the optimal control pulses, the corresponding power spectra, and the execution time between conventional and symmetry-based methods. As examples, I solve for the temporal forms of the control pulses, $B_x(t)$ and $B_y(t)$, that excite the multi-qubit system from the initial 'all-spin-up' ($|\uparrow\rangle^{\otimes n}$) state to the final 'all-spin-down' ($|\downarrow\rangle^{\otimes n}$) state in the non-coupled and coupled multi-qubit systems, respectively, with conventional and symmetry-based methods. The initial controlling pulses are initialized as white noise with the same seeds so that the results are comparable. The comparison in this section indicates that the symmetry-based methods generate exactly the same results as the conventional method, while the execution time and RAM requirement are reduced by orders of magnitude.

When the multi-qubit system is non-coupled as described by Eqs. 2.3 and 2.5, the multi-qubit system is separable, and the evolution of each qubit is independent of any other qubit. In this case, the Hilbert space can be decomposed into the tensor product of n of 2-dimensional spaces, i.e., $\mathcal{H}(\mathbb{C}^{2^n}) = \bigotimes_{i=1}^{n} \mathcal{H}^{(i)}(\mathbb{C}^2)$, and each space $\mathcal{H}^{(i)}(\mathbb{C}^2)$ can be treated independently. However, in my study, I make use of the direct sum decomposition $\mathcal{H}(\mathbb{C}^{2^n}) = \bigoplus_{\lambda,j} \mathcal{H}_j^{\lambda}$ as it is allowed by the symmetry of the n-qubit system. As the two states $|\uparrow\rangle^{\otimes n}$ and $|\downarrow\rangle^{\otimes n}$ both lie and evolve in the first subspace $\mathcal{H}_1^{[n]}$, only the first block of $A_S^\dagger H_0 A_S$ and $A_S^\dagger H_c A_S$ are necessary and sufficient in the calculations. As shown in Fig. 4.6a, the symmetry-based method reduces the runtime by orders of magnitude due to the decreased size of the Hamiltonian from $2^n \times 2^n$ to $(n+1) \times (n+1)$. It should be noted

that the separable system with S_n symmetry also has D_n symmetry, and I also compare the computational runtime with the first block of the A_D-transformed Hamiltonians. Although it is much more efficient than the original Hamiltonian, the computational runtime is longer than the A_S-transformed Hamiltonian since the dimension of $\mathcal{H}_1^{\mathrm{Id}}$ is larger than $\mathcal{H}_1^{[n]}$ (see Table 4.1 in Sec. 4.1).

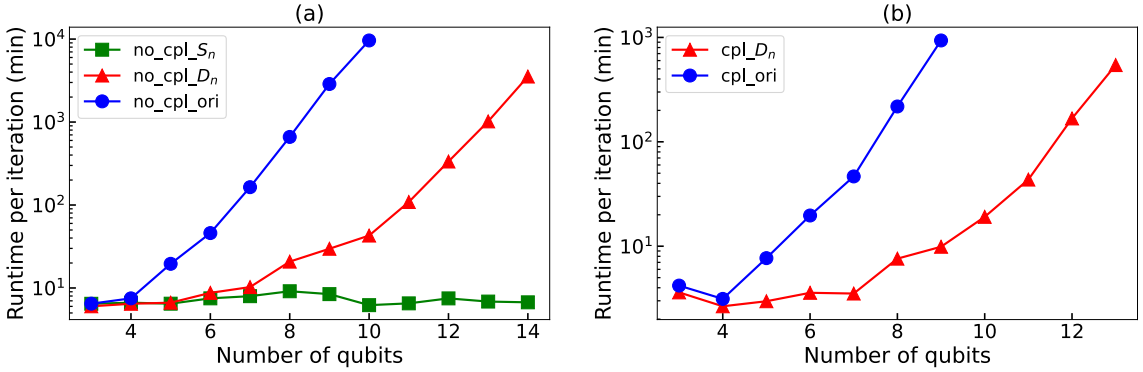

Figure 4.6: **Comparison of computational runtimes between the conventional and symmetry-based methods.** The Hamiltonians have (a) no coupling and (b) nearest-neighbor coupling.

When the Hamiltonians have nearest-neighbor coupling terms as in Eqs. 2.4 and 2.5, the evolution of each qubit is correlated to the other qubits, and the system is no longer separable, and I cannot use the tensor product decomposition. However, the direct sum decomposition $\mathcal{H}(\mathbb{C}^{2^n}) = \bigoplus_{\theta,j} \mathcal{H}_j^\theta$ can still be leveraged to accelerate the calculation, and I can use the first block of $A_D^\dagger H_0 A_D$ and $A_D^\dagger H_c A_D$. Fig. 4.6b shows that compared with the conventional method, the runtime is significantly reduced by the D_n-symmetry-based method as well.

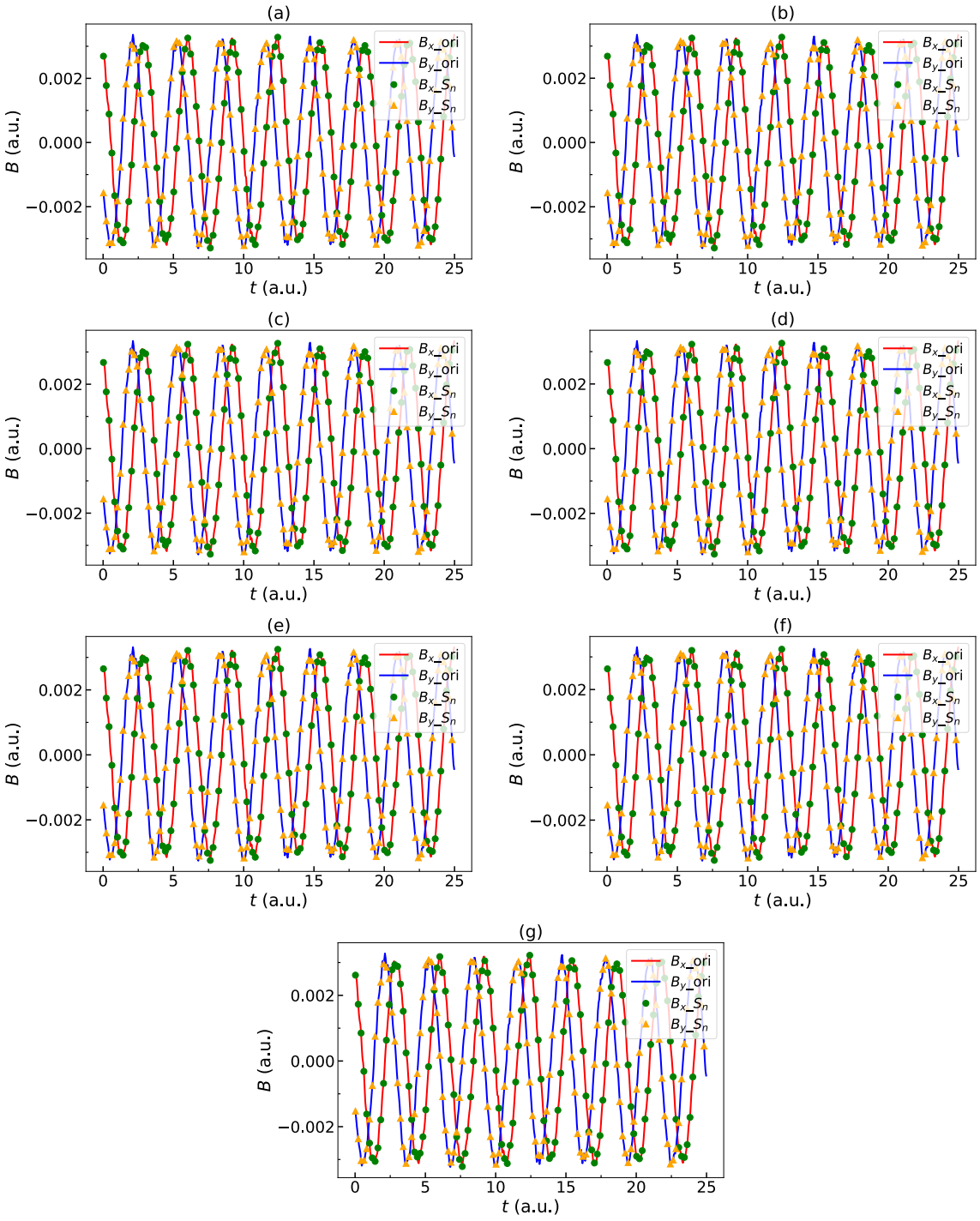

Figure 4.7: **Comparison of optimal control pulses between the conventional and S_n-symmetry-based methods.** The Hamiltonians have no coupling as defined in Eqs. 2.3, 2.5. (a), 3 qubits; (b), 4 qubits; (c), 5 qubits; (d), 6 qubits; (e), 7 qubits; (f), 8 qubits; (g), 9 qubits.

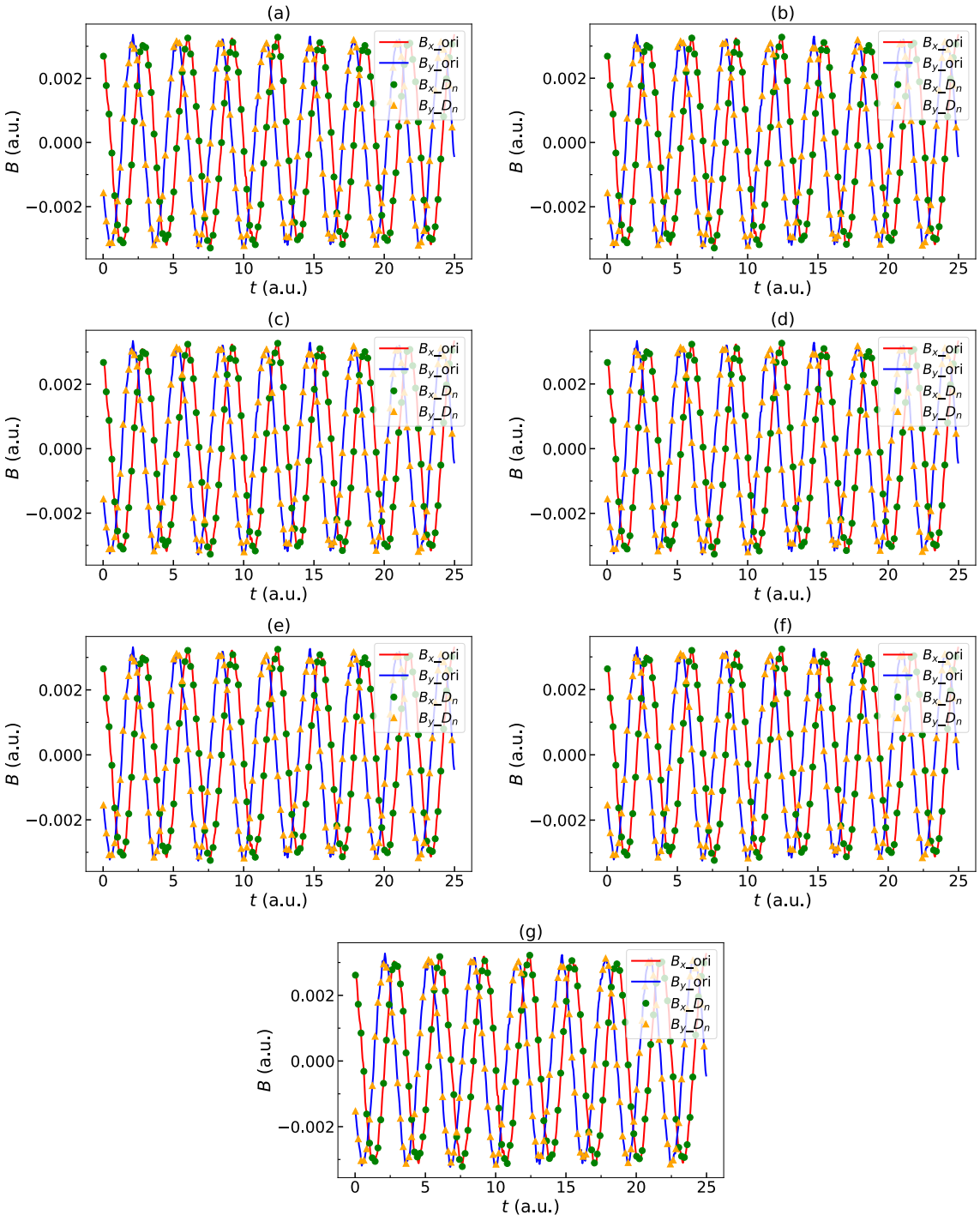

Figure 4.8: **Comparison of optimal control pulses between the conventional and D_n-symmetry-based methods.** The Hamiltonians have no coupling as defined in Eqs. 2.3, 2.5. (a), 3 qubits; (b), 4 qubits; (c), 5 qubits; (d), 6 qubits; (e), 7 qubits; (f), 8 qubits; (g), 9 qubits.

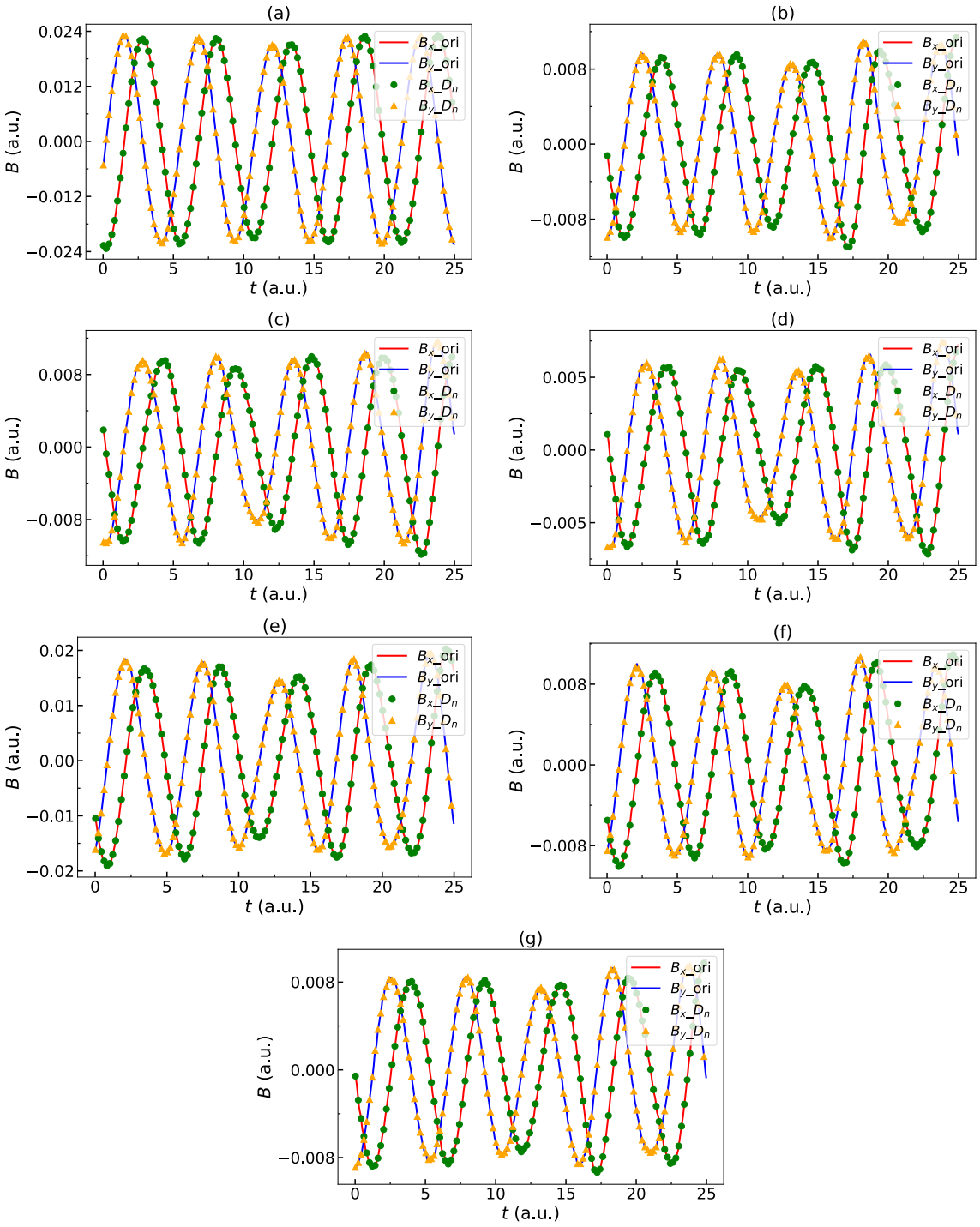

Figure 4.9: **Comparison of optimal control pulses between the conventional and D_n-symmetry-based methods.** The Hamiltonians have nearest-neighbor coupling as defined in Eqs. 2.4, 2.5. (a), 3 qubits; (b), 4 qubits; (c), 5 qubits; (d), 6 qubits; (e), 7 qubits; (f), 8 qubits; (g), 9 qubits.

Since both A_S and A_D are unitary matrices, the unitary transformation of the Hamiltonians with A_S or A_D does not affect the QOC results. To demonstrate this, I carried out numerical tests for systems ranging from 3 to 14 qubits and found the original and transformed Hamiltonians give exactly the same optimal control pulses $B_x(t)$, $B_y(t)$, and power spectra $|\varepsilon_x(\omega)|$, $|\varepsilon_y(\omega)|$. As examples, Figs. 4.7, 4.8, 4.9 compare the optimal control pulses for multi-qubit systems between the conventional and the symmetry-based methods. The data points from the symmetry-based method lie exactly on top of the curves from the conventional method, regardless of whether coupling is present or not. It is worth noting that the optimal $B_x(t)$, $B_y(t)$ for all numbers of qubits in Fig. 4.7 are exactly the same. That is because the multi-qubit system without coupling is separable, i.e., the Hilbert space can be decomposed with the tensor product $\mathcal{H}(\mathbb{C}^{2^n}) = \bigotimes_{i=1}^{n} \mathcal{H}^{(i)}(\mathbb{C}^2)$. As such, the profile of the optimal pulses does not depend on the number of qubits, n.

A comparison of the corresponding power spectra, $|\varepsilon_x(\omega)|$ and $|\varepsilon_y(\omega)|$, is shown in Figs. 4.10 and 4.11. It should be noted that $B_x(t)$ has the same resonance frequency and amplitude as $B_y(t)$. The only difference between $B_x(t)$ and $B_y(t)$ is a $\frac{\pi}{2}$ phase shift, which arises from the circular polarization of the control pulses (see Sec. 5.2). Fig. 4.11 indicates that the nearest-neighbor coupling terms result in three resonance frequencies in the power spectra. This arises from the energy difference of the transitions in the $\mathcal{H}_1^{[n]}$ subspace being degenerate when the system has no coupling, whereas the nearest-neighbor coupling terms partially break the degeneracy of the energy differences in the D_n-induced $\mathcal{H}_1^{\mathrm{Id}}$ subspace.

In Fig. 4.12, I present the comparison of probability vs. iteration between multi-qubit systems with nearest-neighbor coupling and without coupling. When there is no

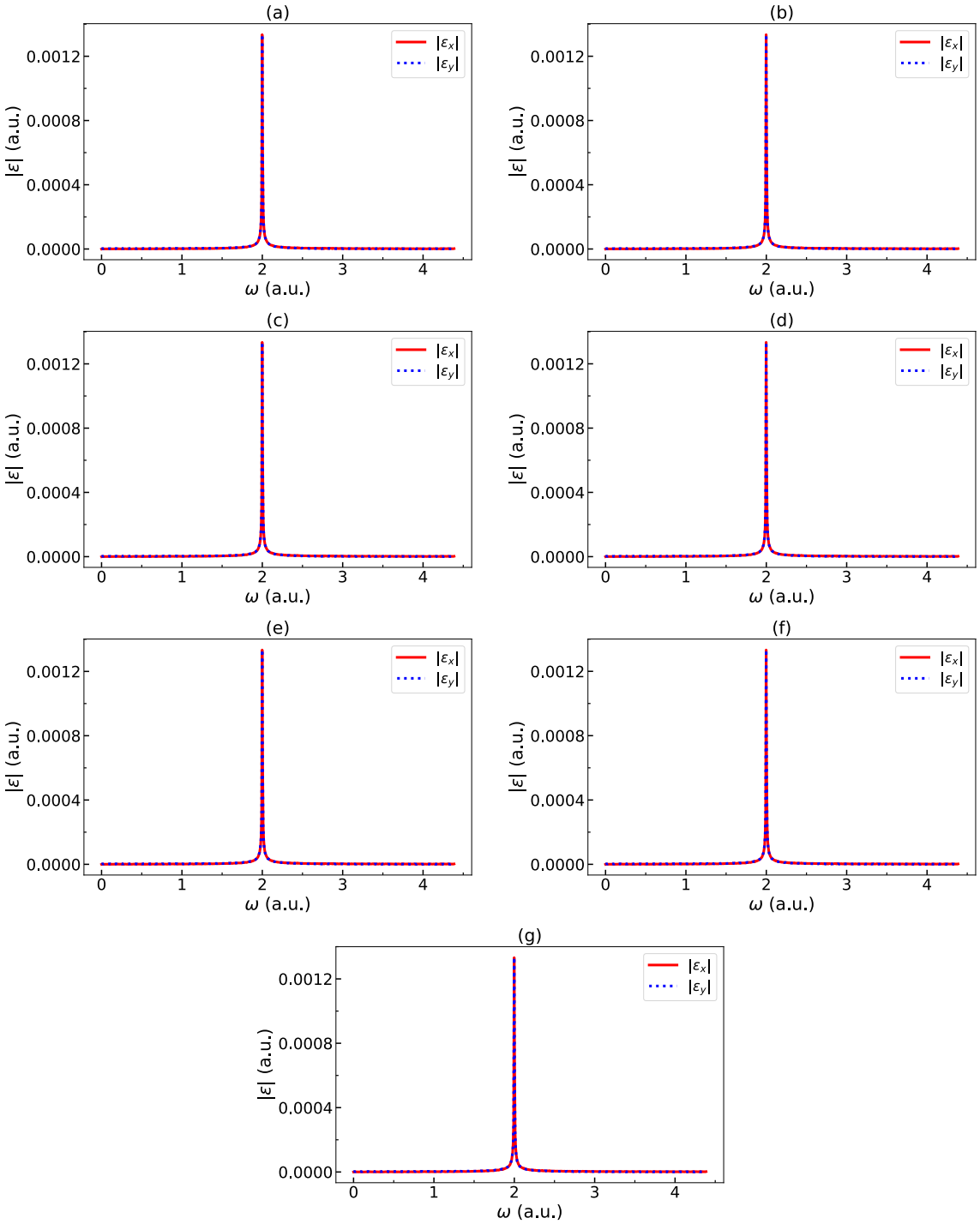

Figure 4.10: **Comparison of power spectra between the x- and y-directions.** The Hamiltonians have no coupling as defined in Eqs. 2.3, 2.5. (a), 3 qubits; (b), 4 qubits; (c), 5 qubits; (d), 6 qubits; (e), 7 qubits; (f), 8 qubits; (g), 9 qubits.

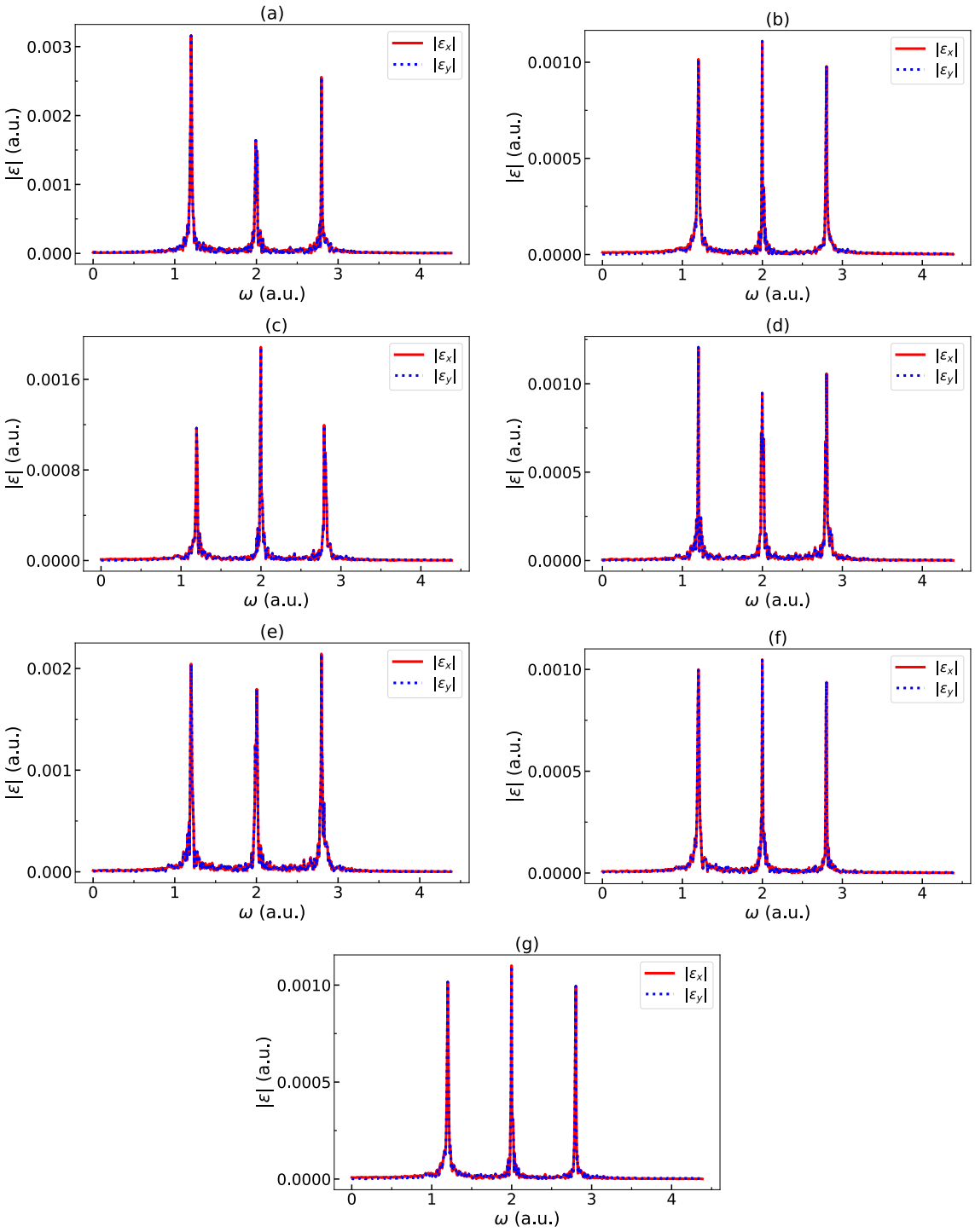

Figure 4.11: **Comparison of power spectra between the x- and y-directions.** The Hamiltonians have nearest-neighbor coupling as defined in Eqs. 2.4, 2.5. (a), 3 qubits; (b), 4 qubits; (c), 5 qubits; (d), 6 qubits; (e), 7 qubits; (f), 8 qubits; (g), 9 qubits.

coupling, the multi-qubit system is separable. The QOC algorithm converges in only one iteration (i.e., $P > 0.999$) no matter what the size of the multi-qubit system is, as shown in Fig. 4.12. Note that the optimal pulses of all non-coupled systems are exactly the same (see Fig. 4.7). Therefore it is trivial that the convergence progress of P does not depend on the number of qubits, n. In contrast, when the nearest-neighbor coupling term exists, the convergence of P becomes more difficult as n increases. Especially, P does not exceed 0.999 in 100 iteration when $n \geq 7$. I discuss how to make P converge in fewer iterations by introducing coupling between further qubits in Sec. 5.1.

4.3 Symmetry-Based Method Combined With the Lie-Trotter-Suzuki Decomposition

In this section, I demonstrate that the accuracy of the Trotterized and transformed propagator in Eq. 3.32 is very close to that of the original propagator in Eq. 3.30. To prove this, I let an n-qubit ($3 \leq n \leq 13$) system evolve for $20,000$ time steps with $\tau = 0.05$ a.u. I then evaluate the fidelity $F = |\frac{\mathrm{Tr}(K_j^{\mathrm{LTS}\dagger} K_j^{\mathrm{ori}})}{2^n}|^2$ [26] of the unitary matrix $K_j^{\mathrm{ori}} = \prod_{m=j}^{1} U_m^{\mathrm{ori}}$ calculated with the original propagator in Eq. 3.30 and the unitary matrix $K_j^{\mathrm{LTS}} = \prod_{m=j}^{1} U_m^{\mathrm{LTS}}$ calculated with the Trotterized propagator in Eq. 3.32. Figs. 4.13 and 4.14 show that in varied multi-qubit systems, the fidelity F is always above 0.996 during the control duration $[0, 1000]$ a.u., which is highly accurate.

I also compared the runtime for calculating the original and transformed propagator per time step. Here I calculated the exponentials in the transformed propagator in

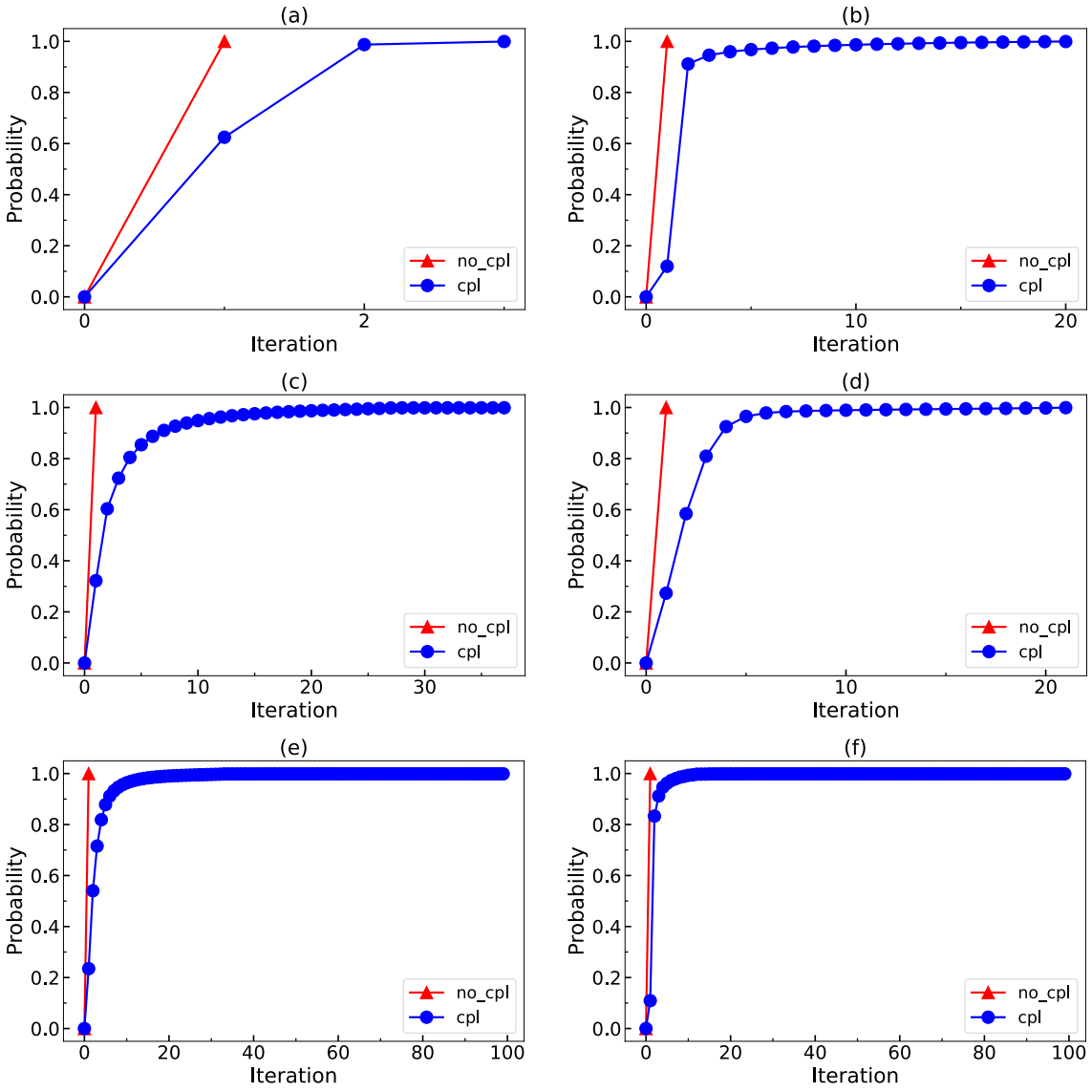

Figure 4.12: **Comparison of convergence between coupled and non-coupled multi-qubit systems.** The Hamiltonians of coupled systems are defined as in Eqs. 2.4 and 2.5. The Hamiltonians of non-coupled systems are defined as in Eqs. 2.3 and 2.5. (a), 3 qubits; (b), 4 qubits; (c), 5 qubits; (d), 6 qubits; (e), 7 qubits; (f), 8 qubits.

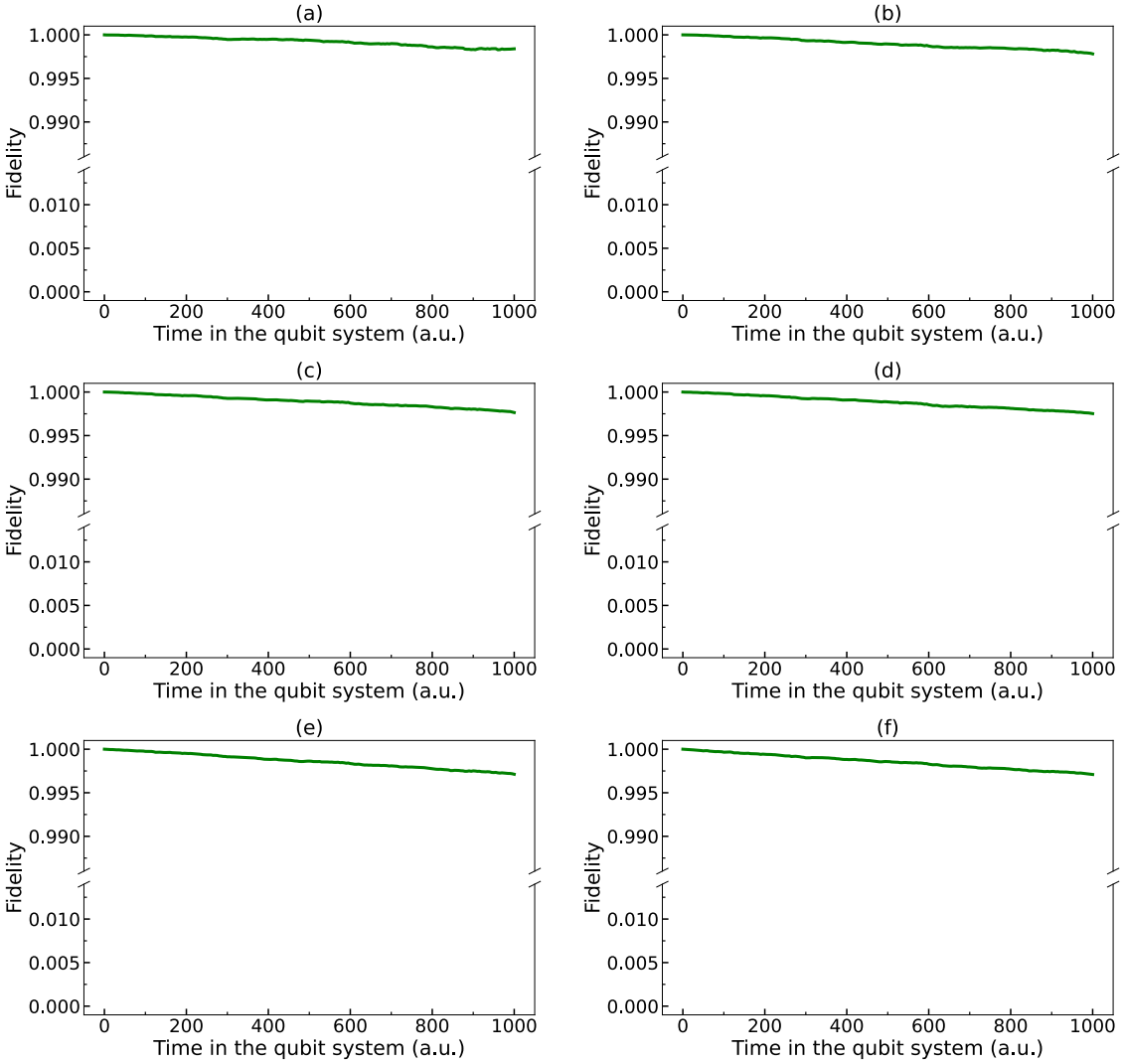

Figure 4.13: **Fidelity of the Trotterized and transformed propagator in multi-qubit systems.** (a) The fidelity vs. control duration in the 3-qubit system; (b) 4 qubits; (c) 5 qubits; (d) 6 qubits; (e) 7 qubits; (f) 8 qubits.

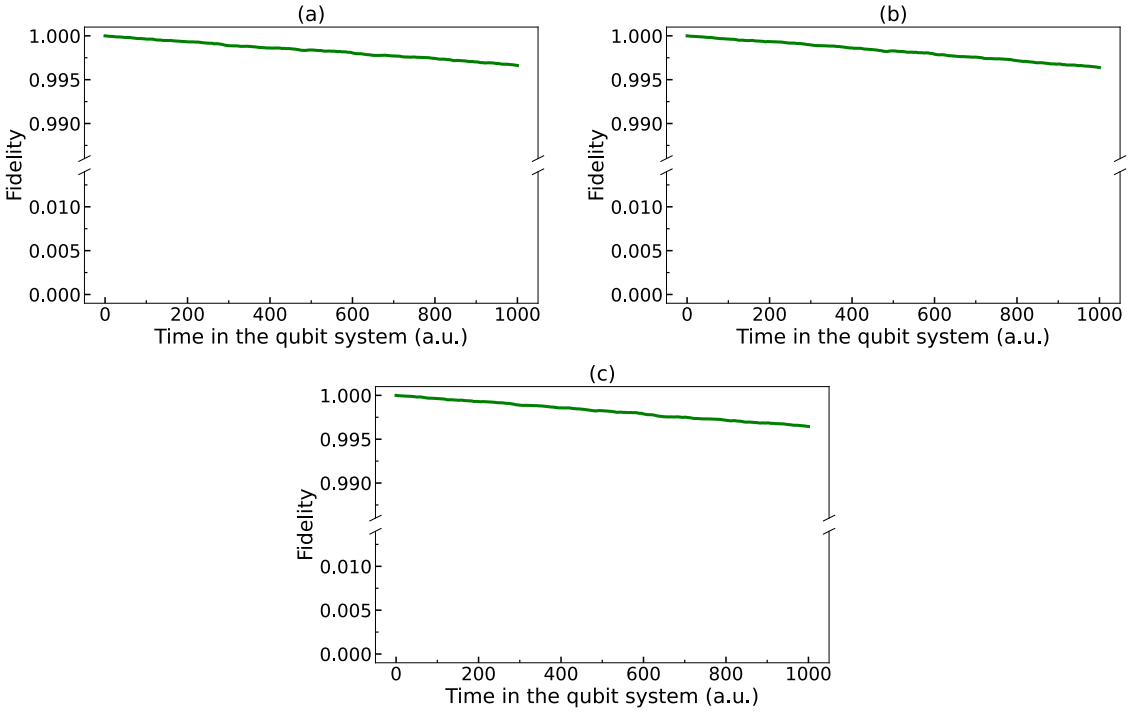

Figure 4.14: **Fidelity of the Trotterized and transformed propagator in multi-qubit systems.** (a) The fidelity vs. control duration in the 9-qubit system; (b) 10 qubits; (c) 11 qubits.

series. To approximate the runtime in an in-parallel computing setup, I divided the runtime for calculating the transformed propagator by n. As Fig. 4.15 shows, the transformed propagator is more time-efficient since each exponential term in Eq. 3.32 is block diagonalized into exactly the same blocks, and I need to calculate the matrix exponential of only one block. Collectively, the tests above show that the transformed propagator in Eq. 3.32 is highly accurate and time-efficient.

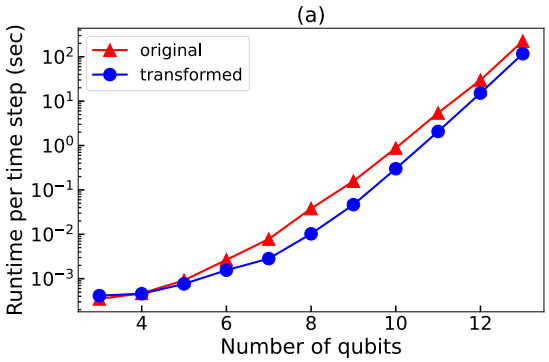

Figure 4.15: **Comparison of computational runtime between the original and the Trotterized and transformed propagator.** The number of qubits n ranges from 3 to 13.

Chapter 5

Discussion

I propose the concept of symmetry-protected subspaces in Sec. 5.1. By introducing the coupling between further qubits without breaking the symmetry of finite groups, I can gain more controllability in each subspace. In addition, I list several potential applications of symmetry-protected subspaces, including preparing permutation-symmetric states [32], realizing simultaneous quantum gate operations [5, 6], quantum error suppression, and quantum simulation of other quantum systems [37, 38]. A point of view based on ladder operators is presented in Sec. 5.2 to help understand the dynamics of multi-qubit systems. The selection rules of the transitions in the multi-qubit system can easily be derived from the ladder-operator-based approach.

Some content in this chapter is part of *Accelerating Quantum Optimal Control of Multi-Qubit Systems with Symmetry-Based Hamiltonian Transformations*, an article accepted for publication in *AVS Quantum Science*.

5.1 Symmetry-Protected Subspaces of the Hilbert Space

I discuss the concept of symmetry-protected subspaces inspired by the finite-group-induced decomposition of the Hilbert space $\mathcal{H}(\mathbb{C}^{2^n})$. The system described by Eqs. 2.3 and 2.5, and Eqs. 2.4 and 2.5 has S_n/D_n symmetry, respectively. Denoting the state of a single qubit as $|\psi\rangle_{\text{sq}}$, all the $|\psi\rangle_{\text{sq}}^{\otimes n}$ states lie in the first subspace $\mathcal{H}_1^{[n]}/\mathcal{H}_1^{\text{Id}}$ of S_n/D_n symmetry. In fact, $\mathcal{H}_1^{[n]}$ is a subspace of $\mathcal{H}_1^{\text{Id}}$. It should be noted that transitions among the $|\psi\rangle_{\text{sq}}^{\otimes n}$ states can be enabled with quantum gates $U_{\text{sq}}^{\otimes n}$, where U_{sq} is a single-qubit gate. As such, all $U_{\text{sq}}^{\otimes n}$ transitions are restricted within the specific subspace; i.e., a state in one subspace cannot transition into another subspace as long as the Hamiltonian preserves the symmetry of finite groups. Therefore, I claim that the subspaces generated by decomposing the Hilbert space $\mathcal{H}(\mathbb{C}^{2^n})$ are protected by the symmetry of the finite groups. Given an initial $|\uparrow\rangle^{\otimes n}$ state, some important multi-qubit states, such as the Greenberger–Horne–Zeilinger (GHZ) state and the W state [32], can be realized in the first subspace $\mathcal{H}_1^S/\mathcal{H}_1^D$. Some essential simultaneous gates in Shor's algorithm for factorizing integers in polylogarithmic time [5] and Grover's algorithm for unstructured search [6], such as $H^{\otimes n}$ (where H denotes the Hadamard gate), can also be realized in $\mathcal{H}_1^S/\mathcal{H}_1^D$.

Physical qubits have been realized in several platforms, such as superconducting qubits [10, 11], trapped ions [14, 15], nitrogen-vacancy centers in diamonds [16, 17], and neutral atoms [18]. Thus far, all types of physical qubits do not possess an ideal fidelity, which hinders the realization of practical quantum computers. A proposed approach to quantum error correction is to encode one logical qubit with multiple physical qubits. [65, 66, 67, 7] In a symmetry-protected n-qubit system, $|\psi\rangle_{\text{sq}}^{\otimes n}$ states are always in the first

subspace regardless of whether the system has S_n symmetry, D_n symmetry, or the symmetry of another subgroup of S_n. Therefore, a natural approach is to encode $|\uparrow\rangle$ and $|\downarrow\rangle$ with $|\uparrow\rangle^{\otimes n}$ and $|\downarrow\rangle^{\otimes n}$, respectively, in the first subspace. I find that the error rate can be greatly reduced not only because the logical qubit is n-fold encoded but also because the first subspace is protected by the symmetry of the finite group. In short, the quantum error is significantly suppressed since the quantum state cannot evolve to other subspaces even if the control pulses deviate from the optimized amplitude, resonance frequency, or duration.

Turning the attention to the first subspace, when the multi-qubit system has S_n symmetry, $n+1$ eigenstates exist in $\mathcal{H}_1^{[n]}$ with equally-spaced energy levels, as shown in Figs. 5.1a, 5.2a, 5.4a. Thus, there is only one resonance frequency, which corresponds to the single peak in Fig. 4.10. It should be noted that a direct transition is not possible from $|\uparrow\rangle^{\otimes n}$ to $|\downarrow\rangle^{\otimes n}$ due to selection rules (see Sec. 5.2). Such a transition can only be realized via a cascade consisting of multiple intermediate eigenstates. Since there is only one resonance frequency in the transition cascade, any pulse exciting one transition in the cascade also enables all other transitions. As a result, given the initial state is $|\uparrow\rangle^{\otimes n}$, the only possible final eigenstate is $|\downarrow\rangle^{\otimes n}$ lying at the other end of the transition cascade, which is realized by the gate $\sigma_x^{\otimes n}$, and vice versa. It is, therefore, not possible to evolve the system to any intermediate eigenstate because such a transition cannot be realized by any gate in the form of $U_{\text{sq}}^{\otimes n}$.

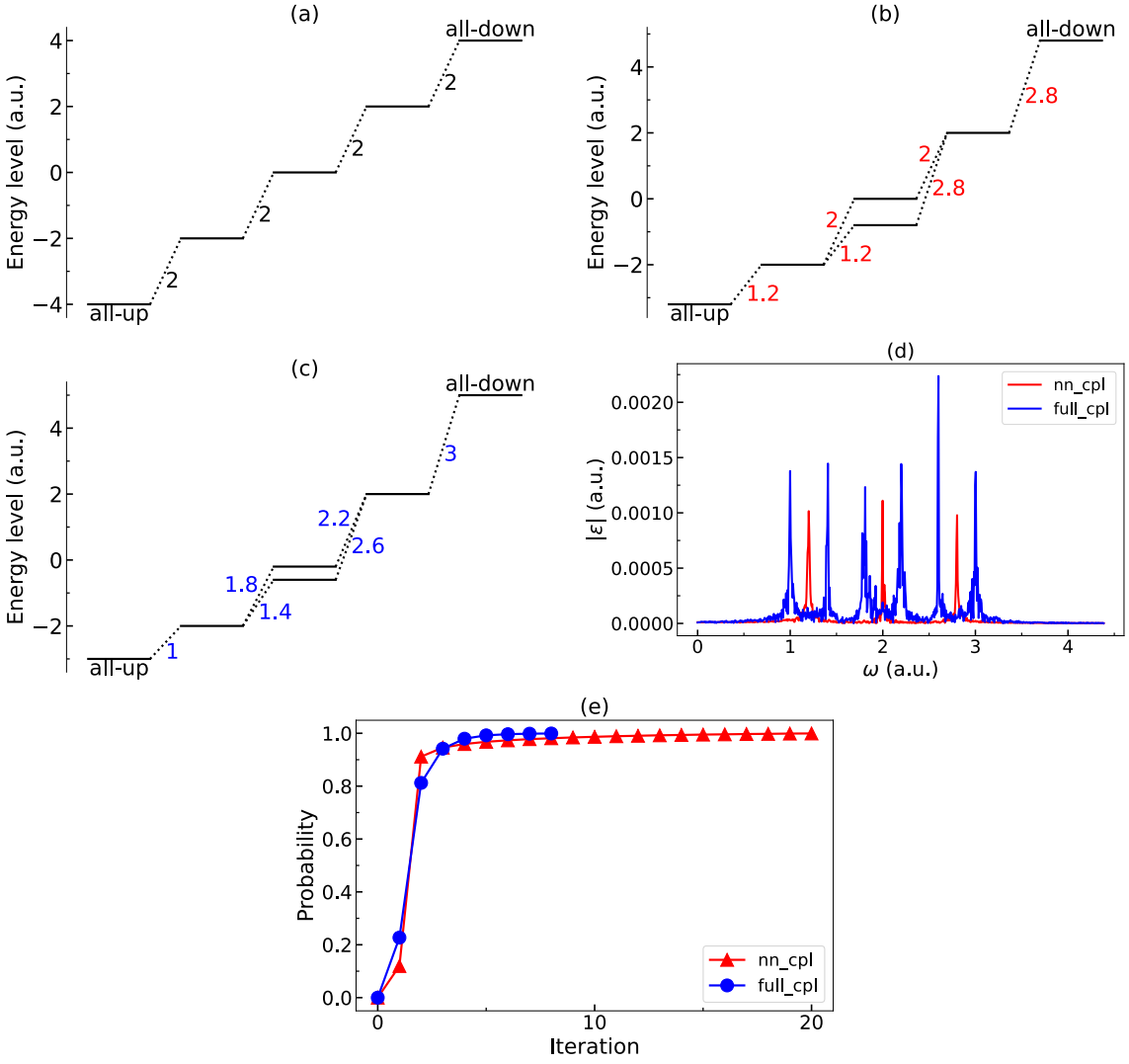

Figure 5.1: **Comparison of energy levels, power spectra, and convergence for the systems with nearest-neighbor coupling and full coupling.** Eigenstates in the first subspace of a 4-qubit system when the system has (a) S_n symmetry without coupling terms, (b) D_n symmetry with nearest-neighbor coupling terms as described in Eq. 2.4, and (c) D_n symmetry with full coupling as described in Eq. 5.1. The 'all-up' and the 'all-down' eigenstates at the two ends of the transition cascade are labeled. The transitions permitted by the selection rules are indicated by dashed lines, and the energy differences are shown next to each transition. (d) Power spectra of the optimized pulses when the 4-qubit system has nearest-neighbor and full coupling. (e) Comparison of convergence for the system with nearest-neighbor and full coupling.

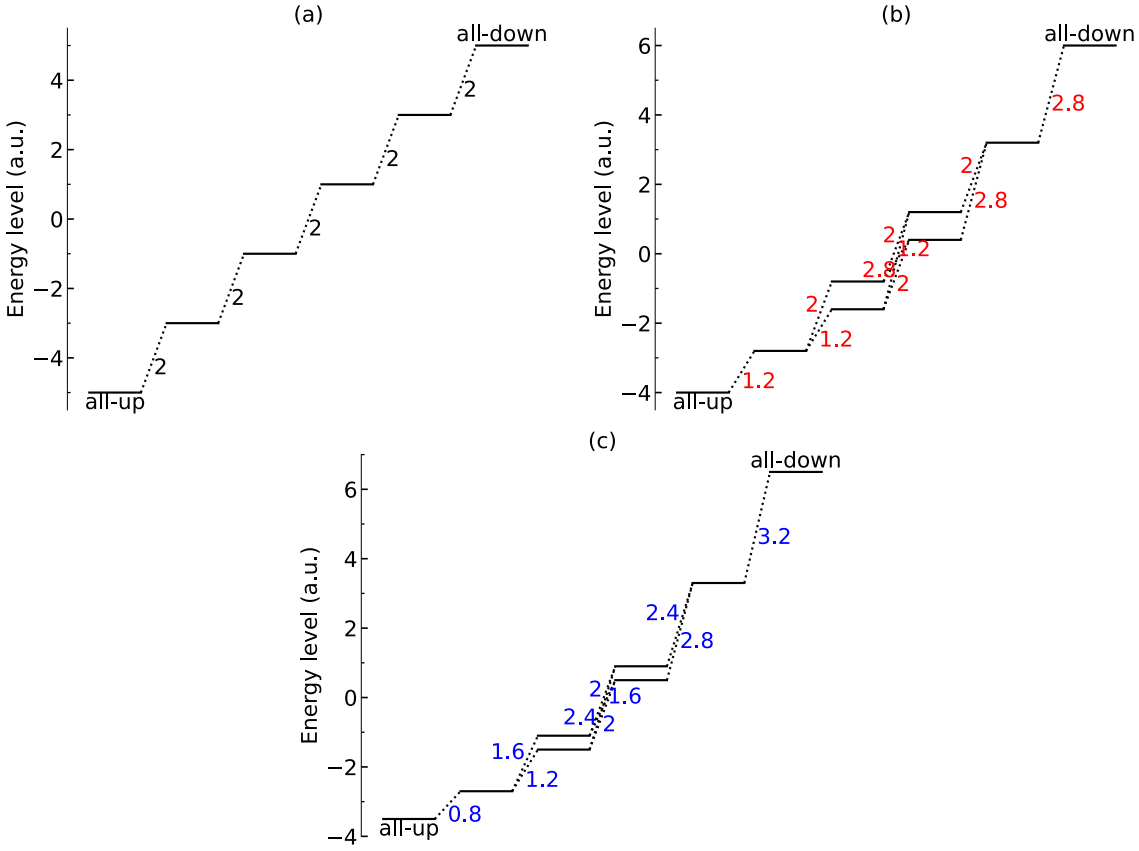

Figure 5.2: **Comparison of energy levels for the systems with nearest-neighbor coupling and full coupling.** Eigenstates in the first subspace of a 5-qubit system when the system has (a) S_n symmetry without coupling terms, (b) D_n symmetry with nearest-neighbor coupling terms as described in Eq. 2.4, and (c) D_n symmetry with full coupling as described in Eq. 5.1. The 'all-up' and the 'all-down' eigenstates at the two ends of the transition cascade are labeled. The transitions permitted by the selection rules are indicated by dashed lines, and the energy differences are shown next to each transition.

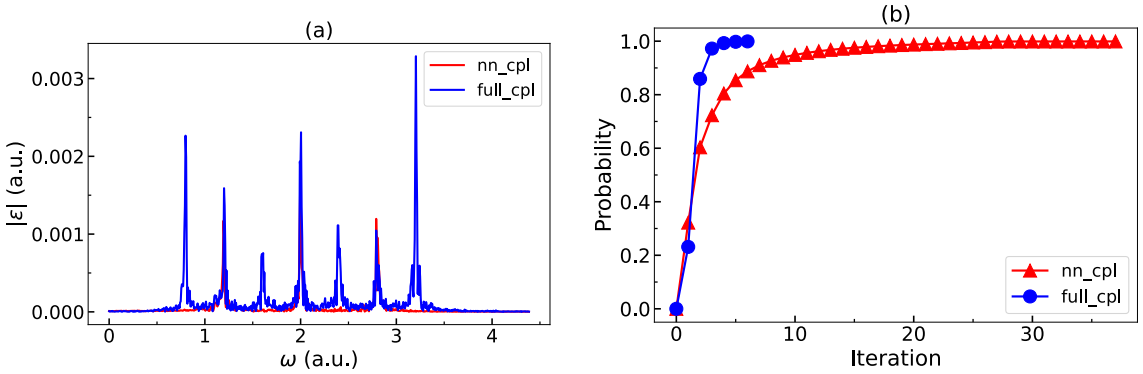

Figure 5.3: **Comparison of power spectra and convergence for the systems with nearest-neighbor coupling and full coupling.** (a) Power spectra of the optimized pulses when the 5-qubit system has nearest-neighbor and full coupling. The frequencies of the three resonance peaks of the nearest-neighbor-coupled system (plotted in red), i.e., 1.2, 2, 2.8 a.u., coincide with the frequencies of the resonance peaks of the fully coupled 5-qubit system (plotted in blue). (b) Comparison of convergence for the system with nearest-neighbor and full coupling.

To fully control transitions in the first subspace, I can introduce coupling terms to break the degeneracy of the resonance frequencies. As shown in Fig. 4.11, using the nearest-neighbor coupling in Eq. 2.4, there will be three resonance frequencies in the n-qubit system when $n \geq 3$. However, when $n \geq 4$, three resonance frequencies are insufficient to completely break the degeneracy of the energy differences, as shown in Figs. 5.1b, 5.2b, 5.4b. When $n \geq 6$, nearest-neighbor coupling terms are even insufficient to completely break the degeneracy of the eigenstates, as shown in Figs. 5.4b. Beyond the nearest neighbors, I can introduce further couplings between qubit pairs:

$$\begin{aligned} H_0 = B_z \cdot \frac{1}{2}\sum_{i=1}^{n}\sigma_z^{(i)} + c_{\text{cpl}}^{(1)} \cdot \frac{1}{4}\sum_{i=1}^{n}\sigma_z^{(i)}\sigma_z^{(i+1)} + c_{\text{cpl}}^{(2)} \cdot \frac{1}{4}\sum_{i=1}^{n}\sigma_z^{(i)}\sigma_z^{(i+2)} \\ + \cdots + c_{\text{cpl}}^{(\lfloor \frac{n}{2} \rfloor)} \cdot \frac{1}{4}\sum_{i=1}^{n}\sigma_z^{(i)}\sigma_z^{(i+\lfloor \frac{n}{2} \rfloor)}, \end{aligned} \tag{5.1}$$

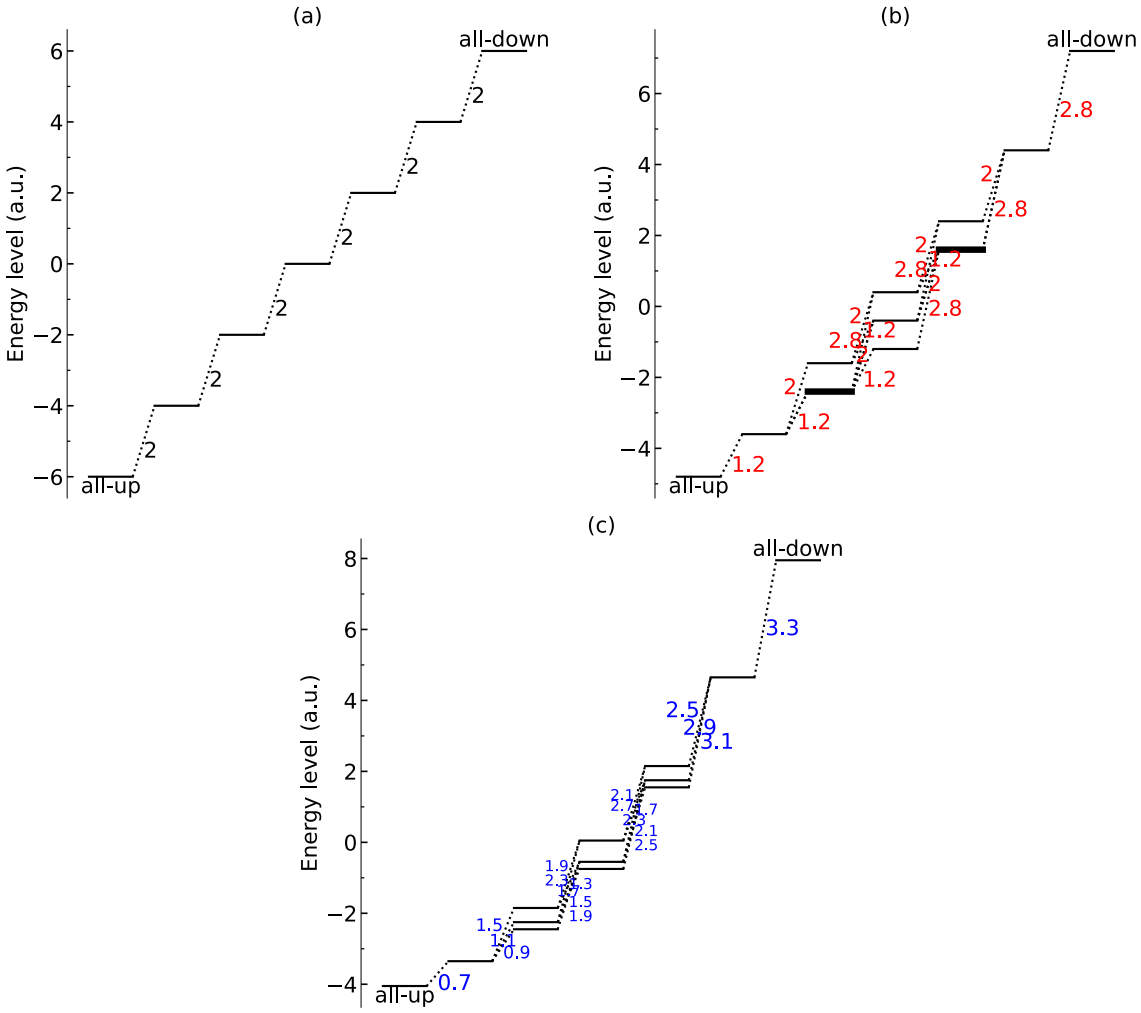

Figure 5.4: **Comparison of energy levels for the systems with nearest-neighbor coupling and full coupling.** Eigenstates in the first subspace of a 6-qubit system when the system has (a) S_n symmetry without coupling terms, (b) D_n symmetry with nearest-neighbor coupling terms as described in Eq. 2.4, and (c) D_n symmetry with full coupling as described in Eq. 5.1. The bold solid lines in (b) indicate degenerate eigenstates. The 'all-up' and the 'all-down' eigenstates at the two ends of the transition cascade are labeled. The transitions permitted by the selection rules are indicated by dashed lines, and the energy differences are shown next to each transition.

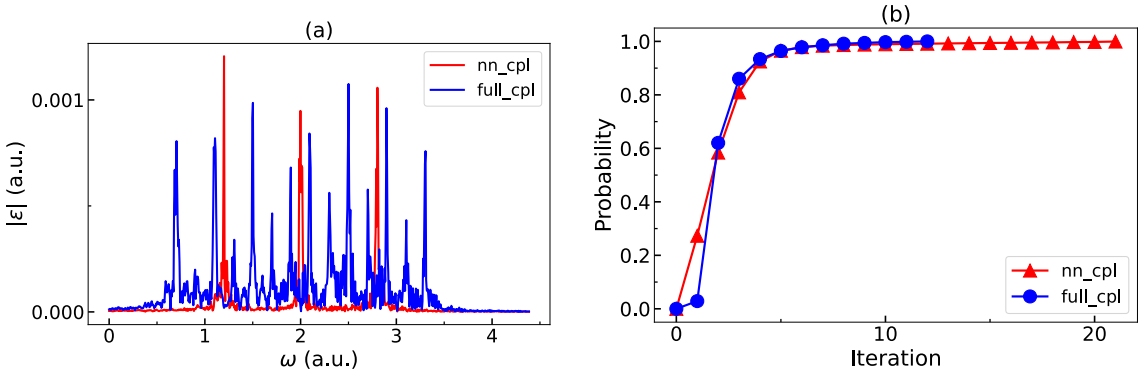

Figure 5.5: **Comparison of power spectra and convergence for the systems with nearest-neighbor coupling and full coupling.** (a) Power spectra of the optimized pulses when the 6-qubit system has nearest-neighbor and full coupling. (b) Comparison of convergence for the system with nearest-neighbor and full coupling.

where $c_{\text{cpl}}^{(1)}$, $c_{\text{cpl}}^{(2)}$, and $c_{\text{cpl}}^{(\lfloor \frac{n}{2} \rfloor)}$ are the nearest-, next-nearest-, and furthest-neighbor coupling strengths, respectively. This form can fully break the degeneracy of energy levels and energy differences. D_n symmetry is preserved with the full coupling terms, and therefore, the eigenstates do not change, whereas their energy levels are modified. As shown in Fig. 5.1c, the degeneracy in the energy differences is completely broken in the 4-qubit system, resulting in 6 resonance frequencies in the power spectra of the fully coupled system in Fig. 5.1d. Similarly, as shown in Figs. 5.2c and 5.4c, the degeneracy in the energy differences is also broken in the 5- and 6-qubit systems by introducing full coupling terms, resulting in more resonance frequencies in the power spectra in Figs. 5.3a and 5.5a. As such, the cascade of transitions from $|\uparrow\rangle^{\otimes n}$ to $|\downarrow\rangle^{\otimes n}$ becomes a series of concatenated two-level systems, and each two-level transition can be enabled by pulses of a unique resonance frequency. [68] This allows me to manipulate the system to be in any eigenstate, or a linear combination of the eigenstates, with a selected route of transitions from the $|\uparrow\rangle^{\otimes n}$ initial state (as long as high-quality pulses with desired resonance frequencies and profiles can be generated). In

summary, properly tuning the coupling coefficients $c_{\text{cpl}}^{(i)}, 1 \leq i \leq \lfloor \frac{n}{2} \rfloor$ in an n-qubit system can completely break the degeneracy of energy differences. The role of each resonance frequency is apparent in a completely non-degenerate system since each one corresponds to an exact transition in the excitation cascade pathway. This enables a more efficient way to manipulate a multi-qubit system. As a demonstration, Figs. 5.1e, 5.3b, and 5.5b show that the probability P in Eq. 2.8 converges in fewer iterations when the multi-qubit system is fully coupled.

I propose that a subspace of the fully coupled multi-qubit system can potentially be a platform for simulating the Hamiltonians of other quantum systems. [37, 38] In a coupled n-qubit system, there are $O(\frac{2^n}{n})$ eigenstates in the first subspace with D_n symmetry. With full coupling, their energy levels can be manipulated by tuning $\lfloor \frac{n}{2} \rfloor + 1$ parameters, namely the static field B_z and the coupling coefficients $c_{\text{cpl}}^{(i)}$. The transitions in the first subspace can be controlled by pulses with selected resonance frequencies, which enables me to examine the features of the Hamiltonian through the evolution of the multi-qubit system. [69, 70] Moreover, I can tailor the "route" of transitions in the cascade when the degeneracy of resonance frequencies is broken; i.e., even though the selection rules indicate allowed transitions, some undesired transitions can be avoided by filtering the corresponding resonance frequency component in the pulses. This allows more controllability in simulating the Hamiltonian with a subspace of the multi-qubit system.

5.2 A Perspective on Ladder Operators and Selection Rules

In this section, I present how to analyze the control Hamiltonian H_c in Eq. 2.5 from the perspective of ladder operators. The selection rule of a multi-qubit system becomes clear with the transformed control Hamiltonians $A_S^\dagger H_c A_S$ or $A_D^\dagger H_c A_D$.

In a single qubit system, σ_x and σ_y form the creation and annihilation operators of the spin; i.e.,

$$\begin{aligned} a_+ &= \frac{1}{2}(\sigma_x + i\sigma_y); \\ a_- &= \frac{1}{2}(\sigma_x - i\sigma_y); \\ a_+|-\rangle &= |+\rangle, a_+|+\rangle = 0; \\ a_-|+\rangle &= |-\rangle, a_-|-\rangle = 0, \end{aligned} \tag{5.2}$$

where $|+\rangle = |\frac{1}{2}, \frac{1}{2}\rangle$ and $|-\rangle = |\frac{1}{2}, -\frac{1}{2}\rangle$ are in the $|J, M\rangle$ basis. In terms of the n-qubit system, the creation and annihilation operator become

$$\begin{aligned} A_+ &= \frac{1}{2}(H_x + iH_y) = \frac{1}{2}\left(\sum_{i=1}^n \sigma_x^{(i)} + i\sum_{i=1}^n \sigma_y^{(i)}\right) = \sum_{i=1}^n a_+^{(i)}; \\ A_- &= \frac{1}{2}(H_x - iH_y) = \frac{1}{2}\left(\sum_{i=1}^n \sigma_x^{(i)} - i\sum_{i=1}^n \sigma_y^{(i)}\right) = \sum_{i=1}^n a_-^{(i)}; \\ A_+|J, M\rangle &= c_+(J, M)|J, M+1\rangle \text{ if } M < J; A_+|J, +J\rangle = 0; \\ A_-|J, M\rangle &= c_-(J, M)|J, M-1\rangle \text{ if } M > -J; A_-|J, -J\rangle = 0, \end{aligned} \tag{5.3}$$

where $c_+(J, M)$ and $c_-(J, M)$ are coefficients depending on J, M. Here $|J, M\rangle$ is the eigenstate of $\tilde{H}_0 = \frac{1}{2}\sum_{i=1}^n \sigma_z^{(i)}$, the operator measuring the quantum number $M = \sum_{i=1}^n m_s^{(i)}$, in

the subspace $\mathcal{H}^J_{[J^{(i)}]}$, i.e.,

$$\tilde{H}_0|J,M\rangle = M|J,M\rangle, |J,M\rangle \in \mathcal{H}^J_{[J^{(i)}]}. \tag{5.4}$$

When the static field B_z is applied, the eigenenergy of the $|J,M\rangle$ states in the multi-qubit system becomes B_zM, i.e.,

$$H_0|J,M\rangle = B_z \cdot \tilde{H}_0|J,M\rangle = B_zM|J,M\rangle. \tag{5.5}$$

I can then manipulate the energy levels by tuning the amplitude of the static field B_z. The creation (A_+) and annihilation (A_-) operators change the quantum number M by ± 1 but leave J unchanged. Therefore, the evolution of the eigenstates $|J,M\rangle$ is restricted within each subspace $\mathcal{H}^J_{[J^{(i)}]}$ when the Hamiltonians have S_n symmetry as in Eqs. 2.3 and 2.5 (this is how the subspaces $\{\mathcal{H}^J_{[J^{(i)}]}\}$ are protected by the S_n symmetry of the system). It should be noted that for each $M \in \{-J, -J+1, \ldots, J-1, J\}$, there is only one basis vector characterized by M (i.e., $|J,M\rangle$) in the subspace $\mathcal{H}^J_{[J^{(i)}]}$. Therefore, the nonzero elements of $A'_+ = A_S^\dagger A_+ A_S$ are at the upper diagonal closest to the main diagonal only, while those of $A'_- = A_S^\dagger A_- A_S$ are at the lower diagonal closest to the main diagonal. Obviously, the value of those nonzero elements are $c_+(J,M)$, and $c_-(J,M)$, respectively. From Eq. 5.3, it is clear that the nonzero elements of $H'_x = A_S^\dagger H_x A_S$ and $H'_y = A_S^\dagger H_y A_S$ are at the two minor diagonals closest to the main diagonal only, while those of the original H_x and H_y are distributed up to the furthest of the 2^{n-1}th minor diagonal. When the controlling pulses $B_x(t)$ and $B_y(t)$ are applied, the distribution of the nonzero elements of H_c in Eq. 2.5 is

the same as H_x and H_y. Thus, I conclude that the unitary similarity transformation of the Hamiltonians with A_S not only block diagonalizes the Hamiltonians but also reduces the number of nonzero minor diagonals. The simulation of the time-dependent Schrödinger equation in Eq. 2.1 is accelerated with these two features.

Since the energy levels $\{B_z M | -J \leq M \leq J\}$ of H_0 are equally spaced, I assert that the energy spectrum of the multi-qubit system with S_n symmetry resembles that of a simple harmonic oscillator even though there are a finite number of energy levels in each subspace $\mathcal{H}^J_{[J^{(i)}]}$. It should be noted that the control Hamiltonians H_x and H_y can only transition between eigenstates whose M differ by ± 1. Therefore, there is only one resonance frequency of the controlling pulses $B_x(t)$ and $B_y(t)$ that can excite transitions between states. Many desired transitions cannot be realized with a single resonance frequency. By removing the degeneracy in the energy level differences, I introduce coupling terms as in Eq. 2.4.

The symmetry of the multi-qubit system is reduced to D_n with the introduction of nearest-neighbor coupling terms. Under the action of the D_n elements, the elements in each orbit of $\{|\uparrow\rangle, |\downarrow\rangle\}^{\otimes n}$ have the same numbers of $|\uparrow\rangle$ and $|\downarrow\rangle$ entries, so M is still a good quantum number for the basis vectors in each subspace $\mathcal{H}^\theta_j$. However, more than one basis vector may be characterized by the same M in $\mathcal{H}^\theta_j$. This is because D_n has much fewer elements than S_n. For two elements in $\{|\uparrow\rangle, |\downarrow\rangle\}^{\otimes n}$ to be in the same D_n-orbit, they should have the same pattern of spins which is invariant under the D_n actions as well as having the same M. As explained in Sec. 3.4, each operator O^θ_j in Eq. 3.19 may act on one or two elements in every orbit characterized by the same M, and each M may characterize more than one orbit. As such, there may be more than one orthonormal

basis vector characterized by the same M in each subspace $\mathcal{H}_j^\theta$. These orthonormal basis vectors of $\mathcal{H}_j^\theta$ are the eigenstates of the coupling Hamiltonian $H_{\text{cpl}} = \sum_{i=1}^{n} \sigma_z^{(i)} \sigma_z^{(i+1)}$, while their eigenvalues are functions of M and the pattern of spins. For 3 qubits and above, the nearest-neighbor coupling terms result in 3 resonance frequencies in the power spectra of the controlling pulses (see Fig. 4.11). Some transitions that are not possible in the S_n-symmetry system can now be realized with more resonance frequencies.

Since there may be more than one basis vector characterized by the same M in the subspace $\mathcal{H}_j^\theta$, its dimension is generally larger than that of the subspace $\mathcal{H}_{[J^{(i)}]}^J$. Note that the control Hamiltonians H_x and H_y still have S_n symmetry and change M by ± 1. One consequence is that there will be more nonzero upper diagonals in the blocks of $A'_+ = A_D^\dagger A_+ A_D$. This is because any basis vector characterized by M may be partially transitioned to more than one basis vector characterized by $M \pm 1$. Similarly, there will be more nonzero lower diagonals in the blocks of $A'_- = A_D^\dagger A_- A_D$. Eq. 5.3 reveals there are more nonzero minor diagonals in $H'_x = A_D^\dagger H_x A_D$ and $H'_y = A_D^\dagger H_y A_D$ compared with those transformed with A_S, as shown in Figs. 4.2b, c, 4.3b, c, 4.4b, c, and 4.5b, c. In other words, more controllability in a multi-qubit system results in an increased subspace dimension and a larger number of nonzero minor diagonals that require more computational resources.

The nonzero elements in A'_+ and A'_- determine the selection rules of the multi-qubit system. Even if two eigenstates are in the same subspace, transitions between them can occur only when their M quantum numbers differ by ± 1. When the two states have a larger difference in M, the initial state must transition to some intermediate states step by step before it fully transitions to the target state. Under D_n symmetry, in certain cir-

cumstances, I am allowed to design a desired "route" (i.e., desired intermediate states) of transitions as long as it is compatible with the selection rules (see Fig. 5.1c). Assuming the controlling pulses can be perfectly constructed to be at the required resonance frequencies (i.e., eigenenergy differences between intermediate states in the desired transition), the transition route can be realized by progressing the entire transition with a series of intermediate transitions while each intermediate transition is enabled with a different resonance frequency. The design of the transition routes is possible because the degeneracy of the energy level differences is removed with the D_n-symmetry coupling terms. However, when the number of qubits, n, is large and the coupling is limited to be between nearest neighbors, some degeneracy of the energy level differences cannot be removed with nearest-neighbor coupling only (see Fig. 5.2b). Also, some eigenstates with the same M may have the same eigenvalues of $H_{\text{cpl}} = \sum_{i=1}^{n} \sigma_z^{(i)} \sigma_z^{(i+1)}$ (see Fig. 5.4b). Consequently, controlling pulses at some resonance frequency may excite more than one transition simultaneously. The state will then evolve to a linear combination of eigenstates, while the ratio of the coefficients of these eigenstates will be the ratio of the magnitude of corresponding nonzero elements in A'_+ and A'_-. In this case, none of these eigenstates can be solely transitioned into. To further break the degeneracy of the energy level differences, I introduce the coupling between next nearest neighbors, next next nearest neighbors, and so on.

For the case of nearest-neighbor coupling only, the number of resonance frequencies of the controlling pulses is limited to 3. I can introduce more coupling between qubits that are further from each other, as defined in Eq. 5.1. When n is even, I can add coupling terms until the ith qubit is coupled to the $(i + \frac{n}{2})$th one because the maximum distance of the

indices between two qubits in $\frac{n}{2}$. In contrast, when n is odd, the ith qubit can be coupled to the $(i+\frac{n-1}{2})$th one at its extreme. These coupling terms will remove, if not completely, a considerable amount of the degeneracy of the energy levels of the eigenstates characterized by the same M. This occurs because the eigenstates with different patterns typically have different eigenvalues. I can then gain more controllability of the multi-qubit system with an increasing number of resonance frequencies. It is worth noting that the coupling strength of each coupling term needs to be carefully tuned, or some of the resonance frequencies will coincide (or be very close to each other), which can be experimentally challenging.

Any transition conserves the angular momentum of the entire physical system. Since the H_x and H_y control Hamiltonians allow transitions between states with M differing by ± 1, the difference of M must be carried by the helicity; i.e., the projection of the spin onto the direction of the momentum of the photon exciting the transition. In this work, I simulate the evolution of the system with a semiquantum model. The controlling pulses are modeled as continuous electromagnetic waves during a finite time span. As such, the helicity of photons is manifested by its classical counterpart, the polarization of electromagnetic waves. Only one handedness of the circularly polarized light, either left-handed or right-handed, is able to excite a specific transition. If the sign of the static Hamiltonian H_0 is changed (i.e., $H_0 \mapsto -H_0$), the other handedness will be selected. The controlling pulses modeled in only one direction, either along the x- or y-axis, can be linearly polarized only. To simulate circularly polarized light, I choose to manipulate the multi-qubit system with both $B_x(t)$ and $B_y(t)$.

Chapter 6

Conclusions

I conclude this dissertation in this chapter. Some content in this chapter is part of *Accelerating Quantum Optimal Control of Multi-Qubit Systems with Symmetry-Based Hamiltonian Transformations*, an article accepted for publication in *AVS Quantum Science*.

The study in this dissertation harnessed the intrinsic symmetry of finite groups to accelerate quantum optimal control calculations in multi-qubit systems. Based on the Young method, I developed an approach to decompose the Hilbert space $\mathcal{H}(\mathbb{C}^{2^n})$ under D_n symmetry or the symmetry of other finite groups. The homogeneity and distinguishability of the qubits, resulting in the symmetry of multi-qubit systems, are ubiquitous in nearly all multi-qubit systems, which allows me to generalize my approach to a variety of quantum computing configurations. In addition to these techniques, I developed a scheme to generalize our symmetry-based Hamiltonian transformation to general systems with the Lie-Trotter-Suzuki decomposition, which is naturally amenable to parallel computing.

My results show that even in the case of inseparable multi-qubit systems, it is possible to decompose the Hilbert space $\mathcal{H}(\mathbb{C}^{2^n})$ into a direct sum of orthogonal and complete subspaces. The QOC computation of multi-qubit systems is much accelerated with the symmetry-based approaches. The selection rules intrinsic to the finite group symmetry restrict the transitions within each subspace, from which I propose the concept of symmetry-protected subspaces. Symmetry-protected subspaces provide a potential platform for preparing permutation-symmetric states and realizing simultaneous quantum gate operations. I also propose a scheme of quantum error suppression and quantum simulation in the symmetry-protected subspaces.

A mathematical proof for the D_n-induced method is provided to guarantee the accuracy of the symmetry-based methods. My approach does not impose constraints to satisfy features of any specific quantum platform, which enables my symmetry-based approach to be easily used for general QOC calculations up to 14 qubits and beyond.

Bibliography

[1] Thomas N. Theis and H.-S. Philip Wong. The end of Moore's law: A new beginning for information technology. *Computing in science & engineering*, 19(2):41–50, 2017.

[2] Hassan N. Khan, David A. Hounshell, and Erica R.H. Fuchs. Science and research policy at the end of Moore's law. *Nature Electronics*, 1(1):14–21, 2018.

[3] M.S. Lundstrom. The MOSFET revisited: Device physics and modeling at the nanoscale. In *2006 IEEE international SOI Conferencee Proceedings*, pages 1–3. IEEE, 2006.

[4] Deblina Sarkar, Xuejun Xie, Wei Liu, Wei Cao, Jiahao Kang, Yongji Gong, Stephan Kraemer, Pulickel M. Ajayan, and Kaustav Banerjee. A subthermionic tunnel field-effect transistor with an atomically thin channel. *Nature*, 526(7571):91–95, 2015.

[5] Peter W. Shor. Algorithms for quantum computation: Discrete logarithms and factoring. In *Proceedings 35th Annual Symposium on Foundations of Computer Science*, pages 124–134. IEEE, 1994.

[6] Lov K. Grover. A fast quantum mechanical algorithm for database search. In *Proceedings of the Twenty-eighth Annual ACM Symposium on Theory of Computing*, pages 212–219. ACM, 1996.

[7] Suppressing quantum errors by scaling a surface code logical qubit. *Nature*, 614(7949):676–681, 2023.

[8] Diego Riste, Stefano Poletto, M.-Z. Huang, Alessandro Bruno, Visa Vesterinen, O.-P. Saira, and Leonardo DiCarlo. Detecting bit-flip errors in a logical qubit using stabilizer measurements. *Nature communications*, 6(1):6983, 2015.

[9] Julian Kelly, Rami Barends, Austin G. Fowler, Anthony Megrant, Evan Jeffrey, Theodore C. White, Daniel Sank, Josh Y. Mutus, Brooks Campbell, Yu Chen, et al. State preservation by repetitive error detection in a superconducting quantum circuit. *Nature*, 519(7541):66–69, 2015.

[10] Jay M. Gambetta, Jerry M. Chow, and Matthias Steffen. Building logical qubits in a superconducting quantum computing system. *npj Quantum Information*, 3(1):2, 2017.

[11] Frank Arute, Kunal Arya, Ryan Babbush, Dave Bacon, Joseph C. Bardin, Rami Barends, Rupak Biswas, Sergio Boixo, Fernando GSL Brandao, David A. Buell, et al. Quantum supremacy using a programmable superconducting processor. *Nature*, 574(7779):505–510, 2019.

[12] Feng Bao, Hao Deng, Dawei Ding, Ran Gao, Xun Gao, Cupjin Huang, Xun Jiang, Hsiang-Sheng Ku, Zhisheng Li, Xizheng Ma, et al. Fluxonium: an alternative qubit platform for high-fidelity operations. *Physical Review Letters*, 129(1):010502, 2022.

[13] Long B. Nguyen, Yen-Hsiang Lin, Aaron Somoroff, Raymond Mencia, Nicholas Grabon, and Vladimir E. Manucharyan. High-coherence fluxonium qubit. *Physical Review X*, 9(4):041041, 2019.

[14] Juan I. Cirac and Peter Zoller. Quantum computations with cold trapped ions. *Physical Review Letters*, 74(20):4091, 1995.

[15] Thomas Monz, Philipp Schindler, Julio T. Barreiro, Michael Chwalla, Daniel Nigg, William A. Coish, Maximilian Harlander, Wolfgang Hänsel, Markus Hennrich, and Rainer Blatt. 14-qubit entanglement: Creation and coherence. *Physical Review Letters*, 106(13):130506, 2011.

[16] Bas Hensen, Hannes Bernien, Anaïs E. Dréau, Andreas Reiserer, Norbert Kalb, Machiel S. Blok, Just Ruitenberg, Raymond F.L. Vermeulen, Raymond N. Schouten, Carlos Abellán, et al. Loophole-free Bell inequality violation using electron spins separated by 1.3 kilometres. *Nature*, 526(7575):682–686, 2015.

[17] Conor E. Bradley, Joe Randall, Mohamed H. Abobeih, R.C. Berrevoets, M.J. Degen, Michiel A. Bakker, Matthew Markham, D.J. Twitchen, and Tim H. Taminiau. A ten-qubit solid-state spin register with quantum memory up to one minute. *Physical Review X*, 9(3):031045, 2019.

[18] Sepehr Ebadi, Tout T. Wang, Harry Levine, Alexander Keesling, Giulia Semeghini, Ahmed Omran, Dolev Bluvstein, Rhine Samajdar, Hannes Pichler, Wen Wei Ho, et al. Quantum phases of matter on a 256-atom programmable quantum simulator. *Nature*, 595(7866):227–232, 2021.

[19] Patrice Bertet, S. Osnaghi, A. Rauschenbeutel, G. Nogues, A. Auffeves, M. Brune, J.M. Raimond, and S. Haroche. A complementarity experiment with an interferometer at the quantum-classical boundary. *Nature*, 411(6834):166–170, 2001.

[20] Sebastien Gleyzes, Stefan Kuhr, Christine Guerlin, Julien Bernu, Samuel Deleglise, Ulrich Busk Hoff, Michel Brune, Jean-Michel Raimond, and Serge Haroche. Quantum jumps of light recording the birth and death of a photon in a cavity. *Nature*, 446(7133):297–300, 2007.

[21] Christine Guerlin, Julien Bernu, Samuel Deleglise, Clement Sayrin, Sebastien Gleyzes, Stefan Kuhr, Michel Brune, Jean-Michel Raimond, and Serge Haroche. Progressive field-state collapse and quantum non-demolition photon counting. *Nature*, 448(7156):889–893, 2007.

[22] Samuel Deleglise, Igor Dotsenko, Clement Sayrin, Julien Bernu, Michel Brune, Jean-Michel Raimond, and Serge Haroche. Reconstruction of non-classical cavity field states with snapshots of their decoherence. *Nature*, 455(7212):510–514, 2008.

[23] Clément Sayrin, Igor Dotsenko, Xingxing Zhou, Bruno Peaudecerf, Théo Rybarczyk, Sébastien Gleyzes, Pierre Rouchon, Mazyar Mirrahimi, Hadis Amini, Michel Brune, et al. Real-time quantum feedback prepares and stabilizes photon number states. *Nature*, 477(7362):73–77, 2011.

[24] D.J. Wineland and N.F. Ramsey. Atomic deuterium maser. *Physical Review A*, 5(2):821, 1972.

[25] P. Oetal Schmidt, Till Rosenband, C. Langer, Wayne M. Itano, James C. Bergquist, and David J. Wineland. Spectroscopy using quantum logic. *Science*, 309(5735):749–752, 2005.

[26] Xian Wang, Paul Kairys, Sri Hari Krishna Narayanan, Jan Hückelheim, and Paul Hovland. Memory-efficient differentiable programming for quantum optimal control of discrete lattices. In *2022 IEEE/ACM Third International Workshop on Quantum Computing Software (QCS)*, pages 94–99, Los Alamitos, CA, USA, Nov. 2022. IEEE Computer Society.

[27] Nelson Leung, Mohamed Abdelhafez, Jens Koch, and David Schuster. Speedup for quantum optimal control from automatic differentiation based on graphics processing units. *Physical Review A*, 95(4):042318, 2017.

[28] Dave Bacon, Isaac L. Chuang, and Aram W. Harrow. Efficient quantum circuits for Schur and Clebsch-Gordan transforms. *Physical review letters*, 97(17):170502, 2006.

[29] Francesca Albertini and Domenico D'Alessandro. Controllability of symmetric spin networks. *Journal of Mathematical Physics*, 59(5), 2018.

[30] Francesca Albertini and Domenico D'Alessandro. Subspace controllability of multipartite spin networks. *Systems & Control Letters*, 151:104913, 2021.

[31] Domenico D'Alessandro. Subspace controllability and Clebsch-Gordan decomposition of symmetric quantum networks. *arXiv preprint arXiv:2307.12908*, 2023.

[32] Jiahui Chen, Hui Zhou, Changkui Duan, and Xinhua Peng. Preparing Greenberger-Horne-Zeilinger and W states on a long-range Ising spin model by global controls. *Physical Review A*, 95(3):032340, 2017.

[33] Quynh T. Nguyen, Louis Schatzki, Paolo Braccia, Michael Ragone, Patrick J. Coles, Frederic Sauvage, Martin Larocca, and M. Cerezo. Theory for equivariant quantum neural networks. *arXiv preprint arXiv:2210.08566*, 2022.

[34] Andrea Skolik, Michele Cattelan, Sheir Yarkoni, Thomas Bäck, and Vedran Dunjko. Equivariant quantum circuits for learning on weighted graphs. *npj Quantum Information*, 9(1):47, 2023.

[35] Andrew M. Childs and Yuan Su. Nearly optimal lattice simulation by product formulas. *Physical Review Letters*, 123(5):050503, 2019.

[36] Thomas Barthel and Yikang Zhang. Optimized Lie-Trotter-Suzuki decompositions for two and three non-commuting terms. *Annals of Physics*, 418:168165, 2020.

[37] Yuri I. Manin. In *Computable and Uncomputable*, pages 13–15. Sov. Radio, 1980.

[38] Richard P. Feynman. Simulating physics with computers. In *Feynman and Computation*, pages 133–153. CRC Press, 2018.

[39] David Deutsch and Richard Jozsa. Rapid solution of problems by quantum computation. *Proceedings of the Royal Society of London. Series A: Mathematical and Physical Sciences*, 439(1907):553–558, 1992.

[40] Richard Cleve, Artur Ekert, Chiara Macchiavello, and Michele Mosca. Quantum algorithms revisited. *Proceedings of the Royal Society of London. Series A: Mathematical, Physical and Engineering Sciences*, 454(1969):339–354, 1998.

[41] Charles H. Bennett and Gilles Brassard. Quantum cryptography: Public key distribution and coin tossing. *arXiv preprint arXiv:2003.06557*, 2020.

[42] Artur K. Ekert. Quantum cryptography based on Bell's theorem. *Physical Review Letters*, 1991.

[43] Han-Sen Zhong, Hui Wang, Yu-Hao Deng, Ming-Cheng Chen, Li-Chao Peng, Yi-Han Luo, Jian Qin, Dian Wu, Xing Ding, Yi Hu, et al. Quantum computational advantage using photons. *Science*, 370(6523):1460–1463, 2020.

[44] Ming Gong, Shiyu Wang, Chen Zha, Ming-Cheng Chen, He-Liang Huang, Yulin Wu, Qingling Zhu, Youwei Zhao, Shaowei Li, Shaojun Guo, et al. Quantum walks on a programmable two-dimensional 62-qubit superconducting processor. *Science*, 372(6545):948–952, 2021.

[45] W. Huang, C.H. Yang, K.W. Chan, T. Tanttu, B. Hensen, R.C.C. Leon, M.A. Fogarty, J.C.C. Hwang, F.E. Hudson, Kohei M. Itoh, et al. Fidelity benchmarks for two-qubit gates in silicon. *Nature*, 569(7757):532–536, 2019.

[46] Ye Wang, Stephen Crain, Chao Fang, Bichen Zhang, Shilin Huang, Qiyao Liang, Pak Hong Leung, Kenneth R. Brown, and Jungsang Kim. High-fidelity two-qubit gates using a microelectromechanical-system-based beam steering system for individual qubit addressing. *Physical Review Letters*, 125(15):150505, 2020.

[47] Ilya N. Moskalenko, Ilya A. Simakov, Nikolay N. Abramov, Alexander A. Grigorev, Dmitry O. Moskalev, Anastasiya A. Pishchimova, Nikita S. Smirnov, Evgeniy V. Zikiy, Ilya A. Rodionov, and Ilya S. Besedin. High fidelity two-qubit gates on fluxoniums using a tunable coupler. *npj Quantum Information*, 8(1):130, 2022.

[48] Fabian Marxer, Antti Vepsäläinen, Shan W. Jolin, Jani Tuorila, Alessandro Landra, Caspar Ockeloen-Korppi, Wei Liu, Olli Ahonen, Adrian Auer, Lucien Belzane, et al. Long-distance transmon coupler with CZ-gate fidelity above 99.8%. *PRX Quantum*, 4(1):010314, 2023.

[49] Jinglei Cheng, Haoqing Deng, and Xuehai Qia. Accqoc: Accelerating quantum optimal control based pulse generation. In *2020 ACM/IEEE 47th Annual International Symposium on Computer Architecture (ISCA)*, pages 543–555. IEEE, 2020.

[50] Frédéric Sauvage and Florian Mintert. Optimal control of families of quantum gates. *Physical Review Letters*, 129(5):050507, 2022.

[51] Navin Khaneja, Timo Reiss, Cindie Kehlet, Thomas Schulte-Herbrüggen, and Steffen J. Glaser. Optimal control of coupled spin dynamics: Design of NMR pulse sequences by gradient ascent algorithms. *Journal of Magnetic Resonance*, 172(2):296–305, 2005.

[52] Vadim F. Krotov and I.N. Feldman. An iterative method for solving optimal-control problems. *Engineering Cybernetics*, 21(2):123–130, 1983.

[53] Tommaso Caneva, Tommaso Calarco, and Simone Montangero. Chopped random-basis quantum optimization. *Physical Review A*, 84(2):022326, 2011.

[54] Yuanqi Gao, Xian Wang, Nanpeng Yu, and Bryan M Wong. Harnessing deep reinforcement learning to construct time-dependent optimal fields for quantum control dynamics. *Physical Chemistry Chemical Physics*, 24(39):24012–24020, 2022.

[55] Akber Raza, Chengkuan Hong, Xian Wang, Anshuman Kumar, Christian R. Shelton, and Bryan M. Wong. NIC-CAGE: An open-source software package for predicting optimal control fields in photo-excited chemical systems. *Computer Physics Communications*, 258:107541, 2021.

[56] Xian Wang, Anshuman Kumar, Christian R. Shelton, and Bryan M. Wong. Harnessing deep neural networks to solve inverse problems in quantum dynamics: Machine-learned predictions of time-dependent optimal control fields. *Physical Chemistry Chemical Physics*, 22(40):22889–22899, 2020.

[57] Dawei Lu, Keren Li, Jun Li, Hemant Katiyar, Annie Jihyun Park, Guanru Feng, Tao Xin, Hang Li, Guilu Long, Aharon Brodutch, Jonathan Baugh, Bei Zeng, and Raymond Laflamme. Enhancing quantum control by bootstrapping a quantum processor of 12 qubits. *npj Quantum Information*, 3(1):45, Oct 2017.

[58] Peter Štelmachovič and Vladimír Bužek. Quantum-information approach to the Ising model: Entanglement in chains of qubits. *Physical Review A*, 70(3):032313, 2004.

[59] Chao Song, Kai Xu, Hekang Li, Yu-Ran Zhang, Xu Zhang, Wuxin Liu, Qiujiang Guo, Zhen Wang, Wenhui Ren, Jie Hao, et al. Generation of multicomponent atomic Schrödinger cat states of up to 20 qubits. *Science*, 365(6453):574–577, 2019.

[60] Zhong-Qi Ma. In *Group Theory for Physicists (Second Edition)*, pages 49–276. World Scientific Publishing Co. Pte. Ltd., 2007.

[61] Qi-Zhi Han and Hong-Zhou Sun. In *Group Theory*, pages 28–184. Peking University Press, 1987.

[62] Xin-Zheng Li. In *Group Theory and its Application to Condensed Matter Physics*, pages 41–199, 260–328. Peking University Press, 2019.

[63] Minking Eie and Shou-Te Chang. In *A Course on Abstract Algebra*, pages 144–151. World Scientific Publishing Co. Pte. Ltd., 2010.

[64] Christophe Cheverry and Nicolas Raymond. In *A Guide to Spectral Theory*, pages 203–228. Birkhäuser Advanced Texts Basler Lehrbücher, 2021.

[65] Asher Peres. Reversible logic and quantum computers. *Physical Review A*, 32(6):3266, 1985.

[66] Peter W. Shor. Scheme for reducing decoherence in quantum computer memory. *Physical Review A*, 52(4):R2493, 1995.

[67] Austin G. Fowler, Matteo Mariantoni, John M. Martinis, and Andrew N. Cleland. Surface codes: Towards practical large-scale quantum computation. *Physical Review A*, 86(3):032324, 2012.

[68] Taiwang Cheng and Alex Brown. Quantum computing based on vibrational eigenstates: Pulse area theorem analysis. *The Journal of Chemical Physics*, 124(3):034111, 2006.

[69] Seth Lloyd. Universal quantum simulators. *Science*, 273(5278):1073–1078, 1996.

[70] Dominic W. Berry, Graeme Ahokas, Richard Cleve, and Barry C. Sanders. Efficient quantum algorithms for simulating sparse hamiltonians. *Communications in Mathematical Physics*, 270:359–371, 2007.